# 4C SEISMIC SHEAR WAVE SOURCE MECHANISM ANALYSIS, MODELING AND IMAGING IN THE SHALLOW MARINE ENVIRONMENT OF THE ARABIAN GULF

A Dissertation

by

HAMDI MAHMOOD

Submitted to the Graduate and Professional School of
Texas A&M University
in partial fulfillment of the requirements for the degree of

DOCTOR OF PHILOSOPHY

| | |
|---|---|
| Chair of Committee, | Yuefeng Sun |
| Committee Members, | Mark Everett |
| | Benchun Duan |
| | David Schechter |
| Head of Department, | Julie Newman |

May 2022

Major Subject: Geophysics

ABSTRACT

Reservoirs in the Arabian Gulf, home to some of the world's largest oil reserves, consist primarily of heterogeneous carbonate rocks and successfully recovering hydrocarbons from them is a challenge. With existing technologies, most of the oil reserves located in the offshore carbonate fields in the Arabian Gulf will remain unrecoverable. Shear wave information is essential for reservoir characterization in the offshore fields of the Arabian Gulf. Used together with P waves, S waves can help better delineate reservoir structures and discriminate bypassed hydrocarbons for production monitoring. The Arabian Gulf has extremely shallow waters ($\sim$ 10 $m$) and varied hard sea-bottom, which results in highly dispersive waves, water-bottom reverberations, and severe anti-aliasing. Previous studies have also observed strong shear wave energy conversion at the sea-bottom in the Arabian Gulf. In this dissertation, I will analyze the source mechanism in order to understand and utilize the strong shear wave generated in the region.

Classical wave propagation analysis, especially the ray theory, is not adequate to address the complex interactions between the acoustic source and sea-bottom in the shallow waters. It remains a long-standing challenging problem to explain the S* and SH* waves observed in the field decades ago. In this dissertation, we propose a conceptual body force model that explains the generation of SH* and S* waves from an explosive source in the shallow water with a hard sea-bottom. This model defines an effective source on the seafloor directly under the acoustic source load from mechanical deformation analysis. Instead of a wave propagation model, the mechanical model considers the source and the boundary together as one volume element of elastic deformation. From the mechanical model, the body force components for P, SV, and SH waves are explicitly defined by the water depth and the Poisson ratio difference of the media. Exact analytical solutions are derived for the near-field and far-field wave propagation from the effective source. Analysis is given for three sea-bottom scenarios, soft mud, intermediate, and hard coral reef, to observe the effect of source distance to the sea-bottom and sea-bottom hardness on wave propagation. Shear waves generated from shallow source and hard sea-bottom are more than a thousand times stronger

compared to far source and soft sea-bottom. Further, finite-difference wave modeling is utilized to analyze the source mechanism in the shallow marine environment using the full wave-form solutions.

Field 2D 4C seismic data acquired in the Arabian Gulf is processed for confirmation of the existence of shear waves generated from the explosive source in the shallow waters and for direct shear wave imaging of the subsurface. The processed inline shear wave is not the evanescent PS* waves as other authors proposed. It is the body shear waves which are generated at the impact point by effective source's SV component. It propagates into the medium as a pure shear wave that we refer to as direct shear (PSS). The SH* waves generated at the impact point by the effective source's SH component should be detected by processing the 2D 4C crossline data or 3D 4C data. An established model-driven approach is used, based on reliable P and S wave velocity from well log. The proposed workflow enhances reflected energy signals to extract shear wave information. P and S wave extracted seismic sections have similar geological structural features, but the S stacked section has higher frequency and higher resolution on the inline component than P wave sections. This processing workflow greatly enhances the signal-to-noise ratio of the seismic data and directly extracts shear wave information for reservoir characterization.

# DEDICATION

To my mother, Hamda Ali Alfalahi. To my wife, Anood Almheiri. To my sons, Yousef and Khalid. To my brother, Ahmad.

# ACKNOWLEDGMENTS

My special thanks goes to my advisor and chairman of my committee, Dr. Yuefeng Sun for his advice, thoughtful direction, and encouragement. His scientific knowledge and depth of thought are inspiring. I would like to thank the members of my advising committee members, Dr. Mark Everett, Dr. Benchun Duan, and Dr. David Schechter for giving valuable direction, suggestions, and recommendations to improve this work. I also thank Dr. Richard Gibson for being on my committee member when he was at Texas A&M University.

I am grateful to the scholarship department at Abu Dhabi National Oil Company (ADNOC) for sponsoring me during my study and providing me with the resources that helped me complete my dissertation. I am also indebted to all members of the Reservoir Geophysics Group at Texas A&M University who all have provided me priceless assistance in many aspects of my life and studies.

CONTRIBUTORS AND FUNDING SOURCES

## Contributors

This work was supervised by a dissertation committee consisting of Professor(s) Yuefeng Sun, Mark Everett, and Benchun Duan of the Department of Geology and Geophysics and Professor David Schechter of the Department of Petroleum Engineering.

All work for the dissertation was completed independently by the student.

## Funding Sources

Graduate study was supported by a scholarship from Abu Dhabi National Oil Company (ADNOC).

# NOMENCLATURE

| | |
|---|---|
| 4C | Four Components |
| OBC | Ocean Bottom Cable |
| Vp | Compressional Wave Velocity |
| Vs | Shear Wave Velocity |
| SH | Shear Horizontal |
| SV | Shear Vertical |
| S/N | Signal to Noise Ratio |
| CMP | Common Middle Point |
| CCP | Common Conversion Point |
| FK | Frequency-Wavenumber |
| FX | Frequency-Space |
| SWA | Surface Wave Attenuation |
| NMO | Normal Moveout Correction |
| FDM | Finite Difference Modeling |

TABLE OF CONTENTS

Page

LIST OF FIGURES

FIGURE Page

# 1. INTRODUCTION

## 1.1 Statement and Significance of the Problem

The impact of seismic technologies has been of paramount importance in oil and gas explorations. With advanced seismic methods, major contributions were made on increasing proven reserves and reserve-production ratios worldwide. Over the past decades, multicomponent seismic method has become one of the most significant breakthroughs in seismic technology. Multicomponent seismic, commonly known as 4C seismic when deployed in water, aims to measure the particle motion of the propagating seismic wave in three orthogonal directions (X-Y-Z) as well as the pressure component (Hydrophone). 4C seismic record includes measurements from not only compressional waves (P-waves) but also transverse shear waves (S-waves). S-waves aid in better subsurface imaging, detecting oil-water contact, and delineating the top or base of the reservoir unit that is not detectable by P-waves alone (Yilmaz, 2001). Furthermore, S-waves can be used to identify fluid types in reservoir rocks, discriminate sand from shale, and map hydrocarbon saturation with the goal of characterizing oil and gas reservoirs accurately (Stewart et al., 2002). To characterize reservoirs, most studies rely on both P-wave imaged seismic data and S-waves estimated from AVO (Amplitude Variation with Offset) analysis techniques (DeVault et al., 2002); however, some studies show better mapping of reservoirs using PS imaged data over AVO (Singh et al., 2015). Nevertheless, the key benefit of 4C seismic data remains in the extraction of shear waves directly from the multicomponent dataset (Farfour and Yoon, 2016). Unfortunately, most studies (Crompton et al., 2005; Johns et al., 2006; Rajput, 2010) utilize shear waves in 4C seismic data by focusing on the pressure and vertical components only, neglecting both the inline and crossline geophone components due to lower signal-to-noise (S/N) ratios that arise from coupling issues. With existing technologies, most of the reserves located in the offshore carbonate fields in the United Arab Emirates (U.A.E.) will remain unrecoverable. To recover them, a fundamental understanding of reservoir heterogeneity and reservoir fluid flow is essential. Therefore, shear waves

can help delineate reservoir structure and discriminate bypassed hydrocarbons which makes them an important tool for carbonate reservoir description and monitoring in the U.A.E. offshore fields, which is home to 8 percent of the global oil reserves.

The data used in this study includes a 2D-4C seismic data recorded offshore Abu Dhabi in the United Arab Emirates (U.A.E.) on the Arabian Gulf. In this area, the water levels are very shallow at 15 m depth only and the seabed comprises of a hard sea-bottom that is due to the scattered hard coral reefs. In addition, the subsurface in the region is characterized by both anhydrite seals and heterogeneous carbonate reservoir rocks. Therefore, shallow water environment in the Arabian Gulf presents a unique setting that presents certain challenges compared to its counterpart in the North Sea as shown in Figure 1.1.

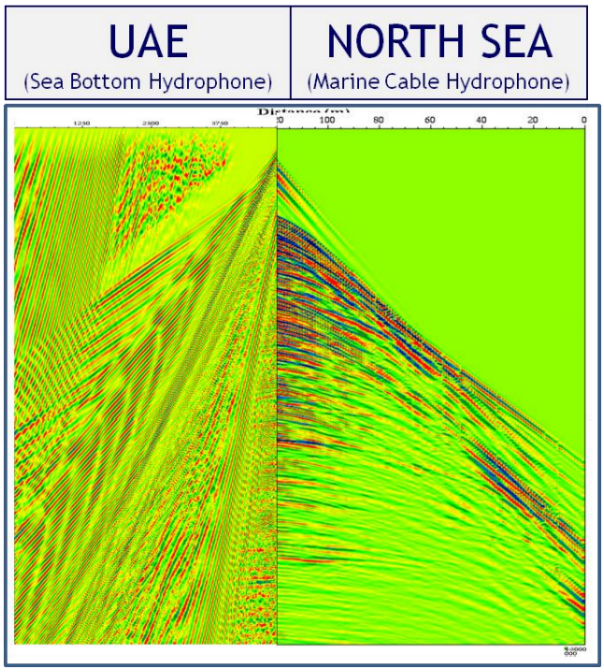


Figure 1.1: Seismic shot record comparison between UAE (shallow water) and the North Sea (deep-sea) Modified from (Berteussen and Sun, 2010).

In the Arabian Gulf, the major challenges can be summarized as highly dispersive surface waves, spatial aliasing, and severe internal multiples. All these characteristics are attributed to the

shallow water and hard sea bottom of the Arabian Gulf that are not present in the deep water environment of the North Sea. However, reflectivity modeling for a P-wave source in shallow water setting (<15 m depth) indicates that strong P-S conversion occurring at the sea-bottom is more than a thousand times stronger than in deep-water environments (>100 m depth) as shown in Figure 1.2 (Sun and Berteussen, 2009). The modeling depicts the relative energy transmitted to the subsurface

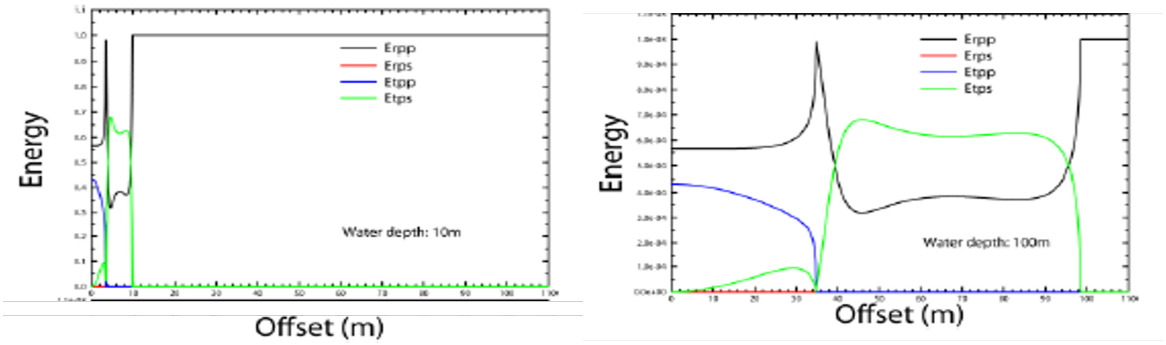


Figure 1.2: A comparison of energy transmitted into the subsurface for a pressure source in a 10 m water depth setting (left) and a 100 m water depth setting (right). The green line represents the energy transmitted for the converted S wave at the sea bottom. Adapted from (Sun and Berteussen, 2009).

with offset for the shallow water and deep-water setting. The energy transmitted for the shallow water setting is order of magnitudes higher than the deep-water setting. Furthermore, the energy transmission peaks within the first 20 m from the source and after that total internal reflection occurs. This means that in the shallow water seismic acquisition most of the energy conversion happens within the vicinity of the source which leads to complex wave-sea bottom interactions. Therefore, the shallow marine environment of the Arabian Gulf presents a unique opportunity for efficient energy penetration of S-waves into the elastic rocks below the water bottom which is important to obtaining shear wave information from converted waves for reservoir monitoring (Sun and Berteussen, 2009). However, the strong shear wave transmission utilizes relative amplitudes and is based on the assumption of classical plane wave theory. The assumption of plane waves

propagating from the source is not valid in the shallow marine environment of the Arabian gulf due to the proximity of the sea-bottom to the pressure source. Thus, energy partition may not be addressed adequately using classical plane theory. To address this, analytical solution of the wave equation is required to quantify the amplitude response in the shallow water setting due to the shallow water and hard sea-bottom. The first exact analytical computation of a propagating wavefield is attributed to Sir Horace Lamb (Lamb, 1904). His solution involves investigating surface motions of linear elastic, isotropic, homogeneous halfspace due to an impulsive point source acting vertically on a boundary; problems of this nature are commonly referred to as Lamb's problem. Analytical solution of wavefields can be found using two main methods. The first method involves Fourier superposition over time domain solutions. This method was first used by Lamb which involves mutliple integrations and asymptotic assumptions to arrive at the analytical solution. This method was expanded further into elastic over elastic half-spaces by several authors (Ewing et al., 1957; Berkhovskikh, 1980). Berkhovskikh (1980) examined the fluid over elastic half-space case but only considered normal modes for his analysis. The other method employs time-domain solutions without the use of Fourier superposition to avoid the asymptotic evaluation of multiple integrals. These group of methods were developed by Cagniard and expanded further by other authors (Cagniard, 1939; Pekeris, 1956); however, it wasn't until de-Hoop's contribution that the Cagniard method became widely known and is now commonly referred to as Cagniard de-Hoop method (de Hoop, 1960). Using the Cagniard de-Hoop method, analytical solution of propagating wavefield were sought in an elastic half-space with varying source-receiver geometry (Garvin, 1956). When an explosive source is placed within a wavelength to the boundary in an elastic half-space, non-geometrical shear waves were reported to exist in synthetic seismograms which are known as $S*$ waves.(Hron and Mikhailenko, 1981). The $S*$ waves are non-geometrical waves that appear to propagate from the boundary instead of the source and are interpreted as evanescent waves that exponentially decay with depth. Other non-geometric wave arrivals such as SH* were identified in synthetic seismograms (Daley and Hron, 1988). This phenomenon was further examined in fluid-solid half-space where a $PS*$ wave was identified on synthetic seismogram given

an explosive source close to the sea-bottom boundary (Allouche and Drijkoningen, 2016). The previous analysis also involved using the Cagniard de-Hoop method to find analytical solutions of propagating waves for sources close to the interface. In the shallow water environment, however, the complex wave interaction from the source and sea-bottom cannot be described by classical ray theory propagation analysis; instead, a wave generation analysis subject to the proximity of the source and physical characteristics of the elastic sea-bottom is required to explain the generation of $SH*$ waves from an explosive source in the shallow waters.

Understanding wave generation in the shallow marine environment provides much needed insight into seismic processing and imaging. This environment introduces unique challenges in seismic imaging such as severe surface wave contamination, spatial aliasing, and multiples (Berteussen and Sun, 2010). Zhang et al. (2015) proposed a model-based seismic processing workflow aimed at verifying the existence of shear waves in shallow water 2D-4C OBC (Ocean Bottom Cable) seismic data as shown in Figure 1.3. The stacked seismic images for shear waves were done utilizing

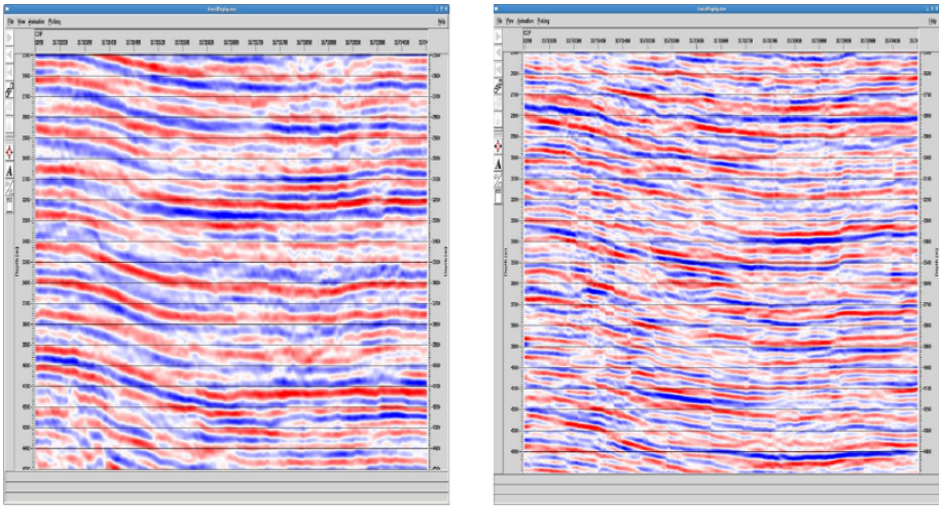


Figure 1.3: A comparison pressure component seismic stacked image using P wave velocity and S wave velocity. Adapted from (Zhang et al., 2015).

S wave velocity stack with a conventional Common MidPoint binning (CMP) instead of Common

Conversion Point (CCP) binning. Those binning techniques are based on the wave propagation in the subsurface and the conversion from P waves to S waves as shown in Figure 1.4. Further,

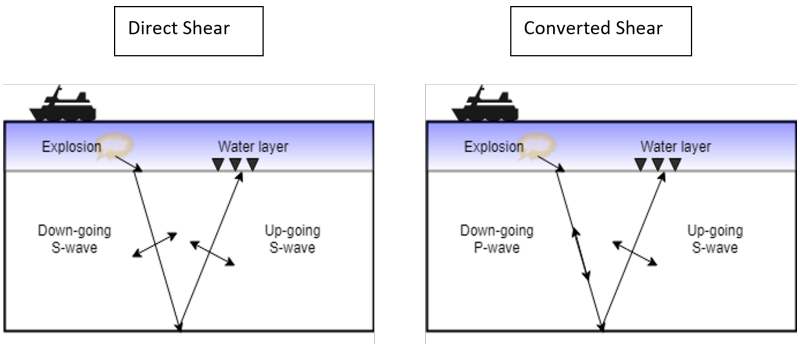


Figure 1.4: A schematic of a marine seismic survey showing the difference between S wave conversion only at the sea bottom and S wave conversion in the subsurface. The S wave conversion at sea-bottom only means the wave propagates only as S wave and requires CMP binning. The S wave conversion at subsurface means the wave propagation downward is P wave and returns to surface as S wave which requires CCP binning.

Berteussen et al. (2014) used the same dataset to extract S-waves from the 4C seismic data using heavy filtering with NMO (Normal Move Out) corrections. Both methods aim to extract P and S waves information from the seismic data by utilizing velocity information from a nearby well log. However, the well log used in their study provides measured P-wave information only; whereas, S wave information was calculated through a constant Vp/Vs ratio. In this study, the well log contains P and S wave information that are both directly measured and available throughout a range that exceeds the reservoir level.

## 1.2 Dissertation Research Objectives

This dissertation is concerned with the generation and propagation of shear waves in the shallow water environment of the Arabian Gulf from the seismic source until the extracting of shear waves in the 2D 4C seismic image. Therefore, the dissertation research objectives are

- Analyze the source mechanism responsible for the complex wave generation in the region

- Explain the complex wave generation in the Arabian Gulf by proposing a new mechanical model
- Verify the generation of strong SH shear waves in the region
- Utilize analytical and numerical solutions to understand the propagation of waves from the source in the shallow marine environment
- Extract direct shear wave information from 2D 4C seismic data

### 1.3 Dataset and Geological Background

The study area is located 25 km NorthWest of Abu Dhabi on the Arabian Gulf between two offshore oil fields as shown in Figure 1.5.


Figure 1.5: Location map of the United Arab Emirates. Study area is NW of Abu Dhabi and is approximately indicated by the highlighted box. Modified from (Granier et al., 2003).

The U.A.E. is part of the Arabian Peninsula and lies at its northeastern corner. In the U.A.E., the existing oil and gas reservoirs developed from the late Permian to the middle Miocene are predominantly carbonate rocks with highly heterogenous quality. The offshore field in this study

area is situated in the NE-trending Rub' Al Khali basin which was floored with evaporates during its initiation as an intracontinental rift basin (Sharland et. al., 2001). During its evolution from the Early Permian, the Rub' Al Khali basin evolved into the NE-trending embayment of the NW-trending Arabian Gulf basin, which is a foreland basin lying between the Arabian Shelf and the Zagros foldbelt. With warm temperatures and very shallow water depth, the area culminated carbonates, mudstones and carbonates-anhydrites that occurred periodically through the geologic age. The anhydrite cycle deposition gave rise to the regional anhydrite seal in the area (Alsharhan and Nairn, 1990). With thermally matured organic-rich source rocks, porous and permeable reservoir rocks, and impermeable seal rocks, the Arabian Gulf Basin is one of the world's largest sources of crude oil.

The study will utilize a 2D 4C OBC seismic line as well as one nearby wireline well log. The seismic line consists of three Geophones, X-Y-Z representing a Cartesian system, and one Hydrophone pressure component deployed on the sea-bottom. In the survey, the average water depth and the source depth are 15 m and 5 m, respectively. 1185 Shots were carried out in the survey with a shot spacing of 18 m and a receiver spacing of 25 m. With 400 receiver groups deployed, the total length of the line is 10 km. The well data for this study contains various well measurements such as caliper, gamma ray, neutron porosity, resistivity, density, compressional wave velocity (Vp), and shear wave velocity (Vs). In this well, Vp and Vs logs are available starting from a measured depth of 42 m up to 3164 $m$; whereas, the density log is available from measured depth of 226 m to 3164 m.

### 1.4 Dissertation Summary

Given the importance of shear waves and challenges present in the shallow marine environment, this dissertation aims to address all the challenges existing with a detailed analysis of the seismic source in the shallow waters of the Arabian Gulf. This includes gaining a fundamental understanding of the source mechanism responsible for the complex wave interactions that leads to the strong shear wave generation in the region. To accomplish that, a novel mechanical model is proposed that explains the complex wave generation in the region. Using this model, an equivalent

body force is established on the sea-bottom and an explicit body force components are derived for P, SV, and SH waves. With propagation analysis, this model is verified both analytically and numerically. From this understanding, direct shear wave information is extracted from 2D 4C seismic data in the shallow marine environment of the Arabian Gulf.

# 2. GENERATION OF SHEAR WAVES FROM AN EXPLOSIVE SOURCE IN THE SHALLOW MARINE ENVIRONMENT

Considering the observed wave phenomenon in the region, multiple challenges are present that affect everything from acquisition to imaging of the seismic data. However, unique opportunities remain due to the shallow water setting and hard sea-bottom. In this chapter, analysis of the explosive source and its interactions with the boundaries in shallow water setting will be conducted in detail to address the strong generation of shear waves in the region. From this analysis, a new body force model is conceptualized that considers the spherical shape of the waves, proximity of the source, and the mechanical nature of the interaction between the source and the sea-bottom boundary. With this model, the correct body force terms for P, SV, and SH waves are explicitly defined using the effective source at the sea-bottom which is responsible for the strong generation of shear waves.

## 2.1 Theory

### 2.1.1 Conceptual Model of the Body Force

In exploration seismology, seismic waves are generated by an active source that are propagated through Earth's medium. Those waves are spherical in nature and undergo physical changes during their propagation due to the varying elastic properties of the Earth. In the shallow waters of the Arabian Gulf, the average water depth is 15 meters and the airgun source is approximately 5 meters above the seafloor. Due to the proximity of the source to the seafloor, the source frequency can be approximately estimated through the seafloor signature as shown in figure 2.1 below.

As depicted from the previous figure, the dominant frequency of the source from the seafloor signature is approximately $f = 30\,Hz$. From the dominant frequency, the dominant period becomes $T = \dfrac{1}{30} = 0.033\,s$. Assuming the average wave velocity in water to be $C = 1500\,m/s$, then the dominant wavelength in the shallow waters of the Arabian Gulf is $\lambda = T * C = 0.033 * 1500 = 50\,meters$. This indicates that with the source depth at 5 meters above the seafloor then the source

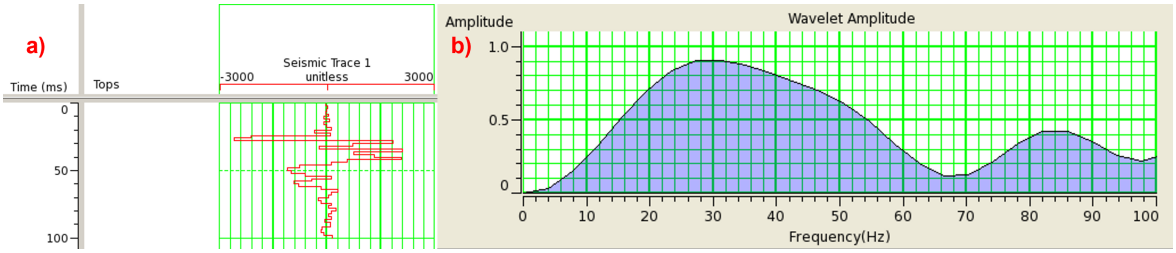


Figure 2.1: Seafloor signature in the shallow waters of the Arabian Gulf from the given airgun source. a) The first 100 ms of the seismic trace closest to the source from a typical shot gather from the seismic data. b) The extracted amplitude spectra from the seismic trace in a). The dominant frequency from the seafloor signature is 30 Hz. The high frequency in the spectra is due to the high frequency coherent noise common in the region.

height compared to the dominant wavelength is $\frac{h}{\lambda} = \frac{5}{50} = \frac{1}{10}$. In such setting, the source is placed one tenth the distance of a dominant wavelength which means that the source exists well within the near-field source radiation. This causes multiple issues that must be identified and addressed adequately . The first problem that needs to be considered is the wave propagation. To visualize it, a comparison of wave propagation between deep and shallow waters is depicted in figure 2.2.

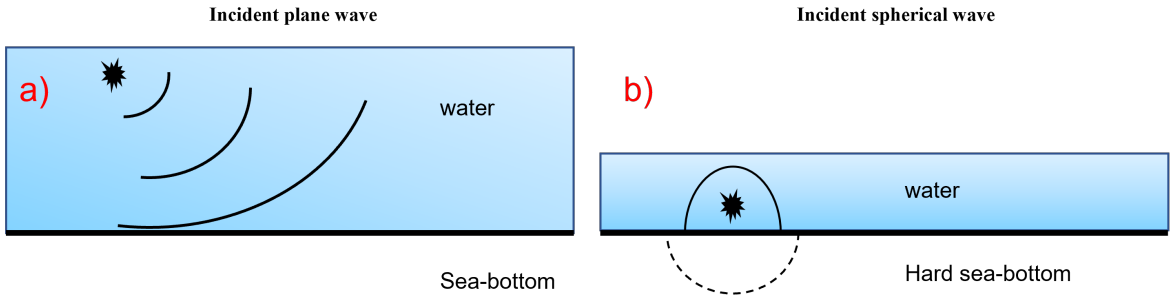


Figure 2.2: A comparison of wave propagation from the source between deep and shallow water environments. a) The wave propagation in deep water environment where the distance from the source to the seafloor is far enough that it can be approximated as an incident plane wave. b) The wave propagation in the shallow water environment where the distance from source to the seafloor is close enough which makes interactions complex and the incident wave remains as a spherical wave without approximations.

Figure 2.2 highlights the difference between a wave propagation from a source in a deep water

and shallow water environments. In the deep water, the source excites spherical waves that progress outward until it interacts with the sea-bottom boundary. In such environment, the distance from the source to the seafloor is much greater than the arc length of the spherical wave that interacts with the sea-bottom boundary. Therefore, the spherical waves in this setting can be approximated as plane waves. The plane wave theory model enables approximate wave amplitude estimation that is convenient especially when considering those waves interactions with boundaries. On the other hand, the wave fronts propagating from the source in the shallow water environments causes complex wave interactions because the source is close to the sea-bottom. The existence of the source within the near-field means that the distance from the source to the sea-bottom cannot be much greater than the arc length of the wave front when it interacts with the seafloor boundary; in fact, it is less. This indicates that the plane wave theory model fails to apply for shallow water setting and the wave propagation model is not sufficient to describe the complex wave interactions that happens in the near-field for the shallow waters of the Arabian Gulf.

In a more comprehensive approach, such as Lamb's problem (Lamb, 1904), spherical waves are decomposed into the summation of plane waves to further analyze the source-boundary interaction in the near-field. In this classical problem, the interest becomes the exact calculation of waves emanating from the impulsive source within the given source/medium geometries. Generally, Lamb's problem involves an impulsive point or line source that acts on a boundary that will then propagate coupled P-SV waves or SH depending on the source configuration.

Given that the ray theory analysis is not a suitable model to describe the wave interactions in the shallow water setting, then a different model is required to better approximate the physical interactions between the source and the hard sea-bottom boundary. The proximity of the source to the hard sea-bottom in the Arabian Gulf enables the source explosion to act directly onto the seabed as a whole. This can be idealized as a vertical force projected directly on the seafloor as shown in figure 2.3.

As shown in figure 2.3, the pressure source is located a distance $h$ from the seafloor but it is close enough that it can be approximated as a vertical force $f_z$ on the seafloor. Intuitively, we

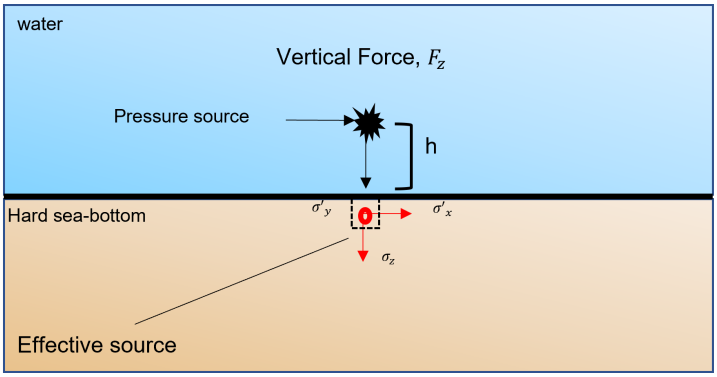


Figure 2.3: The conceptual body force mechanical model. The source proximity to the source is idealized as a vertical force, $F_z$, applied directly on the seafloor. This force directly excites the internal force, $\sigma_z$, which indirectly induces the horizontal internal forces, $\sigma'_x$ and $\sigma'_y$, at the seafloor. The internal forces at the seafloor represent the actual effective source in the shallow water setting and is proportional to the distance from the airgun source and the elastic properties of the hard sea-bottom.

can visualize as follows. Before the instant of the vertical force reaching its impact point on the seafloor, an infinitesimal volume element of the rock mass around the impact point experiences no force in three dimensions. At the instant of the impact, this volume element experiences an external vertical force $f_z$ only. This external vertical force not only generates internal deformations in the vertical direction but also deformations in the horizontal directions. These induced deformations in the horizontal directions produces internal molecular forces in the horizontal directions. After the instant of the impact, these induced internal molecular forces in three directions act as a point source to propagate the deformation energy into the rest of the media, we call this the effective source. To quantify this physical process,the Cartesian coordinates system is employed where $\{x_1 = x, x_2 = y, x_3 = z\}$. Facilitating the mechanical body force model, the external applied force on the seafloor is defined as

$$\begin{aligned} \boldsymbol{f} &= (0, 0, f_z), \\ f_z &= \frac{A}{h^2}\delta(x)S(t) \end{aligned} \tag{2.1}$$

where $A$ is a constant and $f_x = f_y = 0$. Further, $h$ is the distance from the source to the seafloor

and internal force at the seafloor is inversely proportional to the square of the distance from the airgun source. This relationship is reasonable given that the spherical waves in the shallow waters cannot be approximated as plane waves and the intensity of the spherical waves are inversely proportional to the square of the distance from the source (Ikelle and Amundsen, 2010). The $S(t)$ term represents the source time signature which includes the time impulse function. In the mechanical deformation model, we consider a dynamic process at the instantaneous moment of impact on the seafloor. Prior to the external vertical force impact, everything is assumed to be at rest without any external force in all directions. Therefore, this vertical force generates the time-dependent vertical stress in the solid at the moment of the impact that is defined as

$$\sigma_z = \frac{A_0}{h^2}\delta(x)S(t), \tag{2.2}$$

where $A_0$ is a constant and $\sigma_x = \sigma_y = 0$ because no horizontal forces are applied on the seafloor directly from the source at the instant of impact. Here we assume that $\sigma_x$, $\sigma_y$, and $\sigma_z$ are the principal stresses.

As described before, the time-dependent stress at the instant of impact not only generates internal deformation (strain) in the vertical direction but also deformation (strain) in the horizontal directions. Assuming isotropic materials, the deformation (strain) in the infinitesimal volume element around the impact point at the instant of the impact, produced by the external force, can be calculated using the Hooke's law as follows

$$\begin{aligned} e_x &= \frac{1}{E}\left[\sigma_x - \nu(\sigma_y + \sigma_z)\right] \\ e_y &= \frac{1}{E}\left[\sigma_y - \nu(\sigma_x + \sigma_z)\right] \\ e_z &= \frac{1}{E}\left[\sigma_z - \nu(\sigma_x + \sigma_y)\right], \end{aligned} \tag{2.3}$$

where $e$ is the strain which represents a measure of the deformation in the elastic solid, $E$ is the Young's modulus defined as $E = \dfrac{\mu(3\lambda + 2\mu)}{(\lambda + \mu)}$, and $\nu$ is the Poisson's ratio defined as $\nu =$

$\frac{\lambda}{2(\lambda+\mu)}$. It should be noted that only 2 independent elastic constants are required to describe the behavior of isotropic materials; namely, the Lame's constant, $\lambda$, and the shear modulus, $\mu$. Combining equations 2.2 and 2.3 yields:

$$\begin{aligned} e_x &= \frac{1}{E}\left[-\nu(\sigma_z)\right] = \frac{1}{E}\left[\sigma'_x\right] \\ e_y &= \frac{1}{E}\left[-\nu(\sigma_z)\right] = \frac{1}{E}\left[\sigma'_y\right] \\ e_z &= \frac{1}{E}\left[\sigma_z\right]. \end{aligned} \tag{2.4}$$

In equation 2.4, the three strain components, $e_x$, $e_y$, and $e_z$ are the internal deformation produced by the vertical external force at the instant of impact. Following the Hooke's law in elasticity, these strains generate internal stresses in the adjacent molecules immediately after the instant of the impact. This is equivalent to say that the stress components in equation 2.4, $\sigma'_x$, $\sigma'_y$, and $\sigma_z$ can be treated as an effective source. This effective source of stress propagates elastic energy further into the surrounding medium after the instant of impact.

From equation 2.4, it can be seen that the stress of the effective force is produced by the combination of the applied vertical force at the instant of impact and the rock properties of the sea-bottom at the impact point. Although no direct external horizontal forces were applied to the seafloor, the horizontal strains are non-zero after the instant of impact because of the elasticity of the medium; i.e., this is due to the fact that the horizontal deformations are dependent on the vertical stress $\sigma_z$ and the Poisson ratio as given in equation 2.4. Given that the stresses are the forces per unit area, then the deformations in horizontal and vertical directions are excited within a given volume in the solid. This deformation excited by the internal forces form an effective source in the volume at the seafloor directly under the external force, such as the case of an airgun source in the shallow waters of the Arabian Gulf.

In the discussions above, we analyzed the dynamic process of physical source-boundary interactions in the near-field, which is different from the static loading during mechanical deformation due to compaction of sediments. In the study of compaction, we usually assume that under verti-

cal loading there is only vertical strain component and the horizontal components are zero which means the material can freely expand in the horizontal directions. In the compaction scenario, we thus assume $e_x = e_y = 0$. So equation 2.3 becomes

$$\begin{aligned} 0 &= \frac{1}{E}\sigma_x - \frac{\nu}{E}\sigma_y - \frac{\nu}{E}\sigma_z \\ 0 &= -\frac{\nu}{E}\sigma_x + \frac{1}{E}\sigma_y - \frac{\nu}{E}\sigma_z \\ 0 &= \frac{1-\nu}{E}\sigma_x + \frac{1-\nu}{E}\sigma_y - \frac{2\nu}{E}\sigma_z \\ \frac{2(1-\nu)}{E}\sigma_x &= \frac{2\nu}{E}\sigma_z \\ \sigma_x &= \frac{\nu}{1-\nu}\sigma_z, \end{aligned} \tag{2.5}$$

where $\sigma_x = \sigma_y$. Results given in equation 2.5 are valid for mechanical deformation due to static loading during compaction. It is, however, not suitable for the dynamic process we considered here for the source-boundary interaction in the very short time of few milliseconds at and after the instant of impact. In the dynamic process, at the impact point, only the vertical stress component is non-zero but the three strain components are non-zero at the instantaneous moment of the impact; after the instant of impact both stress and strain components are non-zero in general.

In reality, both $\sigma_x$, $\sigma_y$ and $e_x$, $e_y$ in the effective source model should be non-zero after the instant of impact and while $S(t)$ is non-zero. How close or far $\sigma_x$ and $\sigma_y$ are zero as assumed in the source term while $S(t)$ is non-zero may depend on rock properties and the duration of the applied source, and should be tested and evaluated in the future to improve the effective source model.

Having considered the mechanical features of the effective source, the body force in the conceptual model can be formally defined as:

$$\begin{aligned} \boldsymbol{f} &= (f_x, f_y, f_z) \\ &= \frac{A}{h^2}\delta(x)S(t)(-\nu, -\nu, 1). \end{aligned} \tag{2.6}$$

The body force from equation 2.6 represents the effective source in the conceptual body force

model. This source not only takes into account the proximity of the source to the seafloor; but also the material properties of the hard sea-bottom. Those distinctive features form a basis for the shallow water environment in the Arabian Gulf; thus, it is essential they are considered in the model. In this model, the strength of the force in the vertical direction is controlled by the distance h of the airgun source and the seafloor. Moreover, the strength of the horizontal force is affected by the distance $h$ and elastic parameter $\nu$. Generalizing this model to include the limiting case of two fluid boundaries, the Poisson ratio $\nu$ will be replaced by the difference between the two media,

$$\nu = \nu_2 - \nu_1 \tag{2.7}$$

where $\nu_1$ is the Poisson ratio of the first medium, and $\nu_2$ is the Poisson ratio of the medium below the first medium. This model will be used to understand the generation of shear waves from an explosive source in the shallow water setting associated with the hard or soft sea-bottom.

### 2.1.2 The Wave Equation

To study seismic motion in the Earth, an analytical framework must incorporate a seismic source, equations for the motions that propagate once motion has started, and a theory relating the seismic source with the equations of motion. The equation of motion is governed by Newton's law of motion and can be represented in summation notation as:

$$\rho \ddot{u}_i = f_i + \tau_{ij,j}, \tag{2.8}$$

where $\rho$ is the mass density, $u$ is the displacement vector, $f$ is the body force ,and $\tau$ is the stress tensor. Considering infinitesimal motion, the stress is related to strain with the theory of linear stress-strain relation as follows:

$$\tau_{ij} = c_{ijkl} e_{kl}. \tag{2.9}$$

Equation 2.9 is known as the constitutive relation and a system that obeys it is said to be linearly elastic. In linear elasticity, the strain tensor is defined as:

$$e_{ij} = \frac{1}{2}\left(\frac{\partial u_i}{\partial x_j} + \frac{\partial u_j}{\partial x_i}\right) \tag{2.10}$$

The quantities $c_{ijkl}$ are components of a fourth-order tensor; namely, the stiffness tensor. In the isotropic case, the stiffness tensor can be written as

$$c_{ijkl} = \lambda\delta_{ij}\delta_{kl} + \mu\delta\left(\delta_{ik}\delta_{jl} + \delta_{il}\delta_{jk}\right). \tag{2.11}$$

Where the independent constants, $\lambda$ and $\mu$, are the Lamé parameters, and $\delta$ is the Kronecker delta defined as:

$$\delta_{ij} = \begin{cases} 1, & \text{if } i = j, \\ 0, & \text{if } i \neq j. \end{cases}$$

Six independents components of the stiffness tensor remain when considering symmetries due to the stress ($\tau_{ij} = \tau_{ji}$), strain ($e_{ij} = e_{ji}$), and the thermodynamic argument ($c_{ijkl} = c_{klij}$) (Aki and Richards, 2002). In the isotropic case, the reduced stiffness tensor can be expressed in matrix form as:

$$C = \begin{bmatrix} \lambda+2\mu & \lambda & \lambda & 0 & 0 & 0 \\ \lambda & \lambda+2\mu & \lambda & 0 & 0 & 0 \\ \lambda & \lambda & \lambda+2\mu & 0 & 0 & 0 \\ 0 & 0 & 0 & \mu & 0 & 0 \\ 0 & 0 & 0 & 0 & \mu & 0 \\ 0 & 0 & 0 & 0 & 0 & \mu \end{bmatrix} \tag{2.12}$$

Substituting equation 2.12 into equation 2.9 yields:

$$\tau_{ij} = \lambda e_{kk}\delta_{ij} + 2\mu e_{ij} \tag{2.13}$$

Using 2.13, instead of equation 2.9, the wave equation in an isotropic medium can be derived. From equations 2.10, 2.8, and 2.13, the isotropic wave equation in 3D with components can be written as

$$\rho \begin{pmatrix} \frac{\partial^2 u_1}{\partial t^2} \\ \frac{\partial^2 u_2}{\partial t^2} \\ \frac{\partial^2 u_3}{\partial t^2} \end{pmatrix} = (\lambda + 2\mu) \begin{pmatrix} \frac{\partial}{\partial x_1}\left(\frac{\partial u_1}{\partial x_1} + \frac{\partial u_2}{\partial x_2} + \frac{\partial u_3}{\partial x_3}\right) \\ \frac{\partial}{\partial x_2}\left(\frac{\partial u_1}{\partial x_1} + \frac{\partial u_2}{\partial x_2} + \frac{\partial u_3}{\partial x_3}\right) \\ \frac{\partial}{\partial x_3}\left(\frac{\partial u_1}{\partial x_1} + \frac{\partial u_2}{\partial x_2} + \frac{\partial u_3}{\partial x_3}\right) \end{pmatrix} - \mu \begin{pmatrix} \frac{\partial}{\partial x_2}\left(\frac{\partial u_2}{\partial x_1} - \frac{\partial u_1}{\partial x_2}\right) - \frac{\partial}{\partial x_3}\left(\frac{\partial u_1}{\partial x_3} - \frac{\partial u_3}{\partial x_1}\right) \\ \frac{\partial}{\partial x_3}\left(\frac{\partial u_3}{\partial x_2} - \frac{\partial u_2}{\partial x_3}\right) - \frac{\partial}{\partial x_1}\left(\frac{\partial u_2}{\partial x_1} - \frac{\partial u_1}{\partial x_2}\right) \\ \frac{\partial}{\partial x_1}\left(\frac{\partial u_1}{\partial x_3} - \frac{\partial u_3}{\partial x_1}\right) - \frac{\partial}{\partial x_2}\left(\frac{\partial u_3}{\partial x_2} - \frac{\partial u_2}{\partial x_3}\right) \end{pmatrix}, \tag{2.14}$$

or in vector notation, the inhomogeneous wave equation is

$$\rho \ddot{\boldsymbol{u}} = \boldsymbol{f} + (\lambda + 2\mu)\nabla(\nabla \cdot \boldsymbol{u}) - \mu \nabla \times (\nabla \times \boldsymbol{u}), \tag{2.15}$$

where the double over dots implies second derivative with respect to time. The 3D wave equation has three unknowns with a non-trivial solution. This equation supports two type of waves; namely, the transverse and longitudinal waves. Transverse waves are waves that have motion perpendicular to the propagation direction; these types of waves are also known as shear waves (S waves). For longitudinal waves, the motion is parallel to the propagation direction and are commonly known as compressional waves. In acoustics, the longitudinal waves are the same as the pressure waves (P waves). Given those properties, the displacement of the wave equation can be separated into the transverse wave part and the longitudinal wave part. This decomposition is known as the Helmholtz decomposition and is defined as

$$\boldsymbol{u} = \nabla\phi + \nabla \times \boldsymbol{\psi}. \tag{2.16}$$

where $\phi$ is the scalar displacement potential of the P wave (curl-free) and $\boldsymbol{\psi}$ represents the vector displacement potential field of the S wave (divergence-free). Equation 2.16 equates the 3-component vector $\boldsymbol{u}$ to an expression of 4 unknowns; where, the extra constraint is handled by $\nabla \cdot \boldsymbol{\psi} = 0$. Moreover, the Helmholtz decomposition of the displacement field into potentials is satisfied only if the body force from equation 2.15 can also be expressed in terms of Helmholtz

potentials as

$$\boldsymbol{f} = \nabla\Phi + \nabla \times \boldsymbol{\Psi}, \tag{2.17}$$

where $\Phi$ is the scalar body force P potential,$\boldsymbol{\Psi}$ is the vector body force S potential, and $\nabla \cdot \boldsymbol{\Psi} = 0$. The left term on the right hand-side of equation 2.17 represents the compressional (P wave) source and the right term represents the shear (S wave) source of the body force. Substituting the potentials from equations 2.16 and 2.17 into equation 2.15 and utilizing the the vector identity $\nabla \times (\nabla \times \boldsymbol{\psi}) = \nabla\nabla \cdot \boldsymbol{\psi} - \nabla^2\boldsymbol{\psi}$, then the scalar potential satisfies

$$\ddot{\phi} = \frac{\Phi}{\rho} + \alpha^2\nabla^2\phi \tag{2.18}$$

where $\alpha$ is the compressional wave velocity defined as $\alpha^2 = \frac{\lambda+2\mu}{\rho}$. Equation 2.18 is known as the P scalar wave equation since it is curl-free and propagates with the P wave velocity $\alpha$. Similarly, the vector potential satisfies

$$\ddot{\boldsymbol{\psi}} = \frac{\boldsymbol{\Psi}}{\rho} + \beta^2\nabla^2\boldsymbol{\psi}, \tag{2.19}$$

where $\beta$ is the shear wave velocity defined as $\beta^2 = \frac{\mu}{\rho}$. Equation 2.19 is known as the S vector wave equation since it is divergence-free and propagates with the S wave velocity $\beta$.The potential equations satisfy the inhomogeneous wave equation and are simpler than the elastodynamic wave equation which helps break it up into soluble equations. Solutions of the wave equation will be pursued using the potential equations in the subsequent sections and their usefulness will be demonstrated especially when addressing boundary value problems.

## 2.2 Solution for the Elastodynamic Wave Equation in a Homogeneous Medium using the Conceptual Body Force Model

### 2.2.1 Wave Equation Solution using the Body Force P and S potentials

To analyze inhomogeneous solutions of the wave equation, the Helmholtz potential decomposition of the body forces and the displacement fields is utilized. The inhomogeneous body wave equations for P and S waves in isotropic media were expressed in equations 2.18 and 2.19 respec-

tively. The following derivations follows the work of Aki and Richards (2002) for the displacement solutions in a homogeneous, isotropic, and unbounded medium. Prior to finding the solution for the wave equation, the first step involves finding the body-force potentials $\Phi$ and $\Psi$ such that

$$\boldsymbol{f} = (f_1, f_2, f_3) = \frac{A}{h^2}\delta(x)S(t)(-\nu, -\nu, 1) = \nabla\Phi + \nabla \times \boldsymbol{\Psi}. \tag{2.20}$$

At a given moment of time, the body force potentials are defined by solving the Poisson vector equation $\nabla^2 \boldsymbol{W} = \boldsymbol{Z}$, which is given by (Aki and Richards, 2002)

$$\boldsymbol{W}(x,t) = -\iiint_V \frac{\boldsymbol{Z(\xi, t)}}{4\pi|\boldsymbol{x} - \boldsymbol{\xi}|} dV(\xi) \tag{2.21}$$

and

$$\Phi = \nabla \cdot \boldsymbol{W} \tag{2.22}$$

$$\boldsymbol{\Psi} = -\nabla \times \boldsymbol{W} \tag{2.23}$$

Using the conceptual body force model, the vector $Z$ is defined as such

$$\boldsymbol{Z}(x,t) = \frac{A}{h^2}\delta(x)S(t)(-\nu, -\nu, 1), \tag{2.24}$$

so that

$$\boldsymbol{W} = -\frac{AS(t)}{4\pi h^2}\iiint_V (-\nu, -\nu, 1)\frac{\delta(\xi)dV}{|x - \xi|} = -\frac{AS(t)}{4\pi|\boldsymbol{x}|h^2}(-\nu, -\nu, 1). \tag{2.25}$$

Therefore, the body force potentials are

$$\Phi(\boldsymbol{x}, t) = \nabla \cdot \boldsymbol{W} = -\frac{AS(t)}{4\pi h^2}\left(-\frac{\partial}{\partial x_1}\frac{\nu}{|\boldsymbol{x}|} - \frac{\partial}{\partial x_2}\frac{\nu}{|\boldsymbol{x}|} + \frac{\partial}{\partial x_3}\frac{1}{|\boldsymbol{x}|}\right) \tag{2.26}$$

$$\begin{aligned}\boldsymbol{\Psi}(\boldsymbol{x},t) &= -\nabla\times\boldsymbol{W}\\ &= \frac{AS(t)}{4\pi h^2}\left(\frac{\partial}{\partial x_2}\frac{1}{|\boldsymbol{x}|}+\nu\frac{\partial}{\partial x_3}\frac{1}{|\boldsymbol{x}|},-\nu\frac{\partial}{\partial x_3}\frac{1}{|\boldsymbol{x}|}-\frac{\partial}{\partial x_1}\frac{1}{|\boldsymbol{x}|},-\nu\frac{\partial}{\partial x_1}\frac{1}{|\boldsymbol{x}|}+\nu\frac{\partial}{\partial x_2}\frac{1}{|\boldsymbol{x}|}\right)^{\cdot}\end{aligned} \tag{2.27}$$

Substituting equations 2.26 and 2.27 in equations 2.18 and 2.19 respectively, yields the inhomogeneous P and S wave equations

$$\ddot{\phi} = -\frac{AS(t)}{4\pi\rho h^2}\left(-\nu\frac{\partial}{\partial x_1}\frac{1}{|\boldsymbol{x}|}-\nu\frac{\partial}{\partial x_2}\frac{1}{|\boldsymbol{x}|}+\frac{\partial}{\partial x_3}\frac{1}{|\boldsymbol{x}|}\right)+\alpha^2\nabla^2\phi \tag{2.28}$$

$$\ddot{\boldsymbol{\psi}} = \frac{AS(t)}{4\pi\rho h^2}\left(\frac{\partial}{\partial x_2}\frac{1}{|\boldsymbol{x}|}+\nu\frac{\partial}{\partial x_3}\frac{1}{|\boldsymbol{x}|},-\nu\frac{\partial}{\partial x_3}\frac{1}{|\boldsymbol{x}|}-\frac{\partial}{\partial x_1}\frac{1}{|\boldsymbol{x}|},-\nu\frac{\partial}{\partial x_1}\frac{1}{|\boldsymbol{x}|}+\nu\frac{\partial}{\partial x_2}\frac{1}{|\boldsymbol{x}|}\right)+\beta^2\nabla^2\boldsymbol{\psi}. \tag{2.29}$$

Finding the displacements involves solving the wave equations for the Lamé potentials $\phi$ and $\boldsymbol{\psi}$. Since the body force potentials are defined in the whole volume $V$, the Lamé potentials solutions must be written in integral form as

$$\phi(x,t) = -\frac{A}{(4\pi\alpha)^2\rho h^2}\iiint_V \frac{S\left(t-\frac{|x-\xi|}{\alpha}\right)}{|x-\xi|}\left(-\nu\frac{\partial}{\partial\xi_1}\frac{1}{|\xi|}-\nu\frac{\partial}{\partial\xi_2}\frac{1}{|\xi|}+\frac{\partial}{\partial\xi_3}\frac{1}{|\xi|}\right)dV(\xi) \tag{2.30}$$

$$\boldsymbol{\psi}(x,t) = \frac{A}{(4\pi\beta)^2\rho h^2}\iiint_V \frac{S\left(t-\frac{|x-\xi|}{\alpha}\right)}{|x-\xi|}\left(\frac{\partial}{\partial\xi_2}\frac{1}{|\boldsymbol{\xi}|}+\nu\frac{\partial}{\partial\xi_3}\frac{1}{|\boldsymbol{\xi}|},-\nu\frac{\partial}{\partial\xi_3}\frac{1}{|\boldsymbol{\xi}|}-\frac{\partial}{\partial\xi_1}\frac{1}{|\boldsymbol{\xi}|},-\nu\frac{\partial}{\partial\xi_1}\frac{1}{|\boldsymbol{\xi}|}+\nu\frac{\partial}{\partial\xi_2}\frac{1}{|\boldsymbol{\xi}|}\right)dV(\xi). \tag{2.31}$$

It is important to note that all potentials are defined over the whole volume especially for force potentials even when the body forces are acting at a point. In the preceding equations, the evaluation of the volume integral is separated into two parts, first an integral over a spherical surface $\Omega$ and second and integral over time $\tau$ from zero to infinity. Considering the P wave equation, the volume integral can then be separated as

$$\phi(x,t) = -\frac{A}{(4\pi\alpha)^2\rho h^2}\int_0^\infty \frac{S(t-\tau)}{\tau}\left(\iint_\Omega\left(-\nu\frac{\partial}{\partial\xi_1}\frac{1}{q}-\nu\frac{\partial}{\partial\xi_2}\frac{1}{q}+\frac{\partial}{\partial\xi_3}\frac{1}{q}\right)d\Omega(\xi)\right)d\tau, \tag{2.32}$$

with $\alpha\tau = |x - \xi|$ and $q = |\xi|$. To facilitate the previous integral, the geometry configuration of the spherical surface is depicted in figure 2.4 below.

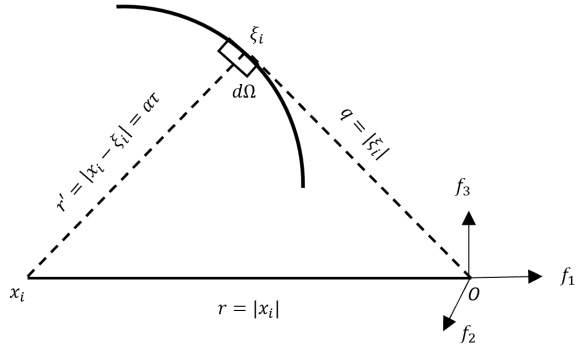


Figure 2.4: Geometry configuration of the spherical surface $\Omega$ with center at $x_i$ and radius $r' = |x_i - \xi_i| = \alpha\tau$.

The parameter q is the distance from the origin to an element $d\Omega$ of the spherical surface $\Omega$, $r = |x_i|$ is the distance from the origin to the position where displacement due to the applied force is evaluated in the volume, and $r' = |x_i - \xi_i| = \alpha\tau$ is the distance from the point $x_i$ to the point $\xi_i$ on the spherical surface. The evaluation of the surface integral involves considering the spherical surface $\Omega$ position relative to the origin $O$. When the spherical surface extends beyond the origin ($\tau > \dfrac{r}{\alpha}$) then the integral over $\Omega$ is constant and equal to $4\pi\alpha\tau$, and thus its derivative is zero. Conversely, if the spherical surface does not include the origin ($\tau < \dfrac{r}{\alpha}$), then the integral has a value of $\dfrac{4\pi\alpha^2\tau^2}{r}$ (Aki and Richards, 2002). Therefore, the integral of the spherical sphere becomes

$$\iint_{\Omega} \left( -\nu \frac{\partial}{\partial \xi_1} \frac{1}{q} - \nu \frac{\partial}{\partial \xi_2} \frac{1}{q} + \frac{\partial}{\partial \xi_3} \frac{1}{q} \right) d\Omega(\xi) = 4\pi\alpha^2\tau^2 \left( -\nu \frac{\partial}{\partial x_1} \frac{1}{r} - \nu \frac{\partial}{\partial x_2} \frac{1}{r} + \frac{\partial}{\partial x_3} \frac{1}{r} \right). \quad (2.33)$$

Substituting equation 2.33 into 2.31 yields

$$\phi = -\frac{A}{4\pi\rho h^2} \left( -\nu \frac{\partial}{\partial x_1} \frac{1}{r} - \nu \frac{\partial}{\partial x_2} \frac{1}{r} + \frac{\partial}{\partial x_3} \frac{1}{r} \right) \int_0^{r/\alpha} \tau S(t - \tau) d\tau. \quad (2.34)$$

Following the same development for the S wave field, the vector potential $\boldsymbol{\psi}$ becomes

$$\boldsymbol{\psi} = \frac{A}{4\pi\rho h^2}\left(\frac{\partial}{\partial x_2}\frac{1}{r} + \nu\frac{\partial}{\partial x_3}\frac{1}{r}, -\nu\frac{\partial}{\partial x_3}\frac{1}{r} - \frac{\partial}{\partial x_1}\frac{1}{r}, -\nu\frac{\partial}{\partial x_1}\frac{1}{r} + \nu\frac{\partial}{\partial x_2}\frac{1}{r}\right)\int_0^{r/\beta}\tau S(t-\tau)d\tau. \tag{2.35}$$

To obtain the displacement $\boldsymbol{u}$ then equations 2.34 and 2.35 are substituted in equation 2.16 as follows

$$\begin{aligned}
&\boldsymbol{u} = \boldsymbol{u}^P + \boldsymbol{u}^S = \nabla\phi + \nabla\times\boldsymbol{\Psi},\\
&\boldsymbol{u} = -\frac{A}{4\pi\rho h^2}\nabla\left(-\nu\frac{\partial}{\partial x_1}\frac{1}{r} - \nu\frac{\partial}{\partial x_2}\frac{1}{r} + \frac{\partial}{\partial x_3}\frac{1}{r}\right)\int_0^{r/\alpha}\tau S(t-\tau)d\tau +\\
&\quad\frac{A}{4\pi\rho h^2}\nabla\times\left(-\nu\left[\frac{\partial}{\partial x_2}\frac{1}{r} - \frac{\partial}{\partial x_3}\frac{1}{r}\right], -\nu\left[\frac{\partial}{\partial x_3}\frac{1}{r} - \frac{\partial}{\partial x_1}\frac{1}{r}\right], \frac{\partial}{\partial x_1}\frac{1}{r} - \frac{\partial}{\partial x_2}\frac{1}{r}\right)\int_0^{r/\beta}\tau S(t-\tau)d\tau.
\end{aligned} \tag{2.36}$$

The parameter $r$ can be expressed from a generic point $\xi_i$ where the force is applied to the point $x_i$ where the displacement is evaluated, is defined in the volume $V$ as

$$r = \left[(x_1-\xi_1)^2 + (x_2-\xi_2)^2 + (x_3-\xi_3)^2\right]^{1/2}, \tag{2.37}$$

Evaluating the displacement in equation 2.36 involves taking derivatives or $r$ and $1/r$ with respect to $x_i$ which is

$$\frac{\partial}{\partial x_i}r = \frac{x_i-\xi_i}{r} = \frac{r_i}{r}, \tag{2.38}$$

$$\frac{\partial}{\partial x_i}\frac{1}{r} = -\frac{x_i-\xi_i}{r^3} = -\frac{r_i}{r^3}. \tag{2.39}$$

Using equations 2.37, 2.38, and 2.39 together yields

$$u_i^P = \frac{Ak_j}{4\pi\rho h^2}\left[-\left(\frac{3r_ir_j}{r^5} - \frac{\delta_{ij}}{r^3}\right)\int_0^{r/\alpha}\tau S(t-\tau)d\tau + \frac{r_ir_j}{r^3\alpha^2}S\left(t-\frac{r}{\alpha}\right)\right], \tag{2.40}$$

$$u_i^S = \frac{Ak_j}{4\pi\rho h^2}\left[\left(\frac{3r_ir_j}{r^5}-\frac{\delta_{ij}}{r^3}\right)\int_0^{r/\beta}\tau S(t-\tau)d\tau - \frac{r_ir_j}{r^3\beta^2}S\left(t-\frac{r}{\beta}\right)+\frac{\delta_{ij}}{r\alpha^2}S\left(t-\frac{r}{\beta}\right)\right], \tag{2.41}$$

with the vector $k_j$ defined as $\boldsymbol{k} = (-\nu, -\nu, 1)$. Combining equations 2.40 and 2.41 together yields the total displacement as follows

$$u_i = \frac{Ak_j}{4\pi\rho h^2}\left[\left(\frac{3r_ir_j}{r^5}-\frac{\delta_{ij}}{r^3}\right)\int_{r/\alpha}^{r/\beta}\tau S(t-\tau)d\tau + \frac{r_ir_j}{r^3\alpha^2}S\left(t-\frac{r}{\alpha}\right)+\frac{1}{r\beta^2}\left(\delta_{ij}-\frac{r_ir_j}{r^2}\right)S\left(t-\frac{r}{\beta}\right)\right]. \tag{2.42}$$

The preceding equation is commonly known as Stokes formula (Stokes, 1849). It gives the displacement component in the i-direction at the point $\boldsymbol{x}$, due to a concentrated arbitrary force $\boldsymbol{f}$ acting at the point $\boldsymbol{\xi}$ in the j-direction (Eringen and Suhubi, 1975). Furthermore, the amplitude of the displacement is affected by the source-receiver distance $r$ and the conceptual body force strength. The first term of equation 2.42 is called a near-field term and decays rapidly away from the source due to the higher power of $r$. The other two terms are the P and S far-field terms, respectively,and they are more dominant and decay slower than the near-field with distance from the source. Notice that the shear wave displacement in equation 2.41 refers to a general transverse waves without indication to the polarization; i.e., SV or SH waves. The following subsection will define and separate the SH and SV components of the wave equation utilizing the effective source from the conceptual body force model.

### 2.2.2 Separation of the Body Force S potential into SV and SH components

In the previous subsections, the displacement field was separated into the gradient of scalar potential and curl of the vector potential using the Helmholtz decomposition. As mentioned earlier, this decomposition is useful for seeking solutions to the displacement field and when accounting to satisfy boundary conditions. Applying boundary conditions on a vector field is often done through scalar fields. Generally, any vector field can be represented by 3 scalar fields (Morse and Feshbach, 1953). The potential wave equations 2.18 and 2.19 results in 1 scalar and 3 vector potential equations; respectively. Therefore, to rewrite the displacement vector field into 3 scalar fields then

the vector potential equation 2.19 must be reduced into 2 scalar potential equations. Indeed, only 2 scalar potential equations are required instead of 3 because the auxiliary condition; i.e., $\nabla \cdot \boldsymbol{\psi} = 0$, reduces the independent quantities needed to specify the vector potential wave equation. Therefore, the potential wave equations 2.18 and 2.19 can be represented by the following 3 scalar equations

$$\ddot{\phi} = \frac{\Phi}{\rho} + \alpha^2 \nabla^2 \phi, \tag{2.43}$$

$$\frac{d^2}{dt^2}(\nabla \times \boldsymbol{\psi})_z = \frac{(\nabla \times \boldsymbol{\Psi})_z}{\rho} + \beta^2 \nabla^2 [(\nabla \times \boldsymbol{\psi})_z], \tag{2.44}$$

$$\ddot{\psi}_z = \frac{\Psi_z}{\rho} + \beta^2 \nabla^2 \psi_z. \tag{2.45}$$

The three scalar fields decomposition utilize the Cartesian coordinates where the vertical axes is the z-axis. Equations 2.43, 2.44, and 2.45 can be rewritten as

$$\ddot{\phi} = \frac{\Phi}{\rho} + \alpha^2 \nabla^2 \phi, \tag{2.46}$$

$$\ddot{\psi} = \frac{\Psi}{\rho} + \beta^2 \nabla^2 \psi, \tag{2.47}$$

$$\ddot{\chi} = \frac{X}{\rho} + \beta^2 \nabla^2 \chi, \tag{2.48}$$

where

$$\begin{aligned} \psi &= (\nabla \times \boldsymbol{\psi})_z = \frac{\partial \psi_y}{\partial_x} - \frac{\partial \psi_x}{\partial_y}, & \Psi &= (\nabla \times \boldsymbol{\Psi})_z = \frac{\partial \Psi_y}{\partial_x} - \frac{\partial \Psi_x}{\partial_y}, \\ \chi &= \psi_z, & X &= \Psi_z. \end{aligned} \tag{2.49}$$

The scalar fields from equations 2.46, 2.47, and 2.48 represent the scalar field decomposition for a general case with an arbitrary body force. It is immediately apparent that equation 2.46 is the P scalar wave equation following from equation 2.18. The physical meaning of the scalar potential

$\phi$ can be deduced from

$$\begin{aligned}\nabla \cdot \boldsymbol{u} &= \nabla \cdot (\nabla \phi)\,, \\ &= \nabla^2 \phi,\end{aligned}$$

where the double spatial derivative of $\phi$ is the divergence of the displacement field. This means that $\phi$ represents the dilatation in a given volume; i.e., the relative change of a volume, or area in 2D, due to deformation.From equation 2.19, equations 2.47 and 2.48 represent the two independent S scalar wave equation that fully describe the vector potential wave equation. The physical meaning of the vector potential $\boldsymbol{\psi}$ can be deduced from

$$\begin{aligned}\nabla \times \boldsymbol{u} &= \nabla \times \nabla \times \boldsymbol{\psi}, \\ &= -\nabla^2 \boldsymbol{\psi},\end{aligned}$$

where the double spatial derivative of $\boldsymbol{\psi}$ is the rotation of the displacement field. This means that $\boldsymbol{\psi}$ represents the shape change in a given volume, or an area in 2D, due to the rotation. The physical meaning of $\psi$ from equation 2.47 is the rotation in the planes parallel to the z-axis; whereas, the physical meaning of $\chi$ from equation 2.48 is the rotation in the plane perpendicular to the z-axis. The scalar equations 2.46, 2.47, and 2.48 will first be analyzed in the absence of body forces. In the absence of body forces, in addition to the trivial solution, only 1 motion is independent and 2 must vanish everywhere from the scalar equations. Starting with equation 2.46, the motion will be analyzed assuming $\psi_x = \psi_y = \psi_z = 0$, then the displacement is

$$\begin{aligned}\boldsymbol{u} &= \nabla \phi = \left( \frac{\partial \phi}{\partial x}, \frac{\partial \phi}{\partial y}, \frac{\partial \phi}{\partial z} \right), \\ \nabla \cdot \boldsymbol{u} &= \frac{\partial^2 \phi}{\partial x^2} + \frac{\partial^2 \phi}{\partial y^2} + \frac{\partial^2 \phi}{\partial z^2} \neq 0, \\ \nabla \times \boldsymbol{u} &= \left( \underbrace{\frac{\partial^2 \phi}{\partial y \partial z} - \frac{\partial^2 \phi}{\partial z \partial y}}_{=0}, \underbrace{\frac{\partial^2 \phi}{\partial x \partial z} - \frac{\partial^2 \phi}{\partial x \partial z}}_{=0}, \underbrace{\frac{\partial^2 \phi}{\partial x \partial y} - \frac{\partial^2 \phi}{\partial y \partial x}}_{=0} \right) = 0.\end{aligned} \tag{2.50}$$

Motion from equation 2.50 is characterized by $\nabla \cdot \boldsymbol{u} \neq 0$ and $\nabla \times \boldsymbol{u} = 0$. Since the rotation of the displacement is zero and the wave propagates with velocity $\alpha$, then equation 2.46 represents P waves. Analysis of the second scalar wave equation 2.47 assumes $\phi = 0$, $\chi = 0$, and involves $\nabla \cdot \boldsymbol{\psi} = 0$. Only in the special case $\psi_z = 0$ then there exists a condition for a scalar function $\gamma$ such that

$$
\begin{aligned}
\boldsymbol{\psi} &= \nabla \times (0, 0, \gamma) = \left( \frac{\partial \gamma}{\partial y}, -\frac{\partial \gamma}{\partial x}, 0 \right), \\
\boldsymbol{u} &= \nabla \times \boldsymbol{\psi} = \left( \frac{\partial^2 \gamma}{\partial z \partial x}, \frac{\partial^2 \gamma}{\partial z \partial y}, -\frac{\partial^2 \gamma}{\partial x^2} - \frac{\partial^2 \gamma}{\partial y^2} \right), \\
\nabla \cdot \boldsymbol{u} &= \frac{\partial^3 \gamma}{\partial x^2 \partial z} + \frac{\partial^3 \gamma}{\partial y^2 \partial z} - \frac{\partial^3 \gamma}{\partial x^2 \partial z} - \frac{\partial^3 \gamma}{\partial y^2 \partial z} = 0, \\
\nabla \times \boldsymbol{u} &= \left( \frac{\partial}{\partial y} \left[ -\frac{\partial^2 \gamma}{\partial x^2} - \frac{\partial^2 \gamma}{\partial y^2} \right] - \frac{\partial^3 \gamma}{\partial z^2 \partial y}, -\frac{\partial}{\partial x} \left[ -\frac{\partial^2 \gamma}{\partial x^2} - \frac{\partial^2 \gamma}{\partial y^2} \right] + \frac{\partial^3 \gamma}{\partial z^2 \partial x}, \underbrace{\frac{\partial^3 \gamma}{\partial z \partial y \partial x} - \frac{\partial^3 \gamma}{\partial z \partial y \partial x}}_{(\nabla \times \boldsymbol{u})_z = 0} \right)
\end{aligned}
\tag{2.51}
$$

Motion from equation 2.51 is characterized by $\nabla \cdot \boldsymbol{u} = 0$, $(\nabla \times \boldsymbol{u})_z = 0$, and $u_z \neq 0$. With this characterization and the fact that the wave travels with velocity $\beta$ then the scalar wave equation 2.47 represents SV waves. It is important to note that the scalar function $\gamma$ exists if and only if $\chi = \psi_z = 0$. Generally, $\gamma \neq \psi$ and $\psi$ is defined as in equation 2.49. Analysis of the third scalar wave equation 2.48 involves $\phi = 0$ and $\psi = 0$, then the displacement is

$$
\begin{aligned}
\boldsymbol{u} &= \nabla \times (0, 0, \chi) = \left( \frac{\partial \chi}{\partial y}, -\frac{\partial \chi}{\partial x}, \underbrace{0}_{u_z = 0} \right), \\
\nabla \cdot \boldsymbol{u} &= \frac{\partial^2 \chi}{\partial x \partial y} - \frac{\partial^2 \chi}{\partial x \partial y} = 0, \\
\nabla \times \boldsymbol{u} &= \left( \frac{\partial^2 \chi}{\partial x \partial z}, \frac{\partial^2 \chi}{\partial y \partial z}, \underbrace{-\frac{\partial^2 \chi}{\partial x^2} - \frac{\partial^2 \chi}{\partial y^2}}_{(\nabla \times \boldsymbol{u})_z \neq 0} \right).
\end{aligned}
\tag{2.52}
$$

Motion from equation 2.52 is characterized by $\nabla \cdot \boldsymbol{u} = 0$, $u_z = 0$, and $(\nabla \times \boldsymbol{u})_z \neq 0$. Given this characterization and the fact that the wave travels with velocity $\beta$ then the scalar wave equation 2.48 represents SH waves. Now that the independent scalar waves have been characterized and their respective motions described, then the presence of the body force will be considered. More specifically, the conceptual body force model will be used to identify and separate the S wave motions only and no further assessment of P waves is necessary; this analysis will be carried out in different case scenarios.

***Case 1: Vertical Body Force, f =*** *(0,0,$f_z$)*

Considering the body force in the vertical direction only which is defined as

$$\boldsymbol{f} = \frac{A}{h^2}\delta(x)S(t)(0,0,1), \tag{2.53}$$

then substituting equation 2.53 into 2.21 yields

$$\boldsymbol{W} = -\frac{AS(t)}{4\pi r h^2}(0,0,1) = -W_z \boldsymbol{z}, \tag{2.54}$$

where $W_z = \dfrac{AS(t)}{4\pi r h^2}$.Using equation 2.54, the body force S potential becomes

$$\boldsymbol{\Psi} = -\nabla \times \boldsymbol{W} = \left( \underbrace{\frac{\partial W_z}{\partial y}}_{\Psi_x}, -\underbrace{\frac{\partial W_z}{\partial x}}_{\Psi_y}, \underbrace{0}_{\Psi_z} \right) \tag{2.55}$$

Since $X = \Psi_z = 0$ then the vertical body force does not excite SH waves. From the body force potential of equation 2.55, the S wave body force is defined as

$$\boldsymbol{f^S} = \nabla \times \boldsymbol{\Psi}. \tag{2.56}$$

Combining equation 2.55 with equation 2.56 yields

$$\boldsymbol{f^S} = \nabla \times \boldsymbol{\Psi} = \left( \frac{\partial^2 W_z}{\partial z \partial x}, \frac{\partial^2 W_z}{\partial z \partial y}, \underbrace{-\frac{\partial^2 W_z}{\partial x^2} - \frac{\partial^2 W_z}{\partial y^2}}_{\boldsymbol{f_z^S \neq 0}} \right) \tag{2.57}$$

Since $\boldsymbol{f_z^S} \neq 0$ then $\boldsymbol{f^S}$ from equation 2.57 for the vertical body force meets one criteria for the characterization of SV wave generation. In order to fully characterize the body force as the SV body force then the curl of equation 2.57 in the vertical direction must be zero as

$$(\nabla \times \boldsymbol{f^S})_z = \frac{\partial^3 W_z}{\partial z \partial y \partial x} - \frac{\partial^3 W_z}{\partial z \partial y \partial x} = 0. \tag{2.58}$$

Therefore, the vertical force from the conceptual body force does not excite SH waves; instead, only excites SV waves. Moreover, the vertical body force fully satisfies the condition for SV wave generation which means that the body force from equation 2.56 is the SV body force $\boldsymbol{f^{SV}} = \boldsymbol{f^S}$. Further analysis will involve the horizontal forces, which will include multiple cases to form a comprehensive analysis of the body force.

***Case 2: Horizontal Body Force, f =*** *($f_x$,0,0)*

For this case, the horizontal force is defined as

$$\boldsymbol{f} = \frac{AS(t)}{h^2} \delta(x)(-\nu, 0, 0), \tag{2.59}$$

Generally, the horizontal force in the conceptual model is directly related to the Poisson ratio, $\nu$, and the distance from source, $h$, unlike the vertical force which is related only to the distance from the source. Substituting equation 2.59 into 2.21 yields the equivalent

$$\boldsymbol{W} = -\left( -\frac{\nu AS(t)}{4\pi r h^2}, 0, 0 \right) = -W_H \boldsymbol{x}, \tag{2.60}$$

where $W_H = \dfrac{-\nu A S(t)}{4\pi r h^2}$. Using equation 2.60, the body force S potential becomes

$$\boldsymbol{\Psi} = -\nabla \times \boldsymbol{W} = \left(0, \frac{\partial W_H}{\partial z}, -\frac{\partial W_H}{\partial y}\right). \tag{2.61}$$

From the previous equation, $X = \Psi_z \neq 0$ which is one of the conditions for the existence of the SH waves. However, the body force S potential involve $\Psi = (\nabla \times \Psi)_z \neq 0$ which is due to either $\Psi_x$, $\Psi_y$, or both not equal to zero which is one of the conditions for the existence of SV waves. For further analysis, the body force S potential from equation 2.61 will be separated as such

$$\boldsymbol{\Psi} = \boldsymbol{\Psi_1} + \boldsymbol{\Psi_2}, \tag{2.62}$$

$$\boldsymbol{f^S} = \boldsymbol{f^{S1}} + \boldsymbol{f^{S2}} \tag{2.63}$$

where

$$\boldsymbol{\Psi_1} = \left(0, \frac{\partial W_H}{\partial z}, 0\right), \tag{2.64}$$

and

$$\boldsymbol{\Psi_2} = \left(0, 0, -\frac{\partial W_H}{\partial y}\right), \tag{2.65}$$

If equation 2.64 satisfy the generation of SV waves then it must be characterized as

$$\boldsymbol{f^{S1}} = \nabla \times \boldsymbol{\Psi_1} = \left(-\frac{\partial^2 W_H}{\partial z^2}, 0, \frac{\partial^2 W_H}{\partial x \partial z}\right), \tag{2.66}$$

and

$$(\nabla \times \boldsymbol{f^{S1}})_z = \frac{\partial^3 W_H}{\partial z^2 \partial y} \neq 0. \tag{2.67}$$

From the previous equations, $\boldsymbol{f^{S1}}$ characterization for SV waves involves $\boldsymbol{f_z^{S1}} \neq 0$ but $(\nabla \times \boldsymbol{f^{S1}})_z = 0$. Since $(\nabla \times \boldsymbol{f^{S1}})_z \neq 0$ then $\boldsymbol{f^{S1}}$ does not fully satisfy the generation of SV waves; hence, $\boldsymbol{f^{SV}} \neq \boldsymbol{f^{S1}}$. This indicates that the horizontal body force (x-component) from the conceptual model generates an S wave like motion from $\boldsymbol{f^{S1}}$ that does not satisfy either an SV or an SH

wave motion. On the other hand, waves generated from $\boldsymbol{f^{S2}}$ can be characterized like SH wave, since $X = \Psi_z \neq 0$, as follows

$$\boldsymbol{f^{S2}} = \nabla \times \boldsymbol{\Psi_2} = \left( -\frac{\partial^2 W_H}{\partial y^2}, \frac{\partial^2 W_H}{\partial x \partial y}, 0 \right), \tag{2.68}$$

and

$$(\nabla \times \boldsymbol{f^{S2}})_z = \frac{\partial^3 W_H}{\partial x^2 \partial y} + \frac{\partial^3 W_H}{\partial y^3} \neq 0. \tag{2.69}$$

From the previous equations, $\boldsymbol{f^{S2}}$ characterization for SH waves involve $\boldsymbol{f_z^{S2}} = 0$ and $(\nabla \times \boldsymbol{f^{S2}})_z \neq 0$. Meeting these conditions means that the horizontal body force (x-component) excited from $\boldsymbol{f^{S2}}$ does fully satisfy and generate SH waves; thus, $\boldsymbol{f^{SH}} = \boldsymbol{f^{S2}}$.

***Case 3: Horizontal Body Force, f = (0,$f_y$,0)***

Similarly, the horizontal force for this case is defined as

$$\boldsymbol{f} = \frac{AS(t)}{h^2} \delta(x)(0, -\nu, 0), \tag{2.70}$$

Substituting equation 2.70 into 2.21 yields the equivalent

$$\boldsymbol{W} = -\left( 0, -\frac{\nu AS(t)}{4\pi r h^2}, 0 \right) = -W_H \boldsymbol{y}, \tag{2.71}$$

where $W_H = \dfrac{-\nu AS(t)}{4\pi r h^2}$. Using equation 2.71, the body force S potential becomes

$$\boldsymbol{\Psi} = -\nabla \times \boldsymbol{W} = \left( -\frac{\partial W_H}{\partial z}, 0, \frac{\partial W_H}{\partial x} \right), \tag{2.72}$$

From the previous equation, $X = \Psi_z \neq 0$ and $\Psi = (\nabla \times \Psi)_z \neq 0$. Those two criteria lead to different body force S potentials which can be separated using equations 2.62 and 2.63 resulting in

$$\boldsymbol{\Psi_1} = \left( -\frac{\partial W_H}{\partial z}, 0, 0 \right), \tag{2.73}$$

and

$$\boldsymbol{\Psi_2} = \left(0, 0, \frac{\partial W_H}{\partial x}\right), \tag{2.74}$$

If equation 2.73 satisfy the generation of SV waves then it must be characterized as

$$\boldsymbol{f^{S1}} = \nabla \times \boldsymbol{\Psi_1} = \left(0, -\frac{\partial^2 W_H}{\partial^2 z^2}, \frac{\partial^2 W_H}{\partial y \partial z}\right), \tag{2.75}$$

and

$$(\nabla \times \boldsymbol{f^{S1}})_z = -\frac{\partial^3 W_H}{\partial z^2 \partial x} \neq 0, \tag{2.76}$$

From the previous equations, $\boldsymbol{f^{S1}}$ characterization for SV waves involves $\boldsymbol{f_z^{S1}} \neq 0$ but $(\nabla \times \boldsymbol{f^{S1}})_z = 0$. Since $(\nabla \times \boldsymbol{f^{S1}})_z \neq 0$ then $\boldsymbol{f^{S1}}$ does not fully satisfy the generation of SV waves; hence, $\boldsymbol{f^{SV}} \neq \boldsymbol{f^{S1}}$. This indicates that the horizontal body force (y-component) from the conceptual model generates an S wave like motion from $\boldsymbol{f^{S1}}$ that does not satisfy either an SV or an SH wave motion. On the other hand, waves generated from $\boldsymbol{f^{S2}}$ can be characterized like SH wave, since $X = \Psi_z \neq 0$, as follows

$$\boldsymbol{f^{S2}} = \nabla \times \boldsymbol{\Psi_2} = \left(\frac{\partial^2 W_H}{\partial x \partial y}, -\frac{\partial^2 W_H}{\partial^2 x^2}, 0\right), \tag{2.77}$$

and

$$(\nabla \times \boldsymbol{f^{S2}})_z = -\frac{\partial^3 W_H}{\partial x^3} - \frac{\partial^3 W_H}{\partial y^2 \partial x} \neq 0, \tag{2.78}$$

From the previous equations, $\boldsymbol{f^{S2}}$ characterization for SH waves involve $\boldsymbol{f_z^{S2}} = 0$ and $(\nabla \times \boldsymbol{f^{S2}})_z \neq 0$. Meeting these conditions means that the horizontal body force (y-component) excited from $\boldsymbol{f^{S2}}$ does fully satisfy and generate SH waves; thus, $\boldsymbol{f^{SH}} = \boldsymbol{f^{S2}}$.

***Case 4: Horizontal Body Force, f =*** *($f_x$,$f_y$,0)*

Similarly, the horizontal force for this case is defined as

$$\boldsymbol{f} = \frac{AS(t)}{h^2}\delta(x)(-\nu, -\nu, 0), \tag{2.79}$$

Substituting equation 2.70 into 2.21 yields the equivalent

$$\boldsymbol{W} = -\left(-\frac{\nu AS(t)}{4\pi r h^2}, -\frac{\nu AS(t)}{4\pi r h^2}, 0\right) = -W_H \boldsymbol{x} - W_H \boldsymbol{y}, \tag{2.80}$$

where $W_H = \dfrac{-\nu AS(t)}{4\pi r h^2}$. Using equation 2.80, the body force S potential becomes

$$\boldsymbol{\Psi} = -\nabla \times \boldsymbol{W} = \left(-\frac{\partial W_H}{\partial z}, \frac{\partial W_H}{\partial z}, \frac{\partial W_H}{\partial x} - \frac{\partial W_H}{\partial y}\right). \tag{2.81}$$

From the previous equation, $X = \Psi_z \neq 0$ and $\Psi = (\nabla \times \Psi)_z \neq 0$. Those two criteria lead to different body force S potentials which can be separated using equations 2.62 and 2.63 resulting in

$$\boldsymbol{\Psi_1} = \left(-\frac{\partial W_H}{\partial z}, \frac{\partial W_H}{\partial z}, 0\right), \tag{2.82}$$

and

$$\boldsymbol{\Psi_2} = \left(0, 0, \frac{\partial W_H}{\partial x} - \frac{\partial W_H}{\partial y}\right). \tag{2.83}$$

If equation 2.82 satisfy the generation of SV waves then it must be characterized as

$$\boldsymbol{f^{S1}} = \nabla \times \boldsymbol{\Psi_1} = \left(-\frac{\partial^2 W_H}{\partial z^2}, -\frac{\partial W_H}{\partial z^2}, \frac{\partial^2 W_H}{\partial z \partial x} + \frac{\partial^2 W_H}{\partial z \partial y}\right), \tag{2.84}$$

and

$$(\nabla \times \boldsymbol{f^{S1}})_z = \frac{\partial^3 W_H}{\partial z^2 \partial y} - \frac{\partial^3 W_H}{\partial z^2 \partial x} \neq 0. \tag{2.85}$$

From the previous equations, $\boldsymbol{f^{S1}}$ characterization for SV waves involves $\boldsymbol{f_z^{S1}} \neq 0$ but $(\nabla \times \boldsymbol{f^{S1}})_z = 0$. Since $(\nabla \times \boldsymbol{f^{S1}})_z \neq 0$ then $\boldsymbol{f^{S1}}$ does not fully satisfy the generation of SV waves; hence, $\boldsymbol{f^{SV}} \neq \boldsymbol{f^{S1}}$. This indicates that the horizontal body force (x and y components) from the conceptual model generates an S wave like motion from $\boldsymbol{f^{S1}}$ that does not satisfy either an SV or an SH wave motion. On the other hand, waves generated from $\boldsymbol{f^{S2}}$ can be characterized like SH

wave, since $X = \Psi_z \neq 0$, as follows

$$\boldsymbol{f^{S2}} = \nabla \times \boldsymbol{\Psi_2} = \left( \frac{\partial}{\partial y}[V], -\frac{\partial}{\partial x}[V], 0 \right), \tag{2.86}$$

and

$$(\nabla \times \boldsymbol{f^{S2}})_z = -\frac{\partial^2}{\partial x^2}[V] - \frac{\partial^2}{\partial y^2}[V] \neq 0, \tag{2.87}$$

where $V = \dfrac{\partial W_H}{\partial x} - \dfrac{\partial W_H}{\partial y}$. From the previous equations, $\boldsymbol{f^{S2}}$ characterization for SH waves involve $\boldsymbol{f_z^{S2}} = 0$ and $(\nabla \times \boldsymbol{f^{S2}})_z \neq 0$. Meeting these conditions means that the horizontal body force (x and y components) excited from $\boldsymbol{f^{S2}}$ does fully satisfy and generate SH waves; thus, $\boldsymbol{f^{SH}} = \boldsymbol{f^{S2}}$.With the conclusion of the horizontal body forces analysis, it is evident that one or a combination of both of the horizontal body forces satisfy the condition to generate SH waves.

***Explicit Form of the Body Force Potentials***

In this section, the initial analysis involved reducing the scalar and vector potential wave equations into 3 independent scalar wave equations. In the absence of the body forces, the motions from each of the scalar equation satisfy a single body wave type only; namely, P, SV, and SH waves. In the presence of the body forces, P, SV, and SH waves can be generated successfully using the conceptual body force model. Using the equivalent force from the body force model, the body force potentials from equations 2.46, 2.47, and 2.48 are then explicitly defined as

$$\Phi = \frac{AS(t)}{4\pi h^2}\left( \nu \frac{\partial}{\partial x}\frac{1}{r} + \nu \frac{\partial}{\partial y}\frac{1}{r} - \frac{\partial}{\partial z}\frac{1}{r} \right), \tag{2.88}$$

$$\Psi = \frac{AS(t)}{4\pi h^2}\left( -\frac{\partial^2}{\partial x^2}\frac{1}{r} - \frac{\partial^2}{\partial y^2}\frac{1}{r} \right), \tag{2.89}$$

$$X = \frac{\nu AS(t)}{4\pi h^2}\left( -\frac{\partial}{\partial x}\frac{1}{r} + \frac{\partial}{\partial y}\frac{1}{r} \right). \tag{2.90}$$

The previous three equations represent the explicit body force potential defined from an arbitrary body force which in the shallow waters of the Arabian Gulf is the effective source. These equations together with equations 2.46, 2.47, and 2.48 represent the three independent scalar wave equations

for P, SV, and SH wave motions with a unique body force to generate each motion. In Aki and Richards (2002), they mentioned that three types of scalar wave equations exist for P, SV, and SH and are described by a body force that can be decomposed as $\boldsymbol{f} = \nabla\Phi + \nabla \times \nabla \times (0, 0, \Psi) + \nabla \times (0, 0, X)$. However, this decomposition does not hold for an arbitrary body force because SV and SH waves are not simultaneously generated from the same force component, as demonstrated in the previous body force analysis. Further, to uncouple P-SV and SH motion then the gauge condition $\nabla \cdot \boldsymbol{\psi} = 0$ must be satisfied. For this condition to be satisfied, the Neumann condition $\nabla \cdot \boldsymbol{\psi} = \dfrac{\partial \chi}{\partial z} = 0$ must be true, which is not necessarily true (Meredith et al.,1990). In general, P-SV and SH motion are completely coupled if no symmetry is assumed (Pilant, 1979). Therefore, the three independent scalar wave equations that are decomposed in Aki and Richards (2002, Box 6.5) is not for a general arbitrary body force; instead, for a specific force only.

### 2.2.3 Boundary Conditions

With the wave equation separated into 3 distinct scalar wave equations, then it remains to apply boundary conditions on the scalar wave equations to verify the existence of the wave motions and the independence of P-SV and SH motions. Given the vertical axis is defined as the z-axis, the boundary conditions will be considered assuming a horizontal material discontinuity at a solid-solid interface encountered within Earth's medium. The boundary conditions the wave motions must satisfy are the displacement and traction continuity conditions because at the interface the displacement and tractions are constrained. Since the interface is assumed to be between two solids, all components of the displacement are continuous because no overlaps or tears occur which in turn requires the tractions to be continuous (Stein and Wysession, 2009). The total displacement from the scalar potentials is

$$\boldsymbol{u} = \boldsymbol{u^P} + \boldsymbol{u^{SV}} + \boldsymbol{u^{SH}} \tag{2.91}$$

with

$$\begin{aligned} u_x &= u_x^P + u_x^{SV} + u_x^{SH} \\ &= \frac{\partial \phi}{\partial x} + \frac{\partial^2 \psi}{\partial x \partial z} + \frac{\partial \chi}{\partial y}, \end{aligned} \tag{2.92}$$

$$\begin{aligned} u_y &= u_y^P + u_y^{SV} + u_y^{SH} \\ &= \frac{\partial \phi}{\partial y} + \frac{\partial^2 \psi}{\partial y \partial z} - \frac{\partial \chi}{\partial x}, \end{aligned} \tag{2.93}$$

$$\begin{aligned} u_z &= u_z^P + u_z^{SV} \\ &= \frac{\partial \phi}{\partial z} - \left( \frac{\partial^2 \psi}{\partial x^2} + \frac{\partial^2 \psi}{\partial y^2} \right). \end{aligned} \tag{2.94}$$

For a horizontal discontinuity, the three scalar conditions of displacement continuity can be differentiated in horizontal directions to satisfy the kinematic boundary condition (Aki and Richards, 2002). Those conditions are

$$(\nabla \times \boldsymbol{u})_z, \tag{2.95}$$

$$\nabla \cdot \boldsymbol{u} - \frac{\partial u_z}{\partial z}, \tag{2.96}$$

$$u_z. \tag{2.97}$$

Substituting equation 2.91 into equations 2.95, 2.96, and 2.97 yields

$$\begin{aligned} (\nabla \times \boldsymbol{u})_z &= \left( -\frac{\partial^2 \chi}{\partial x^2} + \cancel{\frac{\partial^3 \psi}{\partial x \partial y \partial z}} + \cancel{\frac{\partial^2 \phi}{\partial x \partial y}} - \cancel{\frac{\partial^3 \psi}{\partial x \partial y \partial z}} - \cancel{\frac{\partial^2 \phi}{\partial x \partial y}} - \frac{\partial^2 \chi}{\partial y^2} \right) \\ &= \left( -\frac{\partial^2 \chi}{\partial x^2} - \frac{\partial^2 \chi}{\partial y^2} \right), \end{aligned} \tag{2.98}$$

$$\begin{aligned} \nabla \cdot \boldsymbol{u} - \frac{\partial u_z}{\partial z} &= \frac{\partial^2 \phi}{\partial x^2} + \frac{\partial^3 \psi}{\partial x^2 \partial z} + \cancel{\frac{\partial^2 \chi}{\partial x \partial y}} + \frac{\partial^2 \phi}{\partial y^2} + \frac{\partial^3 \psi}{\partial y^2 \partial z} - \cancel{\frac{\partial^2 \chi}{\partial x \partial y}} \\ &= \frac{\partial^2 \phi}{\partial x^2} + \frac{\partial^3 \psi}{\partial x^2 \partial z} + \frac{\partial^2 \phi}{\partial y^2} + \frac{\partial^3 \psi}{\partial y^2 \partial z}, \end{aligned} \tag{2.99}$$

$$u_z = \frac{\partial \phi}{\partial z} - \left( \frac{\partial^2 \psi}{\partial x^2} + \frac{\partial^2 \psi}{\partial y^2} \right). \tag{2.100}$$

The displacement boundary conditions from equations 2.95, 2.96, and 2.97 represent the conditions where the vertical z-direction is normal to the horizontal interface that spans the x-y plane. The first displacement condition from equation 2.95 states that the rotation in the vertical direction is perpendicular to the interface. This rotation is characterized by in-plane rotation in the x-y plane and it must be continuous if the displacement is continuous. The second displacement condition from equation 2.96 states that the particle motion flow in the vertical direction is perpendicular to the interface. This flow is characterized by an in-plane displacement flow in the x-y plane and must be satisfied if the displacements are continuous across the interface. The third displacement condition from equation 2.97 simply states the continuity of the vertical displacement across the interface must be satisfied for the continuity condition. These equations demonstrate that P-SV waves are independent of SH waves at the boundary. Further, the P and SV potentials contribute to the same continuity conditions of $\nabla \cdot \boldsymbol{u}$ and $u_z$; thus, forming a coupled system. Conversely, SH waves contribute to a different continuity condition and is decoupled from P and SV waves. This indicates that the SH potential generated from the body force potential is indeed an SH wave because the other continuity conditions; i.e., $\nabla \cdot \boldsymbol{u}$ and $u_z$, remain zero after interaction with the boundary, so that SH waves remain SH. The boundary conditions also involve tractions continuity. Since the normal to the interface has only a $\boldsymbol{z}$ component,

$$\boldsymbol{n} = (0, 0, 1), \qquad n_j = \delta_{j3} \tag{2.101}$$

and the tractions on the interface are given by

$$T_i = \tau_{ij} n_j = \tau_{i3} = (\tau_{xz}, \tau_{yz}, \tau_{zz}). \tag{2.102}$$

Using equations 2.10, 2.13, and 2.91, the stress components from the traction vector in equation 2.102 can be found as follows

$$\tau_{xz} = \mu \left[ 2\frac{\partial^2 \phi}{\partial x \partial z} - \frac{\partial}{\partial x}\left( \nabla^2 \psi - 2\frac{\partial^2 \psi}{\partial z^2} \right) + \frac{\partial^2 \chi}{\partial y \partial z} \right], \tag{2.103}$$

$$\tau_{yz} = \mu \left[ 2\frac{\partial^2 \phi}{\partial y \partial z} - \frac{\partial}{\partial y}\left( \nabla^2 \psi - 2\frac{\partial^2 \psi}{\partial z^2} \right) - \frac{\partial^2 \chi}{\partial x \partial z} \right], \tag{2.104}$$

$$\tau_{zz} = \lambda \nabla^2 \phi + 2\mu \left[ \frac{\partial^2 \phi}{\partial z^2} - \frac{\partial}{\partial z}\left( \nabla^2 \psi - \frac{\partial^2 \psi}{\partial z^2} \right) \right]. \tag{2.105}$$

The scalar potentials satisfy the traction continuity conditions. Moreover, the normal stress follows directly from the normal displacement of equation 2.100, where the P-SV waves are coupled but the SH wave vanishes identically. To demonstrate the uncoupling of SH from P-SV waves for the dynamic boundary conditions, then the horizontal derivatives are taken across the interface for equations 2.103 and 2.104 and then combined. Therefore, the continuity of traction implies the continuity of

$$\mu \frac{\partial}{\partial z} \left[ (\nabla \times \boldsymbol{u})_z \right] = \mu \frac{\partial}{\partial z} \left[ -\frac{\partial^2 \chi}{\partial x^2} - \frac{\partial^2 \chi}{\partial y^2} \right], \tag{2.106}$$

$$\mu \left[ \frac{\partial}{\partial z} \nabla \cdot \boldsymbol{u} - 2\frac{\partial^2 u_z}{\partial z^2} + \nabla^2 u_z \right] = \mu \left[ 2\frac{\partial}{\partial z}\left( \frac{\partial^2 \phi}{\partial x^2} + \frac{\partial^2 \phi}{\partial y^2} \right) + \left( -\frac{\partial^2}{\partial x^2} - \frac{\partial^2}{\partial y^2} \right)\left( \nabla^2 \psi - 2\frac{\partial^2 \psi}{\partial z^2} \right) \right], \tag{2.107}$$

$$\lambda \nabla \cdot \boldsymbol{u} + 2\mu \frac{\partial u_z}{\partial z} = \lambda \nabla^2 \phi + 2\mu \left[ \frac{\partial^2 \phi}{\partial z^2} - \frac{\partial}{\partial z}\left( \nabla^2 \psi - \frac{\partial^2 \psi}{\partial z^2} \right) \right]. \tag{2.108}$$

From the previous equations, the SH wave satisfies the continuity of equations 2.107 and 2.108 trivially since $(\nabla \times \boldsymbol{u})_z \neq 0$ but $u_z = 0$ and $\nabla \cdot \boldsymbol{u} = 0$. With the satisfaction of equation 2.106 continuity condition, SH waves does satisfy the dynamic boundary conditions that is uncoupled from P and SV waves. However, the coupling of $u_z = 0$ and $\nabla \cdot \boldsymbol{u} = 0$ for equations 2.107 and 2.108 implies the coupling of P and SV waves for the dynamic boundary condition as well.

# 3. PROPAGATION OF SHEAR WAVES ACROSS A HORIZONTAL BOUNDARY

In the shallow marine environment of the Arabian Gulf, the general ray theory does not describe the wave propagation adequately. In fact, the problem in such setting is a mechanical problem and the effective source at the hard sea-bottom is responsible for generating P, SV, and SH waves. Further, since the waves cannot be approximated as plane waves then accurate estimation of the wave amplitudes is necessary. In this chapter, the propagation of the different wave types will be considered in a heterogeneous medium using the exact analytical solution of the Cagniard-de Hoop method (De Hoop, 1960) utilizing the effective source from conceptual body force model.

## 3.1 Analytical Solutions of the Wave Equation in a Heterogeneous Medium using the Conceptual Body Force Model

The Cagniard de-Hoop employs time domain solutions for the wave equation and provides an exact analytical computation of the wavefield at any given point without approximations. For this reason, it will be the preferred method to solve the wave equation. Also, the analytical analysis will be carried out in 2D which involves a line source geometry as shown in figure 3.1.

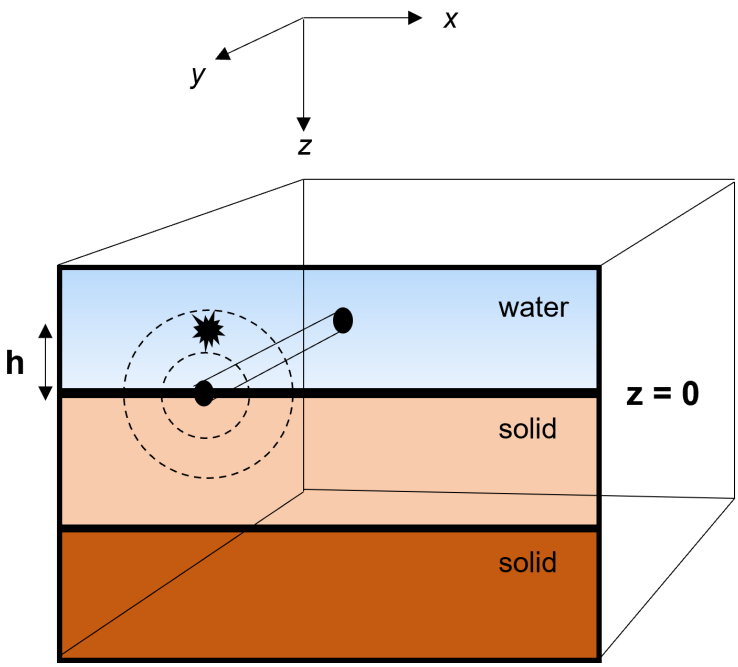


Figure 3.1: Two-dimensional geometry of the line source problem. The sea-bottom interface is located at depth $z = 0$ and the vertical distance from the effective source to the explosive airgun source is $h$. All derivatives in the y direction are zero.

Given the configuration, the direct wave from the source travels a vertical distance of $|z - h|$; whereas the reflected wave travels a vertical distance of $|z + h|$. The following sub sections will utilize the Cagniard de-Hoop method and the effective source from the conceptual model to analytically solve for the SH, P, and SV waves in heterogeneous medium. The Cagniard de-Hoop derivation in the following subsections will follow the line source derivation method by Aki and Richards (2002) with the main difference of utilizing the correct effective source term from the conceptual body force model.

### 3.1.1 SH Wave Solution using the Cagniard de-Hoop Method

In the two-dimensional line source problem, the derivatives in terms of the y direction are zero. From equations 2.92 and 2.93, the SH potential only excites the y component of displacement; i.e., $u_y$. Therefore, the SH wave equation, in this scenario, is characterized by

$$\begin{aligned} u_x = u_z = 0, \\ u_y \neq 0, \\ \frac{\partial u_y}{\partial y} = 0. \end{aligned} \tag{3.1}$$

Substituting equation 3.1 into equation 2.15 yields

$$\begin{aligned} \rho \frac{\partial^2 u_y}{\partial t^2} = \mu \left[ \frac{\partial^2 u_y}{\partial z^2} + \frac{\partial^2 u_y}{\partial x^2} \right] f_y, \qquad or, \\ \ddot{u_y} = \frac{u_y}{\rho} + \beta^2 \nabla^2 u_y, \end{aligned} \tag{3.2}$$

where $f_y$ is the body force that excites the SH waves and for an impulsive line source is defined as

$$f_y = \frac{-\nu A}{h^2} \delta(x)\delta(z)\delta(t) = G\delta(x)\delta(z)\delta(t). \tag{3.3}$$

The SH wave displacement satisfies a scalar wave equation; thus, the displacement can be found without using the SH potential. The Cagniard de-Hoop approach involves multiple domain trans-

formations that include both a spatial Fourier transform

$$f(k) = \int_{-\infty}^{\infty} f(t)e^{-i\boldsymbol{k}}dt, \qquad Forward, \tag{3.4}$$

$$f(x) = \frac{1}{2\pi}\int_{-\infty}^{\infty} f(k)e^{i\boldsymbol{k}}dk, \qquad Inverse, \tag{3.5}$$

and a Laplace transform

$$f(s) = \int_{0}^{\infty} f(t)e^{-st}dt, \qquad Forward, \tag{3.6}$$

$$f(t) = \frac{1}{2\pi i}\int_{c-i\infty}^{c+i\infty} f(s)e^{st}ds, \qquad Inverse. \tag{3.7}$$

Some useful properties of the transforms with respect to derivatives include

$$\begin{aligned} \mathscr{L}\left\{\partial_t^{(n)} f(t)\right\} &= (s)^n \mathscr{L}\left\{f(t)\right\}, \qquad Laplace, \\ \mathscr{F}\left\{\partial_x^{(n)} f(k)\right\} &= (ik_x)^n \mathscr{F}\left\{f(k)\right\}, \qquad Fourier, \end{aligned} \tag{3.8}$$

Also

$$\int_{-\infty}^{\infty} \delta(x)e^{-ik_x x}dx = 1, \qquad \int_{0}^{\infty} \delta(t)e^{-st}dt = 1. \tag{3.9}$$

In two dimensions, the waves displacement are a function of $x$ and $z$ (spatial), and time $t$ (temporal). For this analysis, the propagating wave is assumed to travel with increasing depth $z$ and the Fourier transforms will be carried out on the horizontal variable $x$. Applying the double transforms from equations 3.4 and 3.6 on equation 3.2, while utilizing equation 3.9, gives

$$\begin{aligned} \rho s^2 u_y(k_x, z, s) &= G\delta(z) + \mu\left(-k_x^2 + \frac{\partial^2}{\partial z^2}u_y(k_x, z, s)\right), \\ \frac{\partial^2}{\partial z^2}u_y(k_x, z, s) &= -\frac{G}{\rho\beta^2}\delta(z) + n^2 u_y(k_x, z, s), \end{aligned} \tag{3.10}$$

where $\beta^2 = \dfrac{\mu}{\rho}$ and $n^2 = k_x^2 + \dfrac{s^2}{\beta^2}$. In a heterogeneous media, the shear wave velocity is denoted as $\beta_1$ for the first medium that includes the source, and $\beta_2$ for the second medium. At depth $z \neq 0$,

equation 3.10 becomes

$$\frac{\partial^2 u_y}{\partial z^2} = n^2 u_y, \tag{3.11}$$

with general solutions of

$$u_y(k_x, z, s) = ae^{nz} + be^{-nz}, \tag{3.12}$$

where the choice of root for $n$ is $n > 0$. Requiring $u_y$ to be bounded as $z \to \pm\infty$ means that $a = 0$ for $z > 0$, and $b = 0$ for $z < 0$. Given the choice of root for n, then it follows

$$u_y(k_x, z, s) = be^{-nz}. \tag{3.13}$$

To find $u_y$, it remains to evaluate the constant b in equation 3.13. To do that, equation 3.10 is integrated once in terms of z which results in

$$\begin{aligned} \partial_z u_y|_{z=+z} - \partial_z u_y|_{z=-z} &= -\frac{G}{\rho\beta^2} H(z), \\ -nbe^{-nz} - nbe^{-nz} &= -\frac{G}{\rho\beta^2} H(z), \end{aligned} \tag{3.14}$$

and at $z = 0$

$$b = \frac{G}{2\rho n\beta^2}. \tag{3.15}$$

Substituting equation 3.15 back into equation 3.13 yields

$$u_y(k_x, z, s) = \frac{G}{2\rho n\beta^2} e^{-n|z|}. \tag{3.16}$$

The $H(z)$ function is the Heaviside step function that resulted from integrating $\delta(z)$. Applying the inverse Fourier transform from equation 3.5 on equation 3.16 results in

$$u_y(x, z, s) = \frac{G}{4\pi\rho\beta^2} \int_{-\infty}^{\infty} \frac{\exp(ik_x x - n|z|)}{n} dk_x, \tag{3.17}$$

with $Re(n) = Re(\sqrt{k_x^2 + s^2/\beta^2}) > 0$ which is generalized from $n > 0$. Letting the horizontal slowness $p = \dfrac{k_x}{is}$, $dk_x = isdp$, and defining the vertical slowness $\eta = \sqrt{1/\beta^2 - p^2}$ allows for rewriting the previous equation into

$$u_y(x, z, s) = \frac{G}{4\pi\rho\beta^2} \int_{-i\infty}^{i\infty} \frac{-ie^{-s(px-\eta|z|)}}{\eta} dp, \tag{3.18}$$

where $n = s\eta$ and $Re\ \eta > 0$ since $n > 0$. Rewriting the real and imaginary parts of $\dfrac{1}{\eta}e^{-s(px-\eta|z|)}$ as $E(p)$ and $O(p)$, while noting that $E$ is even and $O$ is odd for imaginary values of p, then

$$\int_{-i\infty}^{i\infty} -i(E + iO)dp = -2i \int_0^{i\infty} Edp = 2Im \left\{ \int_0^{i\infty} (E + iO)dp \right\}; \tag{3.19}$$

thus, equation 3.18 becomes

$$u_y(x, z, s) = \frac{G}{2\pi\rho\beta^2} Im \left\{ \int_0^{i\infty} \frac{e^{-s(px-\eta|z|)}}{\eta} dp \right\}, \tag{3.20}$$

where

$$t = px - \eta|z|. \tag{3.21}$$

Equation 3.20 represents the setup of the wave equation prior to Cagniard de-Hoop method's manipulation and equation 3.21 is the Cagniard path. The aim of Cagniard's manipulation is to replace equation 3.21 into 3.20 and find the representative transformation from $dp \rightarrow dt$. In order to complete this transformation, the solution for the horizontal slowness $p$ on the Cagniard's path must first be found, while avoiding branch points to ensure single-valued solutions. Regarding the SH waves case, it is possible to determine the modified Cagniard path; however, numerical methods are necessary when considering P-SV waves. Prior to finding p, it is instructive to find the travel time of the SH wave. To do that, $p = p_0$ is solved for by differentiating equation 3.21 in terms of

p:

$$
\begin{aligned}
0 &= x - \frac{p_0 z}{\eta}, \\
p_0 &= \frac{x\eta}{z}, \\
p_0 &= \frac{x\sqrt{\frac{1}{\beta^2} - p_0^2}}{z}, \\
p_0^2 &= \frac{x^2\left(\frac{1}{\beta^2} - p_0^2\right)}{z^2}, \\
\frac{x^2}{\beta^2} &= p_0^2 z^2 + p_0^2 x^2, \\
p_0 &= \frac{x}{\beta}\frac{1}{\sqrt{x^2+z^2}}.
\end{aligned}
\tag{3.22}
$$

$p_0$ is necessarily located in between $p = 0$ and the branch point $p = \dfrac{1}{\beta}$ (De Hoop, 1988). Let $t = T_B$ at $p = p_0$, then equation 3.21 becomes

$$
\begin{aligned}
T_B &= p_0 x + \sqrt{\frac{1}{\beta^2} - p_0^2} z, \\
T_B &= \frac{x^2}{\beta}\frac{1}{\sqrt{x^2+z^2}} + \sqrt{\frac{1}{\beta^2} - \frac{x^2}{\beta^2}\frac{1}{x^2+z^2}}, \\
T_B &= \frac{x^2}{\beta}\frac{1}{\sqrt{x^2+z^2}} + \frac{z^2}{\beta}\frac{1}{\sqrt{x^2+z^2}}, \\
T_B &= \frac{\sqrt{x^2+z^2}}{\beta} = \frac{R}{\beta},
\end{aligned}
\tag{3.23}
$$

where $R = \sqrt{x^2+z^2}$ is the source-receiver distance and $T_B$ is the arrival time of the body wave, SH, in accordance with Fermat's principle. Solving for $p$ on the Cagniard path from equation 3.21 involves solving the quartic equation starting from

$$
\begin{aligned}
t &= px + \eta|z|, \\
(t)^2 &= (px + \eta|z|)^2, \\
t^2 &= p^2x^2 + 2px\eta z + \eta^2 z^2,
\end{aligned}
$$

expanding further using the definition of $\eta$

$$t^2 = p^2x^2 + 2px\sqrt{\frac{1}{\beta^2} - p^2}z + \frac{z^2}{\beta^2} - z^2p^2,$$
$$t^2 = (x^2 - z^2)p^2 + 2xz\eta p + \frac{z^2}{\beta^2},$$

rearranging

$$\left(t^2 - (x^2 - z^2)p^2 - \frac{z^2}{\beta^2}\right)^2 = (2xz\eta p)^2,$$

expanding further results in

$$\underbrace{\left[(x^2 - z^2)^2 + 4x^2z^2\right]}_{A}p^4 - 2\underbrace{\left[(x^2 - z^2)t^2 - (x^2 - z^2)\frac{z^2}{\beta^2} + 2x^2\frac{z^2}{\beta^2}\right]}_{B}p^2 + \underbrace{\left(t^2 - \frac{z^2}{\beta^2}\right)^2}_{C} = 0,$$

$$Ap^4 - 2Bp^2 + C = 0.$$

Solving the previous quadratic equation for p results in

$$p = \begin{cases} \dfrac{xt - |z|\sqrt{\dfrac{R^2}{\beta^2} - t^2}}{R^2}, & t \leq \dfrac{R}{\beta}, \\ \dfrac{xt + i|z|\sqrt{t^2 - \dfrac{R^2}{\beta^2}}}{R^2}, & t \geq \dfrac{R}{\beta}. \end{cases} \tag{3.24}$$

The integral in equation 3.20 can instead be taken over the Cagniard path on which t increases from zero to infinity

$$u_y(x, z, s) = \frac{G}{2\pi\rho\beta^2} Im\left\{\int_C \frac{e^{-s(px - \eta|z|)}}{\eta} dp\right\}. \tag{3.25}$$

The derivative of $p$ with respect to $t$ on the Cagniard path is

$$\frac{dp}{dt} = \begin{cases} \dfrac{x}{R^2} + \dfrac{|z|t}{R^2\sqrt{\dfrac{R^2}{\beta^2} - t^2}}, & t \leq \dfrac{R}{\beta}, \\ \dfrac{x}{R^2} + \dfrac{i|z|t}{R^2\sqrt{t^2 - \dfrac{R^2}{\beta^2}}}, & t \geq \dfrac{R}{\beta}. \end{cases} \tag{3.26}$$

To complete Cagniard de-Hoop's transformation, the vertical slowness $\eta$ must be calculated on the Cagniard path as well. Substituting equation 3.24 for $t \geq \dfrac{R}{\beta}$ into equation 3.21 yields

$$t = px + \eta|z|,$$

$$\eta = \frac{t - px}{|z|} = \frac{t}{|z|} - \frac{x^2 t - i|z|x\sqrt{t^2 - \dfrac{R^2}{\beta^2}}}{zR^2},$$

$$\eta = \frac{|z|}{R^2}t - \frac{ix\sqrt{t^2 - \dfrac{R^2}{\beta^2}}}{R^2}, \tag{3.27}$$

and for $t \leq \dfrac{R}{\beta}$

$$\eta = \frac{|z|}{R^2}t + \frac{x\sqrt{t^2 - \dfrac{R^2}{\beta^2}}}{R^2}, \tag{3.28}$$

Using $\eta$ defined from equations 3.27, 3.28 and substituting it back into equation 3.26 yields

$$\frac{dp}{dt} = \begin{cases} \dfrac{\eta}{\sqrt{\dfrac{R^2}{\beta^2} - t^2}}, & 0 < t < \dfrac{R}{\beta}, \\ \dfrac{i\eta}{\sqrt{t^2 - \dfrac{R^2}{\beta^2}}}, & \dfrac{R}{\beta} < t. \end{cases} \tag{3.29}$$

It follows then that equation 3.25, after substituting in equation 3.29, becomes

$$u_y(x,z,s) = Im\left\{\int_{t=\frac{R}{\beta}}^{t=\infty} \underbrace{\frac{iG}{2\pi\rho\beta^2\sqrt{t^2-\frac{R^2}{\beta^2}}}}_{u_y(x,z,t)} e^{-st}dt\right\} + Im\left\{\int_{t=0}^{t=\frac{R}{\beta}} \underbrace{\frac{G}{2\pi\rho\beta^2\sqrt{\frac{R^2}{\beta^2}-t^2}}}_{u_y(x,z,t)} e^{-st}dt\right\} \tag{3.30}$$

Arriving at equation 3.30 completes Cagniard de-Hoop's manipulation. The integrals in that equation depicts forward Laplace transform where the integrand is the displacement in time domain that is initially sought. Recognizing that, the left term of the right handside from equation 3.30

becomes

$$
\begin{aligned}
u_y(x,z,s) &= Im\left\{\int_{t=\frac{R}{\beta}}^{t=\infty} \underbrace{\frac{iG}{2\pi\rho\beta^2\sqrt{t^2-\frac{R^2}{\beta^2}}}}_{u_y(x,z,t)} e^{-st}dt\right\},\\
u_y(x,z,s) &= Im\left\{\int_{t=0}^{t=\infty} \underbrace{\frac{iGH(t-\frac{R}{\beta})}{2\pi\rho\beta^2\sqrt{t^2-\frac{R^2}{\beta^2}}}}_{u_y(x,z,t)} e^{-st}dt\right\},\\
u_y(x,z,t) &= Im\left\{\frac{iG}{2\pi\rho\beta^2}\frac{H(t-\frac{R}{\beta^2})}{\sqrt{t^2-\frac{R^2}{\beta^2}}}\right\},\\
u_y(x,z,t) &= Re\left\{\frac{G}{2\pi\rho\beta^2}\frac{H(t-\frac{R}{\beta^2})}{\sqrt{t^2-\frac{R^2}{\beta^2}}}\right\} = \frac{G}{2\pi\rho\beta^2}\frac{H(t-\frac{R}{\beta^2})}{\sqrt{t^2-\frac{R^2}{\beta^2}}},
\end{aligned}
\tag{3.31}
$$

where the following property was used from Imaginary to Real evaluation (Båth, 1968)

$$Re[i(x+iy)] = Re(ix-y) = -y = -Im(x+iy). \tag{3.32}$$

The SH displacement from equation 3.31 represents the complete displacement in a homogeneous whole-space medium where the first wave arrival occurs at $t = T_B = \frac{R}{\beta}$ which means it is the direct wave arrival. In such medium, there will be no contributions prior to $T_B$ because the horizontal slowness, $p(t)$, is real-valued on the Cagniard path and this would render the integral of the second term in equation 3.30 to be equal to zero. However, if the medium is heterogeneous; i.e.,

a half-space, then a reflected wave can exist. Further, if the second medium is characterized by a higher velocity value than the first then there can exist a condition for the generation of head-waves which eventually precedes the arrival time of both direct and reflected waves. In this case, there will be an imaginary valued contribution of the Cagniard path since the horizontal slowness for the refracted waves is

$$p = \frac{sin90^\circ}{\beta_2} = \frac{1}{\beta_2}, \tag{3.33}$$

which leads to an imaginary valued $\eta$ that contributes to a nonzero imaginary part on the Cagniard path as shown in figure 3.2. There are two contributions in a heterogeneous medium on the Cagniard path. The first contribution is due to the reflected wave arrival which coincides with $p = \frac{sinj_s}{\beta_1}$ corresponding to $t = T_R = \frac{\sqrt{x^2 + (z+h)^2}}{\beta_1} = \frac{R_0}{\beta_1}$; where, $z_0$ is the distance from the interface to the receiver. The second contribution is due to the refracted wave which coincides with $p = \frac{1}{\beta_2}$, where the corresponding refracted wave time arrival is

$$t = T_H = \frac{x}{\beta_2} + |z+h|\sqrt{\frac{1}{\beta_1^2} - \frac{1}{\beta_2^2}}, \tag{3.34}$$

which is found by substituting equation 3.33 into equation 3.21. To find the total displacement in heterogeneous medium, boundary conditions for SH waves in 2D must be satisfied. This includes continuity of displacement, $u_y$, and traction, $\tau_{yz}$. The reflection coefficient that results from satisfying the boundary conditions across depth $z = 0$ for a down-going SH wave is

$$\grave{S}\acute{S} = \frac{\mu_1\eta_1 - \mu_2\eta_2}{\mu_1\eta_2 + \mu_2\eta_2}, \tag{3.35}$$

and the transmission coefficient

$$\grave{S}\grave{S} = \frac{2\mu_1\eta_1}{\mu_1\eta_1 + \mu_2\eta_2}, \tag{3.36}$$

where $\mu$ and $\eta$ subscripts correspond to either $\beta_1$ or $\beta_2$ representing the different mediums. Using the reflection coefficient from equation 3.35, $R_0$ instead of $R$ in equation 3.29, depicting a heterogeneous medium, and substituting the results into equation 3.25 leads to the reflected SH wave

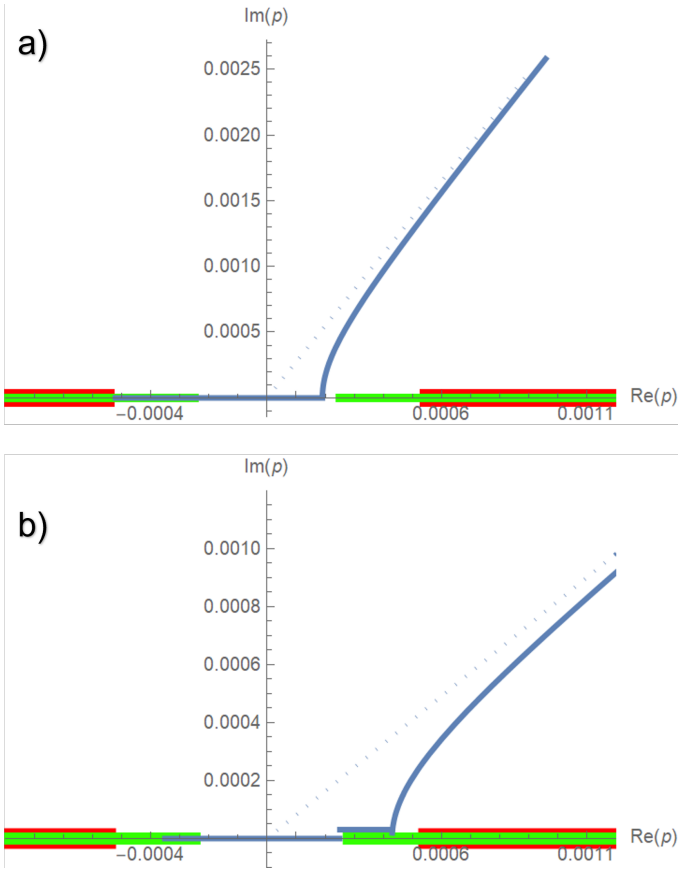


Figure 3.2: The Cagniard path on p=p(t) for a heterogeneous medium. (a) is the Cagniard path pre-critical angle where the point of departure from the real p-axis lies to the left of the branch cuts representing reflected waves only . (b) is the Cagniard path post the critical angle where the initial point of departure lies between $1/\beta_2$ and $1/\beta_1$ which represents head-waves contribution. The red line is the branch cut due to $\beta_1$ which starts at $\pm 1/\beta_1$. The green line is the branch cut due to $\beta_2$ which starts at $\pm 1/\beta_2$. The dashed line in (a) and (b) represent the angle of incidence, $j_s$, for the whole-space and half-space medium, respectively

displacement as follows

$$u_y^{refl}(x,z,t) = \frac{G}{2\pi\rho_1\beta_1^2} Re\left\{\grave{S}\acute{S}\right\} \frac{H(t-R_0/\beta_1)}{\sqrt{t^2-R_0^2/\beta_1^2}} + \frac{G}{2\pi\rho_1\beta_1^2} Im\left\{\grave{S}\acute{S}\right\} \frac{H(t-T_H)-H(t-R_0/\beta_1)}{\sqrt{\frac{R_0^2}{\beta_1^2}-t^2}}, \tag{3.37}$$

where the left term is the contribution due to the reflected wave and the rightmost term is the contribution due to the refracted wave. Substituting the transmission coefficient from equation 3.36; instead, would result in the transmitted SH wave displacement. The total displacement at a

given receiver then combines the displacement due to the direct wave from equation 3.31 and the refleced, refracted waves due to equation 3.37. The total displacement then becomes

$$u_y(x,z,t) = \frac{G}{2\pi\rho\beta^2}\frac{H(t-R/\beta^2)}{\sqrt{t^2-\dfrac{R^2}{\beta^2}}} + \frac{G}{2\pi\rho_1\beta_1^2}Re\left\{\grave{S}\acute{S}\right\}\frac{H(t-R_0/\beta_1)}{\sqrt{t^2-R_0^2/\beta_1^2}} + \frac{G}{2\pi\rho_1\beta_1^2}Im\left\{\grave{S}\acute{S}\right\}\frac{H(t-T_H)-H(t-R_0/\beta_1)}{\sqrt{\dfrac{R_0^2}{\beta_1^2}-t^2}}. \tag{3.38}$$

Equation 3.38 represents the analytical SH wave solution in a heterogoneous medium using the body force model.

### 3.1.2 P-SV Wave Solution using the Cagniard de-Hoop Method

In this section, P-SV motions with displacement only in the x and z directions will be considered due to the two-dimensional geometry of the line source problem. Further, the analytical geometry will include an elastic half-space using the conceptual body force model along with Cagniard de-Hoop's manipulation and time domain solution. Starting from the P and SV scalar potentials from equations 2.46 and 2.47 , respectively, the corresponding displacement in 2D becomes

$$u_x = \frac{\partial\phi}{\partial x} - \frac{\partial\psi}{\partial z}, u_y = 0, u_z = \frac{\partial\phi}{\partial z} + \frac{\partial\psi}{\partial x}. \tag{3.39}$$

In this geometry, the P-SV waves are coupled in x and z and there is no motion in y direction which is characterized only by SH waves. The P-SV solution development is similar to SH but involves a slightly different approach to accommodate the vector displacement and different cases of reflection coefficients. The approach for the P-SV case involves starting from the scalar potential, then defining the line source and invoking the Cagniard de-Hoop method. Prior to proceeding to the Cagniard's manipulation back to time domain, the conversion from scalar potential to displacements will be carried out in Laplace/Fourier domain because partial derivatives become a simple multiplication process. After retrieving the displacement motions, the Cagniard method will transform the result back to time-space domain where the motion will be clearly identified for any given

ray (SS, SP, PS, PP). The line source for the scalar potentials from equations 2.46 and 2.47 is

$$\begin{aligned}\Phi &= \frac{(-\nu)A}{h^2}S(t)\delta(x)\delta(z) = G_P(t)\delta(x)\delta(z),\\ \Psi &= \frac{A}{h^2}S(t)\delta(x)\delta(z) = G_S(t)\delta(x)\delta(z).\end{aligned} \tag{3.40}$$

The source term for the P and SV waves are defined utilizing the effective source in the conceptual body force model. Substituting equation 3.40 into equations 2.46 and 2.47; respectively, and transforming the potentials from space-time to Fourier-Laplace domain in the process leads to

$$\begin{aligned}\phi^{inc}(k_x, z, s) &= \frac{G_P(s)}{2\rho\alpha^2 s\xi}e^{-s\xi|z-h|},\\ \psi^{inc}(k_x, z, s) &= \frac{G_S(s)}{2\rho\beta^2 s\eta}e^{-s\eta|z-h|},\end{aligned} \tag{3.41}$$

where $\phi^{inc}$ and $\psi^{inc}$ are the incoming displacement potentials in a homogeneous medium representing waves directly from the source to the receiver point. Further, $\xi$ is the P wave vertical slowness defined as $\xi = \sqrt{\alpha^{-2} - p^2}$, $\eta$ is the S wave vertical slowness defined as $\eta = \sqrt{\beta^{-2} - p^2}$, and the chosen roots are $Re\ \xi > 0$ and $Re\ \eta > 0$; respectively, to satisfy radiation conditions. Equation 3.41 can be expanded for a heterogeneous medium by satisfying boundary conditions. For a solid-solid half-space, the total potentials become

$$\begin{aligned}\phi(k_x, z, s) =& \frac{G_P(s)}{2\rho\alpha^2 s\xi}\left\{exp(-s\xi|z-h|) + \grave{P}\acute{P}exp(-s\xi|z+h|)\right\}\\ &+ \frac{G_S(s)}{2\rho\beta^2 s\eta}\frac{\alpha}{\beta}\grave{S}\acute{P}exp\left[-s(\xi z + \eta h)\right],\\ \psi(k_x, z, s) =& \frac{G_S(s)}{2\rho\beta^2 s\eta}\left\{exp(-s\eta|z-h|) + \grave{S}\acute{S}exp(-s\eta|z+h|)\right\}\\ &+ \frac{G_P(s)}{2\rho\alpha^2 s\xi}\frac{\beta}{\alpha}\grave{P}\acute{S}exp\left[-s(\eta z + \xi h)\right],\end{aligned} \tag{3.42}$$

where the reflection coefficients are

$$\begin{aligned}
\grave{P}\acute{P} &= \left[(b\xi_1 - c\xi_2)F - (a + d\xi_1\eta_2)Hp^2\right]/D, \\
\grave{S}\acute{P} &= -2\eta_1\left(ab + cd\xi_2\eta_2\right)p\beta_1/(\alpha_1 D), \\
\grave{S}\acute{S} &= -\left[(b\eta_1 - c\eta_2)E - (a + d\xi_2\eta_1)Jp^2\right]/D, \\
\grave{P}\acute{S} &= -2\xi_1\left(ab + cd\xi_2\eta_2\right)p\alpha_1/(\beta_1 D),
\end{aligned} \tag{3.43}$$

and

$$\begin{aligned}
a &= \rho_2(1 - 2\beta_2^2p^2) - \rho_1(1 - 2\beta_1^2p^2), & b &= \rho_2(1 - 2\beta_2^2p^2) + 2\rho_1\beta_1^2p^2, \\
c &= \rho_1(1 - 2\beta_1^2p^2) + 2\rho_2\beta_2^2p^2, & d &= 2(\rho_2\beta_2^2 - \rho_1\beta_1^2),
\end{aligned}$$

$$\begin{aligned}
E &= b\xi_1 + c\xi_2, & F &= b\eta_1 + c\eta_2, \\
J &= a - d\xi_1\eta_2, & H &= a - d\xi_2\eta_1, \\
D &= EF + GHp^2.
\end{aligned}$$

In the special case of fluid-solid interface where $\beta_1 = 0$, the conversion coefficients from equation 3.1.2 become

$$\begin{aligned}
\grave{P}\acute{P} &= \left[-\rho_1\xi_2/(4\rho_2\xi_1\beta_2^4) + \Delta_R\right]/\Delta_{SCH}, \\
\grave{P}\grave{P} &= \left[2(1 - 2p^2\beta_2^2)\rho_1(\alpha_1/\alpha_2)\xi_1\right]/\Delta_{SCH}, \\
\grave{P}\grave{S} &= \left[4 * \rho_1\alpha_1\beta_2 p\xi_1\xi_2\right]/\Delta_{SCH},
\end{aligned} \tag{3.44}$$

where

$$\Delta_R = (p^2 - 1/2\beta_2^2)^2 + p^2\xi_2\eta_2 \tag{3.45}$$

is the Rayleigh wave function and

$$\Delta_{SCH} = \rho_1\xi_2/(4\rho_2\xi_1\beta_2^4) + \Delta_R \tag{3.46}$$

is the Scholte wave function. The Rayleigh wave function is associated with surface waves that propagate along a traction-free boundary of a solid. The Scholte wave function is associated with surface waves that propagate along a fluid-solid interface. Reflection and transmission coefficients for P-SV waves differ based on the media (fluid/solid) and the upgoing/downgoing ray type (Aki and Richards, 2002, pp. 135-143).

In the P-SV wave displacement solution, it is convenient to proceed with the inversion process with the displacement components instead of potentials since spatial operators are a simple multiplicative term. Therefore, equation 3.42 becomes

$$\begin{aligned}\begin{pmatrix} u_x(k_x,z,s) \\ u_z(k_x,z,s) \end{pmatrix} =& \frac{G_P(s)}{2\rho\alpha^2\xi}\left[\begin{pmatrix} -p \\ -\xi \end{pmatrix} exp[-s\xi(z-h)] + \grave{P}\acute{P}\begin{pmatrix} -p \\ -\xi \end{pmatrix} exp[-s\xi(z+h)]\right] \\ &+ \frac{G_S(s)}{2\rho\beta^2\eta}\frac{\alpha}{\beta}\grave{S}\acute{P}\begin{pmatrix} -p \\ -\xi \end{pmatrix} exp[-s(\xi z+\eta h)] \\ &+ \frac{G_P(s)}{2\rho\alpha^2\xi}\frac{\beta}{\alpha}\grave{P}\acute{S}\begin{pmatrix} \eta \\ -p \end{pmatrix} exp[-s(\eta z+\xi h)] \\ &\frac{G_S(s)}{2\rho\beta^2\eta}\left[\begin{pmatrix} -\eta \\ -p \end{pmatrix} exp[-s\eta(z-h)] + \grave{S}\acute{S}\begin{pmatrix} \eta \\ -p \end{pmatrix} exp[-s\eta(z+h)]\right].\end{aligned} \tag{3.47}$$

From equation 3.47, the analytical solution using the Cagniard method can be found for the P, S, PP, and SS rays following a similar development as demonstrated in detail for the SH wave in the previous section. This is mainly due to similar Cagniard Path that can be solved analytically. However, this is not possible for the PS and SP ray paths due to them having different vertical slowness for the up-going and down-going waves. For the converted waves, there are two main distinctions that arise compared to the others; namely, the travel time calculation and the Cagniard Path solution. To find the travel time, the PS waves must satisfy the following equations

$$x = h\tan\theta_P + z\tan\theta_S, \tag{3.48}$$

$$\frac{\sin\theta_S}{\sin\theta_P} = \frac{\beta}{\alpha}, \tag{3.49}$$

where $\theta_P$ is the angle of incidence for the P waves and $\theta_S$ is the angle of reflection for the S waves. Equations 3.48 and 3.49 can be solved simultaneously to find the angles, which are used to find the minimum travel time of the PS waves

$$t_{PS} = \frac{h}{\alpha\cos\theta_P} + \frac{z}{\beta\cos\theta_S}. \tag{3.50}$$

To perform the inversion for the PS waves, the p solution along the Cagniard path must be found. The Cagniard path for the PS wave is defined as

$$t = px + \eta z + \xi h. \tag{3.51}$$

Solving equation 3.51 leads to the quartic equation in $p$ with

$$Ap^4 - 4iBp^3 - 2Cp^2 + 4iDp + E = 0, \tag{3.52}$$

where all the coefficients are real and defined as

$$\begin{aligned}
A &= \left[(H+Z)^2 + X^2\right]\left[(H-Z)^2 + X^2\right] > 0 \\
B &= tX(H^2 + X^2 + Z^2) > 0 \\
C &= t^2(H^2 + 3X^2 + Z^2) - \left[X^2(H^2a^2 + Z^2) + (H^2 - Z^2)(H^2a^2 - Z^2)\right], \\
D &= tX\left[t^2 - (H^2a^2 + Z^2)\right], \\
E &= (t^2 - (Ha + Z)^2)(t^2 - (Ha - Z)^2),
\end{aligned} \tag{3.53}$$

where

$$\begin{aligned}
H = \frac{h}{R_0}, \quad Z = \frac{z}{R_0}, \quad X = \frac{x}{R_0}, \\
a = \frac{\beta}{\alpha}, \quad R_0 = \sqrt{x^2 + (z+h)^2}.
\end{aligned}$$

The quartic equation admits four roots which can appear in alternative forms (Sanchez-Sesma et. al, 2012). Generally, two roots of equation 3.53 have positive real part, which are $p_3$ and $p_4$, and the chosen solution is the root with the smallest positive imaginary part (Shan and Ling, 2016). Therefore, after numerically solving for $p$ in equation 3.52, the chosen p root is

$$p = \begin{cases} p_3, & \text{if } |Im(p_3)| < |Im(p_4)|, \\ p_4, & \text{if } |Im(p_3)| > |Im(p_4)|, \end{cases} \tag{3.54}$$

and the $dp/dt$ for the PS ray is obtained by the derivative of equation 3.51 as

$$\frac{dp}{dt} = \frac{1}{x - \dfrac{pz}{\eta} - \dfrac{ph}{\xi}}. \tag{3.55}$$

With this, the general total analytical displacement solutions for P-SV waves are

$$\begin{aligned} u_x =& \frac{G_P}{2\pi\rho\alpha^2}\left\{ Re(p)\frac{H(t-R/\alpha)}{\sqrt{t^2-R^2/\alpha^2}} + Im\left[\frac{p}{\xi}PP\frac{dp}{dt}\right] + Im\left[\frac{\eta}{\xi}\frac{\beta}{\alpha}PS\frac{dp}{dt}\right]\right\} + \\ & \frac{G_S}{2\pi\rho\beta^2}\left\{ Re(\eta)\frac{H(t-R/\beta)}{\sqrt{t^2-R^2/\beta^2}} + Im\left[SS\frac{dp}{dt}\right] + Im\left[\frac{p}{\eta}\frac{\alpha}{\beta}SP\frac{dp}{dt}\right]\right\}, \end{aligned} \tag{3.56}$$

$$\begin{aligned} u_z =& \frac{G_P}{2\pi\rho\alpha^2}\left\{ Re(\xi)\frac{H(t-R/\alpha)}{\sqrt{t^2-R^2/\alpha^2}} + Im\left[PP\frac{dp}{dt}\right] + Im\left[\frac{p}{\xi}\frac{\beta}{\alpha}PS\frac{dp}{dt}\right]\right\} + \\ & \frac{G_S}{2\pi\rho\beta^2}\left\{ Re(p)\frac{H(t-R/\beta)}{\sqrt{t^2-R^2/\beta^2}} + Im\left[\frac{p}{\eta}SS\frac{dp}{dt}\right] + Im\left[\frac{\xi}{\eta}\frac{\alpha}{\beta}SP\frac{dp}{dt}\right]\right\} \end{aligned}, \tag{3.57}$$

where $p$ and $\dfrac{dp}{dt}$ for reflected waves, PP and SS, are found similar to equations 3.24 and 3.26; respectively, while substituting the appropriate wave velocity and vertical slowness corresponding to P and S waves. As for PS and SP, the $p$ and $\dfrac{dp}{dt}$ are found from equations 3.54 and 3.55, respectively.

## 3.2 Analytical Analysis of Seismic Wave Propagation

In this section, analysis of the analytical solution of the wave propagation across the the sea-bottom boundary will be carried out utilizing the effective source from the conceptual body force model. Each propagating wave type will be analyzed accordingly and the impact of the Poisson ratio, $\nu$, and distance of the airgun source, $h$, will be demonstrated. This will be done through three model cases ranging from soft unconsolidated mud to hard coral reefs.

### 3.2.1 SH Waves Analysis

With the Cagniard de-Hoop method, the exact analytical solution for the SH waves can be found. Using the configuration from figure 3.1, the source is located at depth $z = 0$ and the receiver is across the horizontal boundary at similar depth which is similar to the configuration of the shallow marine environment of the Arabian Gulf. Using the analytical solution from equation 3.38, the SH wave displacement solution for different values of $\nu$ and $h$ is given in figures 3.3 and 3.4 below. Figure 3.4 depicts the analytical displacement solution for SH waves using different models; where each model represents different Poisson ratio, $\nu$, of the sea-bottom ranging from soft to hard. The variation in sea-bottom hardness simulates a soft unconsolidated mud for the soft model to a hard coral reef with $30$ percent porosity for the hard model, which is typical in the Arabian Gulf. Each displacement solution is calculated at a single receiver situated $500\ m$ away from the effective source at the sea-bottom. In figure 3.3, the distance from the airgun source to the effective source at the sea-bottom is $h = 10\ m$. The SH wave displacement solution is calculated for three different models. The first (top) model is characterized by a slow shear wave velocity for the sea-bottom of $\beta = 250\ m/s$, density of $\rho = 1200\ kg/m^3$, and P wave velocity of $\alpha = 1650\ m/s$. These properties result in a Poisson ration for the sea-bottom of $\nu = 0.488$ which represents an unconsolidated soft solid. The peak displacement amplitude for this model is $u_y = 1.1 \times 10^{-3}\ m$. The second model (center) is characterized by an average shear wave velocity for the sea-bottom of $\beta = 1540\ m/s$, density of $\rho = 2100\ kg/m^3$, and P wave velocity of $\alpha = 3400\ m/s$. These properties result in a Poisson ration for the sea-bottom of

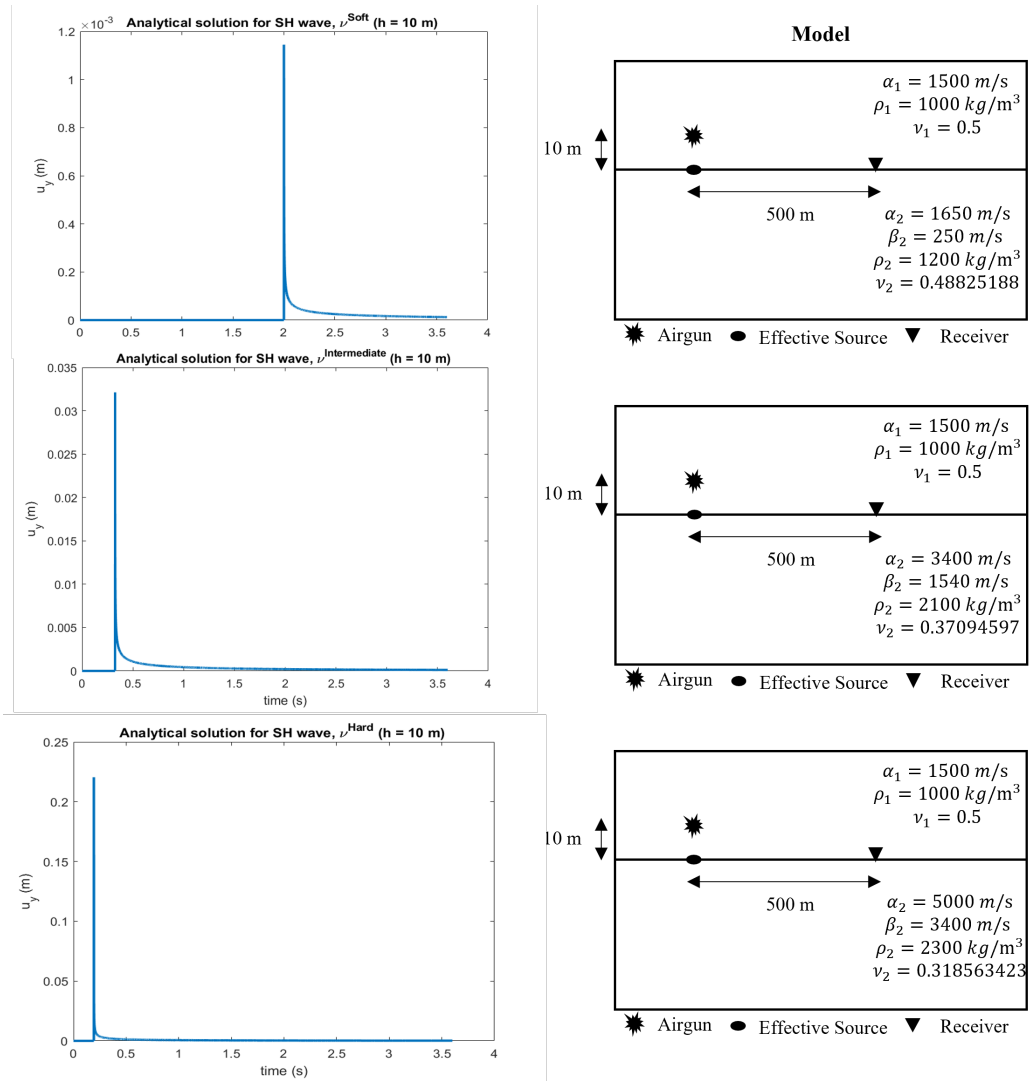


Figure 3.3: Analytical displacement solutions for SH waves given a distance $h = 10\ m$ from the airgun source to the effective source at the sea-bottom. Each displacement solution is calculated a distance $x = 500\ m$ from the source using different elastic parameters representing soft, intermediate, and hard solid layers.

$\nu = 0.371$ which represents an intermediate consolidated solid. The peak displacement amplitude for this model is $u_y = 0.033\ m$. The third model (bottom) is characterized by a fast shear wave velocity for the sea-bottom of $\beta = 2580\ m/s$, density of $\rho = 2300\ kg/m^3$, and P wave velocity of $\alpha = 5000\ m/s$. These properties result in a Poisson ratio for the sea-bottom of $\nu = 0.319$ which represents a hard consolidated solid. The peak displacement amplitude for this model is $u_y = 0.22\ m$. The configuration of the models in figure 3.3 represents the typical configuration

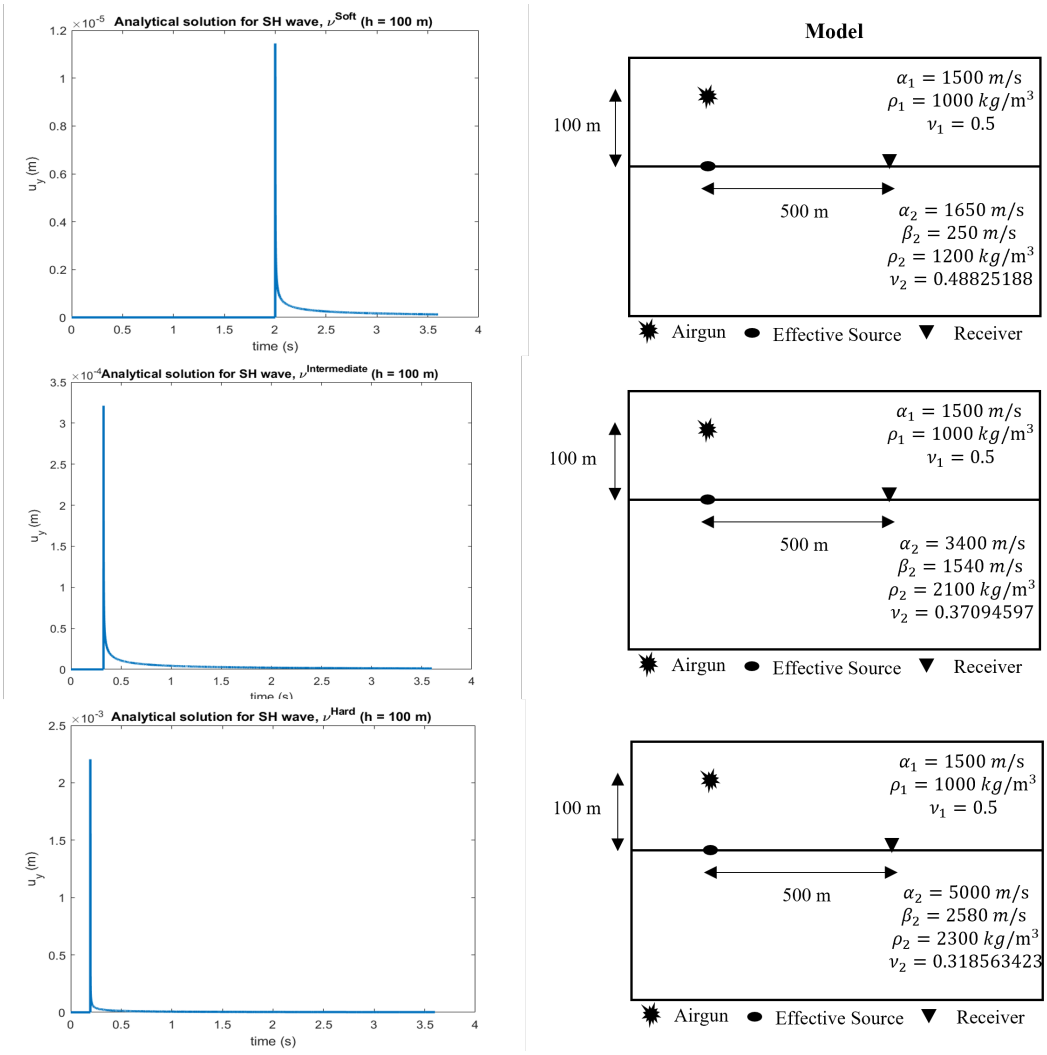


Figure 3.4: Analytical displacement solutions for SH waves given a distance $h = 100\ m$ from the airgun source to the effective source at the sea-bottom. Each displacement solution is calculated a distance $x = 500\ m$ from the source using different elastic parameters representing soft, intermediate, and hard solid layers.

that of the shallow marine environment in the Arabian Gulf. Given the airgun distance of $h = 10$ $m$, the impact on the displacement amplitudes is highlighted by the rigidity of the sea-bottom. As observed, the displacement amplitude of the hard solid is more than five times the intermediate solid, and almost $100$ times the value of the soft unconsolidated solid. This indicates that even with the shallow water environment, the hardness of the sea-bottom has a drastic effect on the strength of the SH wave generated at the sea-bottom from the effective source. In figure 3.4, the displacement solution is calculated using three different models given a distance from the airgun to the effective source at the sea-bottom of $h = 100\ m$. These models are identical to the models of figure 3.4 except for the airgun distance. The configuration from figure 3.4 represents that of the deep-sea environment typical of the North Sea. For the soft solid model, the displacement amplitude solution is $u_y = 1.1 \times 10^{-5}\ m$. For the intermediate solid model, the displacement amplitude solution is $u_y = 3.3 \times 10^{-4}\ m$. For the hard solid model, the displacement amplitude solution is $u_y = 2.2 \times 10^{-3}\ m$. The relative amplitude difference between the models is similar to the variation depicted from figure 3.3 which indicates that the impact of the hard sea-bottom on the displacement amplitude values. However, the amplitude values in the deep water are $100$ times lower than the shallow water displacement amplitude values for each model type. In fact, the displacement amplitude value for the hard consolidated model in figure 3.4 is approximately twice as strong the soft unconsolidated solid in figure 3.3. Moreover, the displacement amplitude values of the hard consolidated solid in figure 3.3 is approximately more than a $1000$ times stronger than the soft unconsolidated solid in figure 3.4. This indicates that although the hardness of the sea-bottom affects the strength of the SH waves generated, the distance of the airgun to the sea-bottom remains a great influence on the generated SH waves on the sea-bottom. This is shown by the fact that a shallow source with unconsolidated solid generates SH waves almost as strong as the far source with hard consolidated solid. Furthermore, a combination of both a shallow airgun depth and a hard sea-bottom depth is responsible for generating strong SH shear waves at the sea-bottom in the shallow marine environment in the Arabian Gulf. This analysis validates the previous work observations and claims that the energy conversion of shear waves at the sea-bottom in the shallow

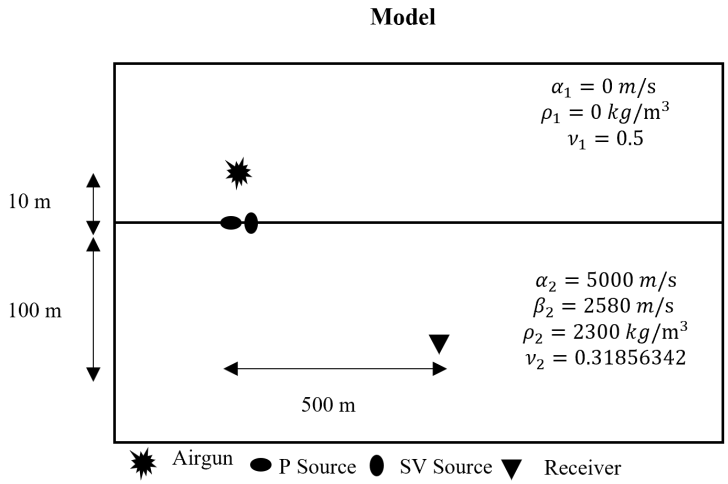


Figure 3.5: Physical model used for the P and SV waves analysis.

marine environment is around $1000$ times stronger than the energy conversion of shear waves for the deep water environment (Sun and Bertuessen, 2009).

### 3.2.2 P-SV Waves Analysis

With the Cagniard-de Hoop method, the exact analytical solution for the P and SV waves utilizing the effective P and SV source is calculated for the hard sea-bottom case with the shallow water to simulate the shallow marine environment of the Arabian Gulf. For the hard sea-bottom, the P and S velocities are very high that the difference between the velocities of the hard sea-bottom and the water layer on top can be approximated and assumed to be the difference similar to the difference between an elastic bottom and the free surface. Further, the proximity of the source makes this configuration resemble a Lamb's problem. Therefore, the model configuration used for the P-SV waves analysis is shown in figure 3.5.

Using the configuration from figure 3.5, the pressure source is located at depth $h = 10$, the effective P and SV source at depth $z = 0.01\ m$, and the receiver is a distance $x = 500\ meters$ at a depth of $z_0 = 100\ m$ . The physical model depicts a free surface on top of an elastic half-space with a source directly acting on the elastic half-space which is similar to Lamb's problem. Using equation 3.56, The P and SV waves analytical solution for the horizontal displacement will be

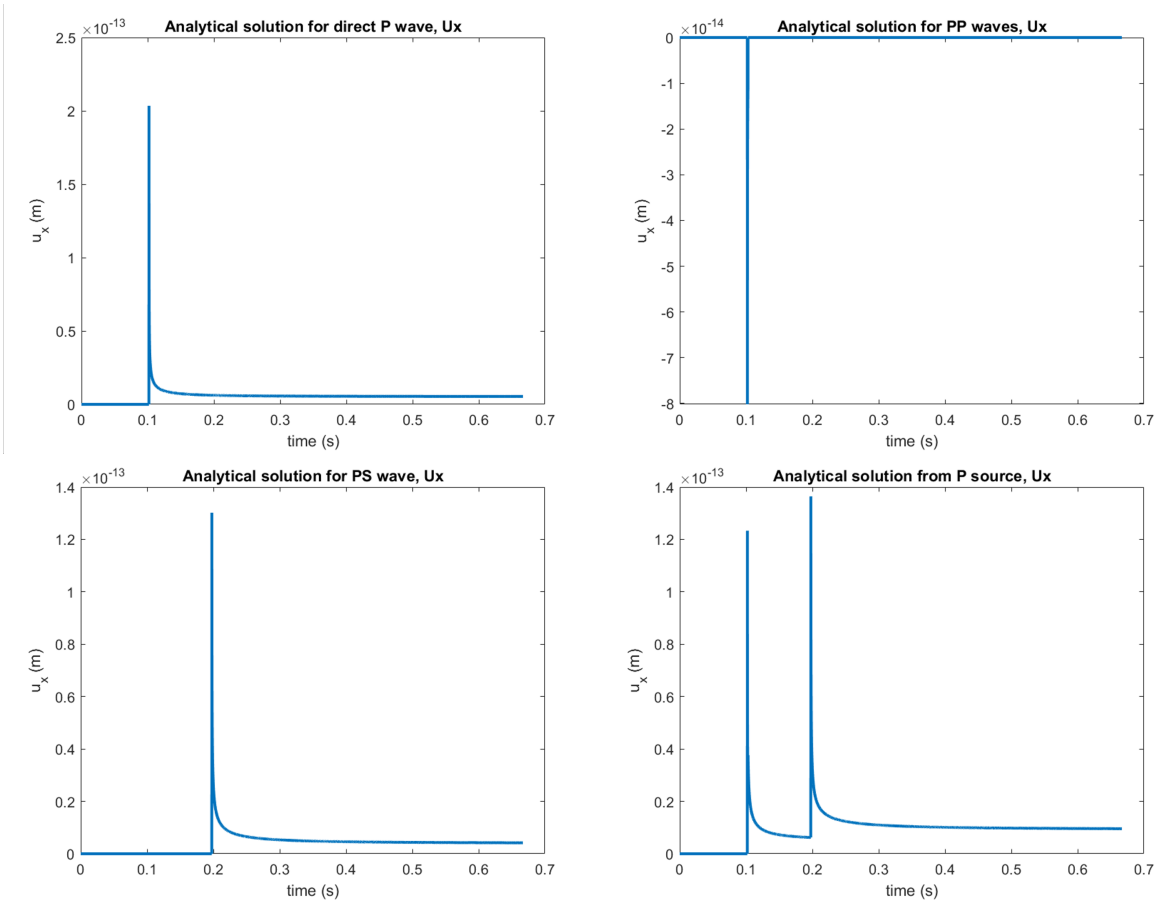


Figure 3.6: Horizontal displacements analytical solutions assuming a Lamb's problem utilizing the P source at depth $z = 0.01\ m$. Each displacement solution is calculated at a distance $x = 500\ m$ with a depth of $z_0 = 100\ m$.

calculated from the P and SV source assuming a Lamb's problem parameter by assuming $h = 0$, then utilizing the conceptual body force parameters by placing the source at $h = 10\ m$ representing the shallow source depth. Utilizing the model from figure 3.5, the analytical solution from the P effective source is solved assuming a Lamb's problem as shown in figure 3.6. The previous figure shows the horizontal displacement solutions from P source calculated using equation 3.57. Since the calculations were done assuming a typical Lamb's problem with the source placed at depth $z = 0.01\ m$ instead of the actual effective source, then the corresponding conceptual model factors of source depth $h$ and Poisson ratio $\nu$ were not considered. From the P source, three distinctive events are observed; namely, the direct P, reflected PP, and converted PS waves. The direct P wave

arrives at $t = 0.1\ s$ and has an amplitude of $u_x = 2.1 \times 10^{-13}\ m$. The reflected PP arrives at $t = 0.1\ s$ and has an amplitude of $u_x = -8.0 \times 10^{-14}\ m$. The arrival times of both direct P and reflected PP coincide due to the placement of the source at the interface. The converted PS arrives at $t = 0.2\ s$ and has an amplitude of $u_x = 1.3 \times 10^{-13}\ m$. The total analytical solution at the receiver is the summation of all these events; however, the reflected PP arrival is not observed since it coincides with the direct P wave arrival and causes a lower amplitude value of $u_x = 1.2 \times 10^{-13}$ $m$ when combined together. The analytical solutions for P and SV waves are more complicated compared with SH wave solution. Therefore, the analytical solution from a P source is compared with analytical solution found in literature to verify the results computed as shown in figure 3.7. From figure 3.7, the horizontal displacement solutions were calculated for a P source placed away from the interface and at the same level with the receiver. In this configuration, the first arrival is the P, followed by the PP, and finally the PS wave event. In this configuration, all the wave arrivals are clearly identifiable and similar parameters were used to the literature. By comparing the results, the relative amplitude of the analytical solution used in this dissertation is similar to the literature analytical solution. Proceeding with Lamb's problem configuration, the analytical horizontal displacement solutions is calculated for the SV source as shown in figure 3.8. Figure 3.8 shows the horizontal displacement solutions from SV source calculated using equation 3.57. Since the calculations were done assuming a typical Lamb's problem with the source placed at depth $z = 0.01\ m$ instead of the actual effective source, where the corresponding conceptual model factors of the source depth $h$ and Poisson ratio $\nu$ were not considered. From the SV source, three distinctive events are observed; namely, the direct S, reflected SS, and converted SP waves. The direct S wave arrives at $t = 0.2\ s$ and has an amplitude of $u_x = 1.25 \times 10^{-13}\ m$. The reflected SS arrives at $t = 0.2\ s$ and has an amplitude of $u_x = 5.0 \times 10^{-14}\ m$. The arrival times of both direct S and reflected SS coincide due to the placement of the source at the interface. The converted SP arrives at $t = 0.1\ s$ and has an amplitude of $u_x = 1.4 \times 10^{-13}\ m$. The total analytical solution at the receiver is the summation of all these events; however, the reflected SS arrival is not observed since it coincides with the direct S wave arrival which is $10$ times stronger in amplitude than the

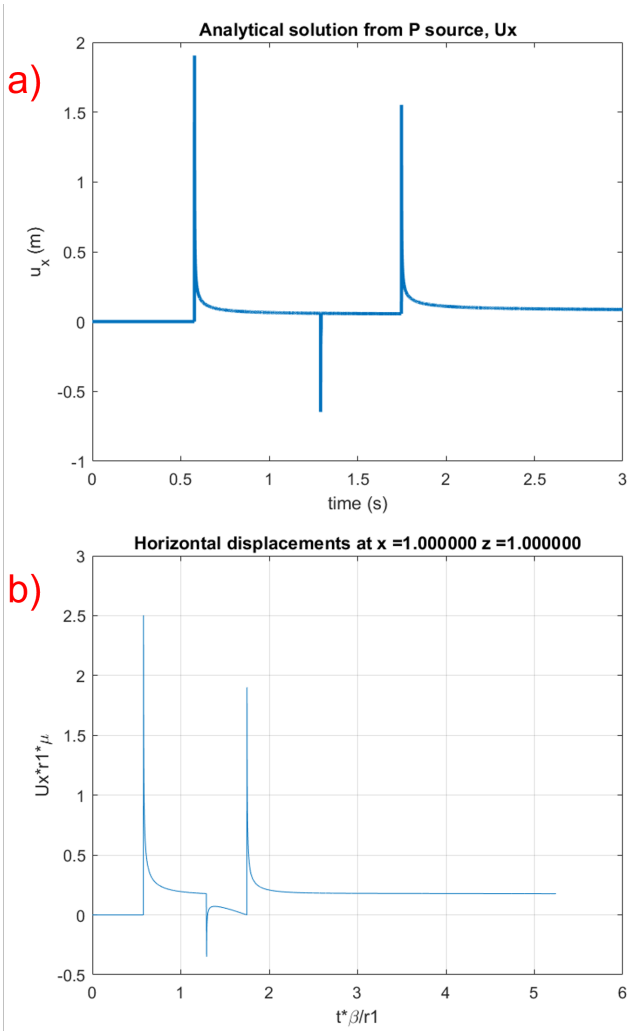


Figure 3.7: Comparison of horizontal displacement analytical solution from P source in elastic half-space and a free surface between solution from this work (a) and solution from the literature (b). Solutions from the literature is adapted from (Sanchez-Sesma et al., 2012). The source and receiver depths are at $z = 1\ m$ and $z_0 = 1\ m$ while the distance between them is $x = 1\ m$. The P and S waves velocity are $\alpha = 1.73\ m/s$ and $\beta = 1\ m/s$ which are scaled.

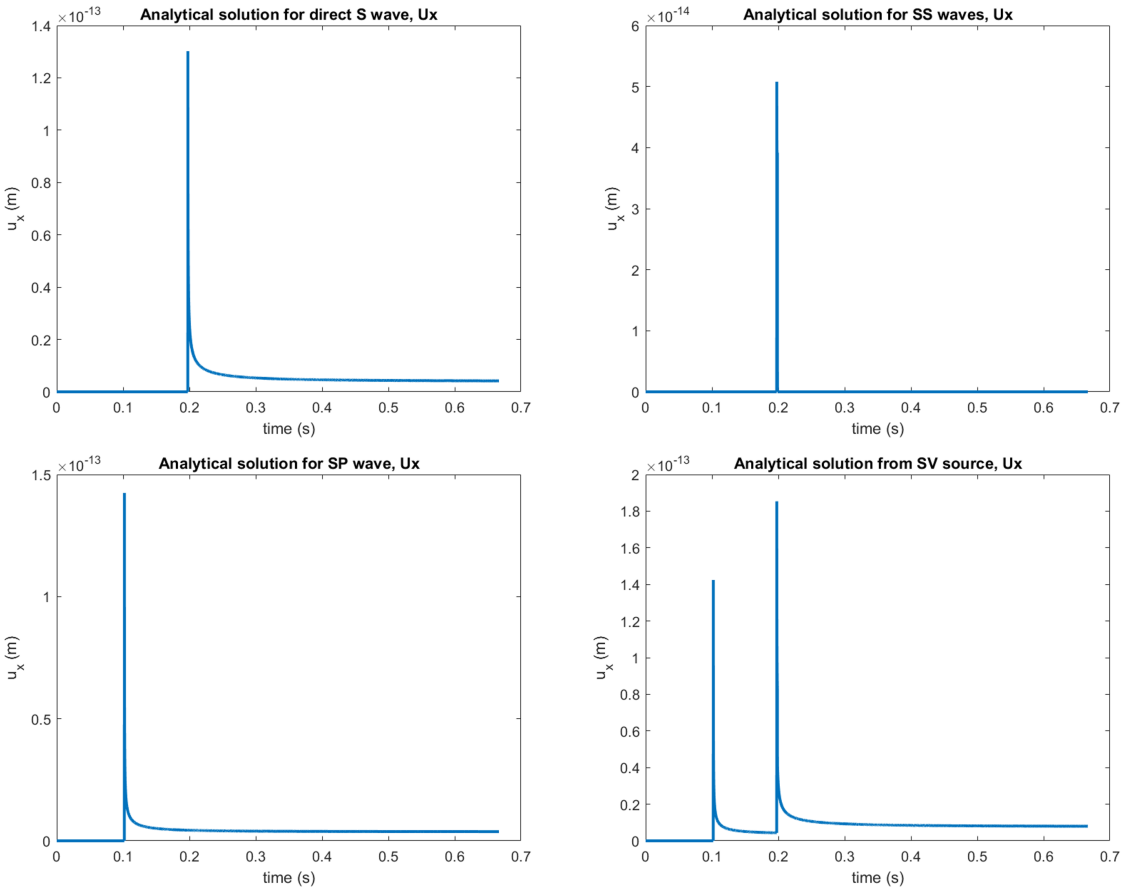


Figure 3.8: Horizontal displacements analytical solutions assuming a Lamb's problem utilizing the SV source at depth $z = 0.01\ m$. Each displacement solution is calculated at a distance $x = 500\ m$ with a depth of $z_0 = 100\ m$.

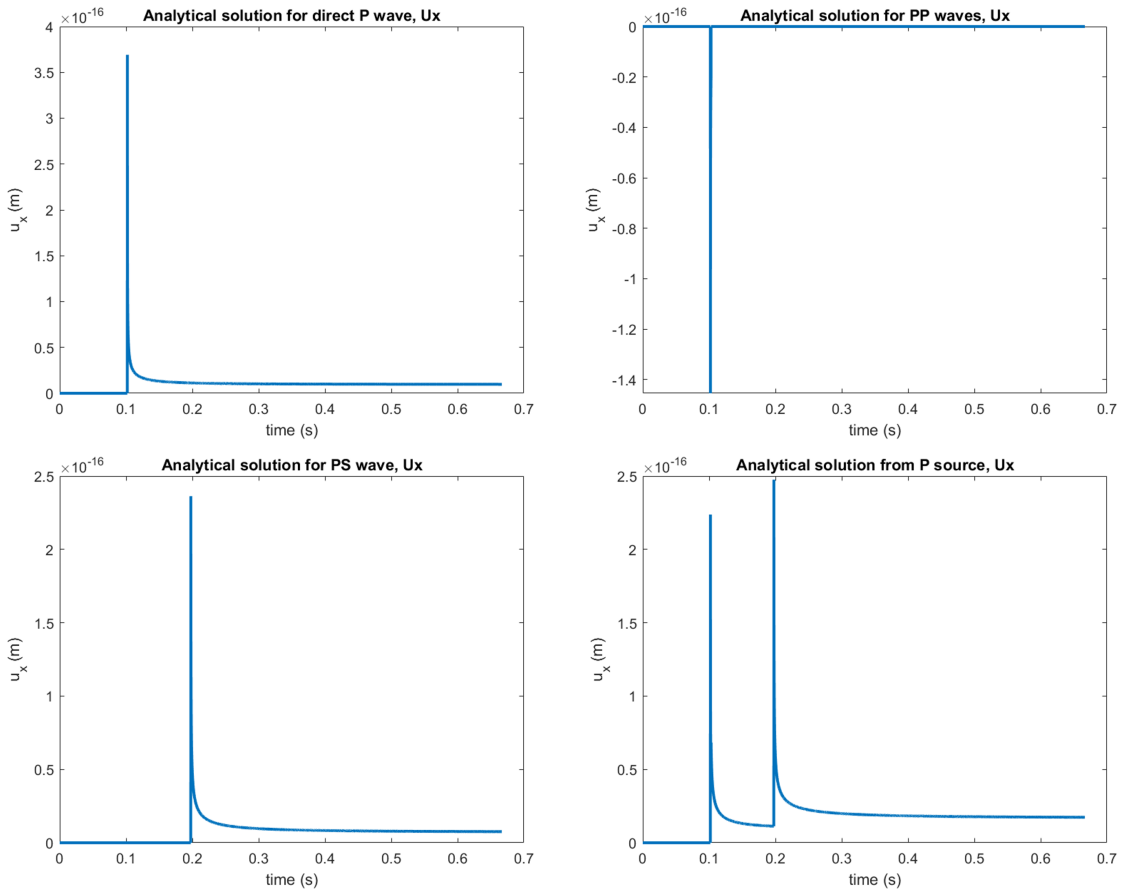


Figure 3.9: Horizontal displacements analytical solutions utilizing the P effective source at depth $z = 0.01\ m$. Each displacement solution is calculated at a distance $x = 500\ m$ with a depth of $z_0 = 100\ m$.

reflected SS wave arrival and are both positive. In fact, both the S and SS constructively combine with a value of $u_x = 1.9 \times 10^{-13}\ m$ .

In Lamb's problem, the analytical solution are solved using either a P or SV source. However, the conceptual body force model excites both P and SV effective source due to the mechanical deformation present from the pressure source on top of the sea-bottom. The horizontal analytical solutions using the effective P and SV source from equation 3.57 are shown in figures 3.9 and 3.10, respectively. The previous figures used the same physical model as the Lamb's problem calculations. From figure 3.9, the effective P source is characterized by both the distance from the source $h$ and Poisson ratio $\nu$. Due to the unique scaling factor characterizing the the effective P

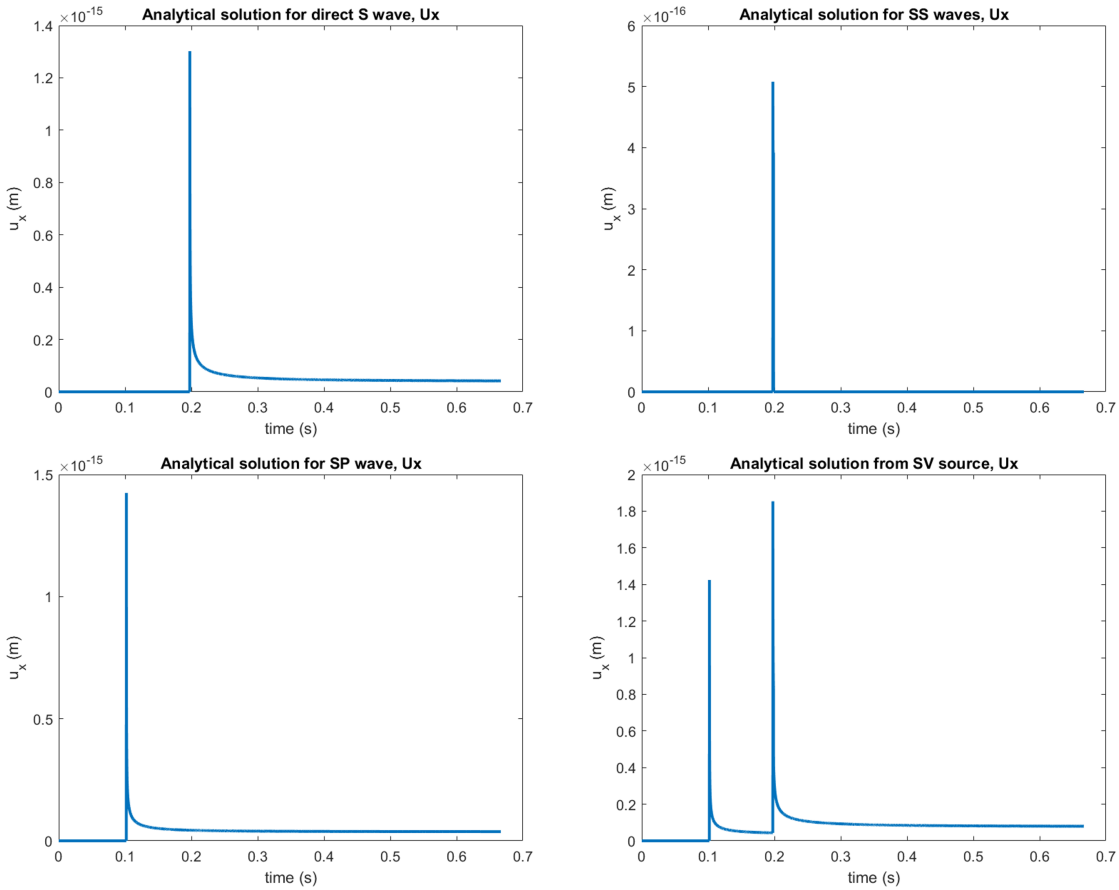


Figure 3.10: Horizontal displacements analytical solutions utilizing the SV effective source at depth $z = 0.01\ m$. Each displacement solution is calculated at a distance $x = 500\ m$ with a depth of $z_0 = 100\ m$.

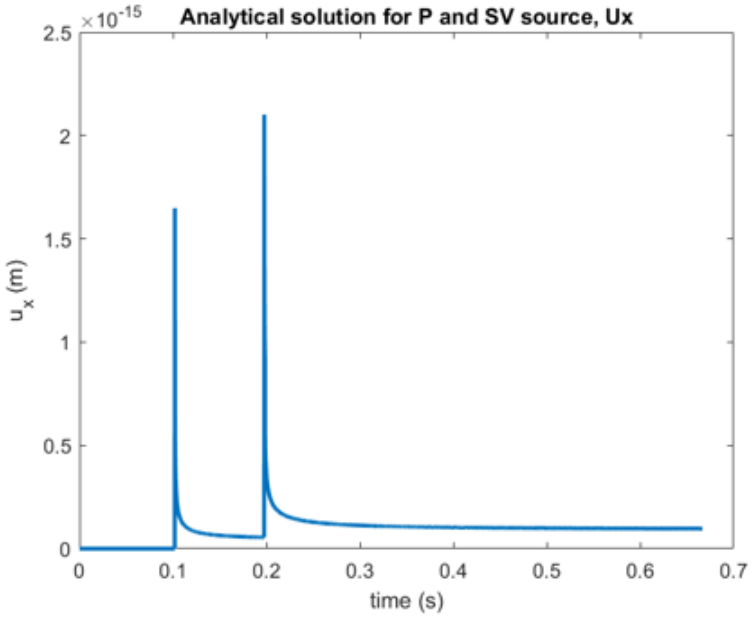


Figure 3.11: Total horizontal displacements solutions utilizing both the effective P and SV sources at depth $z = 0.01\ m$. Each displacement solution is calculated at a distance $x = 500\ m$ with a depth of $z_0 = 100\ m$.

source, the resulting amplitudes are affected. The direct P wave arrives at $t = 0.1\ s$ and has an amplitude of $u_x = 3.7 \times 10^{-16}\ m$. The reflected PP arrives at $t = 0.1\ s$ and has an amplitude of $u_x = -1.4 \times 10^{-16}\ m$. The converted PS arrives at $t = 0.2\ s$ and has an amplitude of $u_x = 2.4 \times 10^{-16}\ m$. Similarly, the total solution from the P effective source is dominated by the P and PS wave arrivals with the combined P and PP wave events having lower amplitude to the PS wave. From figure 3.10, the effective SV source is characterized only by the distance from the source $h$. The direct S wave arrives at $t = 0.2\ s$ and has an amplitude of $u_x = 1.3 \times 10^{-15}\ m$. The reflected SS arrives at $t = 0.2\ s$ and has an amplitude of $u_x = 5.0 \times 10^{-16}\ m$. The arrival times of both direct S and reflected SS coincide due to the placement of the source at the interface. The converted SP arrives at $t = 0.1\ s$ and has an amplitude of $u_x = 1.4 \times 10^{-15}\ m$. In the conceptual body force model, the total solutions from both sources can be combined as shown in figure 3.11. As shown from figure 3.11, the total horizontal displacement solutions is the summation of all wave events excited from the effective P and SV source. The four observable

main events; namely, the P, PS, S, and SP waves are summed to show only two main events since the P and SP waves coincides together as do the S and PS waves given the source location at the interface. The maximum amplitude for the direct P and SP waves are $u_x = 1.65 \times 10^{-15}\ m$ and maximum amplitude for the direct S and PS waves are $u_x = 2.2 \times 10^{-15}\ m$. Calculating the total waves from both effective source shows that the total transmitted SV wave is stronger than the P waves in the shallow water setting which confirms the strong shear waves observed in the shallow waters of the Arabian Gulf.

Analytical solutions represent the exact solution for a propagating wavefield. Given their complexity, analytical solutions are limited to a whole-space or half-space and every single ray path must be solved for independently considering time-domain solutions. In more complex situations, numerical solution of propagating wavefields provide an approximate solution that are robust when considering methods such as finite-difference. In this chapter, 2D finite-difference wave propagation modeling will be used to analyze the source mechanism and the complex wavefield interactions across the sea-bottom. The numerical solutions will include multiple case studies for different source depth and sea-bottom properties using different 2D model geometries for P-SV waves only.

## 4.1 Theory

To simulate a seismic model, it involves solving the wave equations that propagate in the Earth. One of the most robust numerical techniques to solve the differential equations associated with the wave equations is the finite-difference modeling (FDM). FDM consists of numerical approximations of derivatives of differential wave equations that are discretized in space and time. There are multiple approaches to implement FDM; however, the approach that will be considered is the explicit one, also known as the time marching approach, where the wave equations remain in the time domain and are solved recursively. The explicit approach can be implemented in several ways; most notable is the staggered-grid method which will be utilized to solve the wave equation numerically (Madariaga, 1976; Viruex, 1986, Levander, 1988; Graves, 1996).

The following finite difference derivation follows the work of Ikelle and Amundsen (2005). The governing equations for the wave propagation in 2D are given from equations 2.8 and 2.13, which becomes

$$\begin{aligned} \rho(\boldsymbol{x})\frac{\partial v_x(\boldsymbol{x},t)}{\partial t} - \frac{\partial \tau_{xx}(\boldsymbol{x},t)}{\partial x} - \frac{\partial \tau_{xz}(\boldsymbol{x},t)}{\partial z} &= f_x(\boldsymbol{x},t) \\ \rho(\boldsymbol{x})\frac{\partial v_z(\boldsymbol{x},t)}{\partial t} - \frac{\partial \tau_{xz}(\boldsymbol{x},t)}{\partial x} - \frac{\partial \tau_{zz}(\boldsymbol{x},t)}{\partial z} &= f_z(\boldsymbol{x},t) \end{aligned} \tag{4.1}$$

$$
\begin{aligned}
\frac{\partial \tau_{xx}(\boldsymbol{x},t)}{\partial t} &= [\lambda(\boldsymbol{x})+2\mu(\boldsymbol{x})]\frac{\partial v_x(\boldsymbol{x},t)}{\partial x} + \lambda(\boldsymbol{x})\frac{\partial v_z(\boldsymbol{x},t)}{\partial z} + I_{xx}(\boldsymbol{x},t),\\
\frac{\partial \tau_{zz}(\boldsymbol{x},t)}{\partial t} &= [\lambda(\boldsymbol{x})+2\mu(\boldsymbol{x})]\frac{\partial v_z(\boldsymbol{x},t)}{\partial z} + \lambda(\boldsymbol{x})\frac{\partial v_x(\boldsymbol{x},t)}{\partial x} + I_{zz}(\boldsymbol{x},t),\\
\frac{\partial \tau_{xz}(\boldsymbol{x},t)}{\partial t} &= \mu(\boldsymbol{x})\left[\frac{\partial v_z(\boldsymbol{x},t)}{\partial x} + \frac{\partial v_x(\boldsymbol{x},t)}{\partial z}\right] + I_{xz}(\boldsymbol{x},t).
\end{aligned}
\tag{4.2}
$$

In the previous equations, a temporal derivative was taken changing displacement to velocity and stresses into stress-rate which means $\boldsymbol{I} = (I_{xx}, I_{zz}, I_{xz})$ are the components of the stress-rate source. This is done so that the previous equations satisfy a set of first-order coupled differential equations instead of second-order. Given that the numerical solutions are an approximation, this process will reduce the resulting error when applying the staggered-grid method. To solve equations 4.1 and 4.2, appropriate boundary conditions must first be specified. The initial conditions are

$$
\begin{aligned}
\boldsymbol{v} &= \frac{\partial \boldsymbol{v}}{\partial t} = 0, \qquad t \leq 0,\\
\boldsymbol{\tau} &= \frac{\partial \boldsymbol{\tau}}{\partial t} = 0, \qquad t \leq 0.
\end{aligned}
$$

When considering a free surface at depth $z = 0$, the boundary conditions are

$$
\tau_{zz}(x, z=0, t) = \tau_{xz}(x, z=0, t) = 0, \tag{4.3}
$$

substituting equation 4.2 into equation 4.3 yields

$$
\begin{aligned}
&[\lambda(\boldsymbol{x})+2\mu(\boldsymbol{x})]\frac{\partial v_z(x, z=0, t)}{\partial z} + \lambda(\boldsymbol{x})\frac{\partial v_x(x, z=0, t)}{\partial x}\\
&= \mu(\boldsymbol{x})\left[\frac{\partial v_z(x, z=0, t)}{\partial x} + \frac{\partial v_x(x, z=0, t)}{\partial z}\right] = 0.
\end{aligned}
\tag{4.4}
$$

The rest of the model is unbounded. The main part in numerically solving the first-order differential equation is to discretize the physical parameters. First, the spatial and temporal parameters $x$, $z$,

and $t$ are discretized and form what is known as the reference grid. They are discretized as follows

$$\begin{aligned} t &= n\Delta t, \qquad n = 0, 1, 2, \ldots, N, \\ x &= i\Delta x, \qquad i = 0, 1, 2, \ldots, I, \\ z &= k\Delta z, \qquad k = 0, 1, 2, \ldots, K, \end{aligned} \tag{4.5}$$

where $\Delta x$ and $\Delta z$ represent the spatial grid spacing, and $\Delta t$ represents the time sampling. Using the reference grid, equations 4.1 and 4.2 can be defined using the indexes $n$, $i$, and $k$ as demonstrated in the following examples

$$\begin{aligned} &\lambda(x, z) = \lambda\left[\left(i + \frac{1}{2}\right)\Delta x, \left(k + \frac{1}{2}\right)\Delta z\right] = \lambda_{i+1/2,k+1/2}, \\ &\tau_{xz}(x, z, t) = \tau_{xz}(i\Delta x, k\Delta z, n\Delta t) = [\tau_{xz}]^n_{i,k}\,. \end{aligned} \tag{4.6}$$

From the previous equation, not all quantities calculated are gridded on the reference grid; instead, some are calculated half-grids away. This means some of the quantities of the differential equations are calculated on the reference grids and the rest are calculated between the reference grid; i.e., half-grid between the reference grid. This technique is commonly known as the staggered-grid technique. Therefore, the discrete forms of equations 4.1 and 4.2 utilizing the staggered-grid method are given by (Madariaga, 1976; Graves, 1996)

$$\begin{aligned} &[v_x]^{n+1/2}_{i,k+1/2} = [v_x]^{n-1/2}_{i,k+1/2} + [\Delta t b_x(D_x\tau_{xx} + D_z\tau_{xz} + f_x]^n_{i,k+1/2}, \\ &[v_z]^{n+1/2}_{i+1/2,k} = [v_z]^{n-1/2}_{i+1/2,k} + [\Delta t b_z(D_x\tau_{xz} + D_z\tau_{zz} + f_x]^n_{i+1/2,k}, \\ &[\tau_{xx}]^{n+1}_{i+1/2,k+1/2} = [\tau_{xx}]^n_{i+1/2,k+1/2} + \Delta t[(\lambda + 2\mu)D_x v_x + \lambda D_z v_z + I_{xx}]^{n+1/2}_{i+1/2,k+1/2}, \\ &[\tau_{zz}]^{n+1}_{i+1/2,k+1/2} = [\tau_{zz}]^n_{i+1/2,k+1/2} + \Delta t[(\lambda + 2\mu)D_z v_z + \lambda D_x v_x + I_{zz}]^{n+1/2}_{i+1/2,k+1/2}, \\ &[\tau_{xz}]^{n+1}_{i,k} = [\tau_{xz}]^n_{i,k} + \Delta t[\mu_{xz}(D_z v_x + D_x v_z) + I_{xz}]^{n+1/2}_{i,k}, \end{aligned} \tag{4.7}$$

with $b_x$ and $b_z$ being the effective medium parameters defined as

$$\begin{aligned} b_x &= \frac{1}{2}[b_{i,k} + b_{i-1,k}], \\ b_z &= \frac{1}{2}[b_{i,k} + b_{i,k-1}], \end{aligned} \tag{4.8}$$

where $b$ is the reciprocal of density defined as $b_{i,k} = \dfrac{1}{\rho_{i,k}}$. $D_x$ and $D_z$ are spatial operators that represents the first-order spatial derivative for x and z; respectively. The FDM used utilizes a fourth-order difference which is more accurate and is defined as

$$D_x g_{i,k} \approx \frac{1}{\Delta x}\left[\frac{9}{8}(g_{i+1/2,k} - g_{i-1/2,k}) - \frac{1}{24}(g_{i+3/2,k} - g_{i-3/2.k})\right], \tag{4.9}$$

where $g_{i,k}$ is a dummy variable. Aside from the accuracy of the calculation, the order of the FDM is subject to the phsyical parameters of the model such as the minimum wavelength. Based on those parameters, a propagating wavelength must be adequately discretized to be sampled a minimum number of times to ensure grid spatial stability. The minimum grid spacing, assuming $\Delta x = \Delta z$, allowed is

$$\Delta x \leq \frac{\lambda_{min}}{n} = \frac{V_{min}}{n f_{max}}, \tag{4.10}$$

where $\lambda_{min}$ denotes the minimum wavelength, $V_{min}$ the minimum velocity in the model, and $f_{max}$ is the maximum frequency of the source signal. The number of grid points per wavelength, $n$, depends on the FDM order accuracy. A fourth-order accurate FDM requires atleast $n = 8$ to avoid grid dispersion. Beside the spatial criteria, the temporal discretization must satisfy a sampling criteria to ensure the stability of the FDM code. This criterion is commonly referred to as Courant-Friedrichs-Lewy criterion (Courant et al., 1967) and is defined as

$$\Delta t \leq \frac{\Delta x}{h\sqrt{2}V_{max}}, \tag{4.11}$$

where $V_{max}$ is the maximum velocity in the model, and $h$ is the factor associated with the temporal order of the FDM. A second-order temporal finite-difference is used; thus, $h = 1$. Satisfying the

grid dispersion and the Courant stability ensures the stability of the FDM; however, higher values of sampling are required when dealing with complex wave interactions such as surface waves. The free-surface boundary condition from equation 4.4 requires the normal and shear stresses to be zero at $z = 0$. As shown from the staggered-grid, knowledge of spatial derivatives couple of grids prior to the calculation point is required. For horizontal spatial derivatives, the staggered-grid implementation does not run into issues since the medium is unbounded; however, the vertical spatial derivative require adjustment due to the free-surface boundary. The implementation of the free-surface in FDM code involves adding two grid points above $z = 0$ assuming antisymmetry for the stress components at $z = 0$; thus, the stress fields at and above the surface become

$$\begin{aligned}
&[\tau_{xz}]^{n+1}_{i,k=0} = 0, \quad [\tau_{xz}]^{n+1}_{i,k=-1} = -[\tau_{xz}]^{n+1}_{i,k=1}, \\
&[\tau_{zz}]^{n+1}_{i+1/2,k=-1/2} = -[\tau_{zz}]^{n+1}_{i+1/2,k=1/2}, \\
&[\tau_{zz}]^{n+1}_{i+1/2,k=-3/2} = -[\tau_{zz}]^{n+1}_{i+1/2,k=3/2}.
\end{aligned} \tag{4.12}$$

To deal with the unbounded medium, a damping coefficient is applied by surrounding the numerical model with a strip of grids that exponentially decay any propagating wavefield. The stress and particle velocity are multiplied by the damping factor

$$G(i) = exp\left\{-\left[\frac{a}{iabmax}(iabmax - i)\right]^2\right\}, \quad 1 \leq i \leq iabmax, \tag{4.13}$$

where $iabmax$ is the grid strip width and $a$ is the absorbing constant.

## 4.2 Finite-Difference Modeling with Different Model Cases for a fluid/elastic half-space

Using the finite-difference method, numerical solution of the full waveform can be found. The FDM code can be used to simulate both the deep and shallow marine environment. The goal of the numerical simulation is to understand the source mechanism across the horizontal boundary given different model cases that will describe the impact of the source mechanism. The first part of the analysis will involve the shallow source depth with varying sea-bottom properties followed by the far source depth with varying sea-bottom properties. The sea-bottom properties will vary from soft

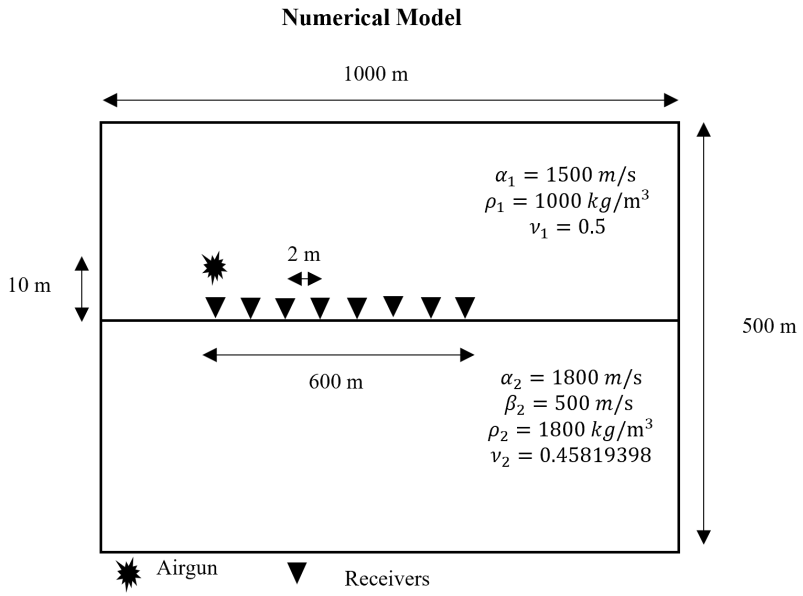


Figure 4.1: Physical model (Model 1) with a shallow source at $h = 10\ m$ and a Poisson ratio of $\nu = 0.458$ which represents soft unconsolidated mud.

unconsolidated mud to hard coral reef solid.

Considering the shallow source depth analysis, the first model used for the numerical solution is shown in figure 4.1. The physical model (Model 1) shows a fluid half-space above an elastic half-space. The pressure source is placed $10\ meters$ above the sea-bottom in the water layer and its placement is similar to the shallow marine environment. In the lower elastic layer, the P wave velocity is $\alpha = 1800\ m/s$, S wave velocity is $\beta = 500\ m/s$, and Poisson ratio is $\nu = 0.458$ which are indicative of an elastic sea-bottom characterized by a soft unconsolidated mud. From the source, 600 receivers are placed on the seafloor that are $2\ meters$ apart. The total dimensions of the physical model are $500\ meters$ in the vertical direction and $1000\ meters$ in the horizontal direction. To investigate the propagation of waves from the source, the medium will be considered unbounded. Numerical solution for the horizontal component using Model 1 is shown in figure 4.2. The wavelet used is a Ricker wavelet and the source frequency is $25\ Hz$. Given the 4th order of the FDM, the grid spacing chosen for this simulation is $1\ meters$ according to equation 4.10. As a result, the minimum sampling rate from the Courant criteria is $\Delta t = 0.3\ ms$; this ensures

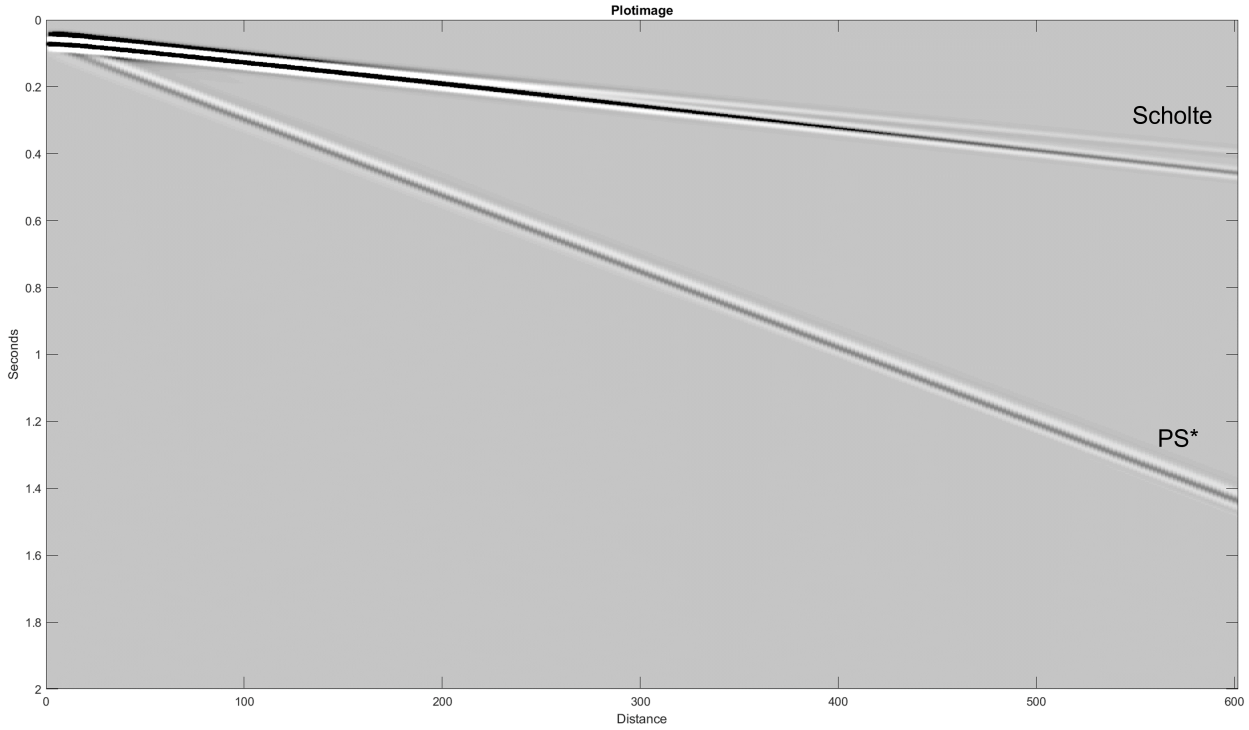


Figure 4.2: Horizontal particle velocity for Model 1. The vertical axis is the time in $seconds$ and the horizontal axis is the distance in $meters$.

the stability of the FDM code and avoids grid dispersion. Two main events are observed from the numerical solution, the surface Scholte wave and a direct transmitted S wave. The PP and PS events appear to overlap due to the coupling between P and SV waves at the sea-bottom boundary which are masked by the surface Scholte waves. At greater distance; however, the PP waves are faster and starter to be arrive before the surface wave. The second event is the PS* waves which are wave arrivals that are interpreted as evanescent P waves tunneling at the interface where they are converted to propagating shear waves (Daley and Hron, 1983). There are two main characteristics of the S* waves. First, they are evanescent waves which means they exponentially decay with depth. Second, they are considered non-geometric waves in the sense that the waves propagate as if they are excited from the sea-bottom instead of the airgun source (Hron and Mikhailenko, 1981). However, when the source is moved closer to the interface then the PS* wave mode becomes more prominent (Gutowski et al., 1984). For the PS* to exist in the fluid/elastic half-space medium, shear wave velocity in the solid medium must be lower than the acoustic wave velocity of the

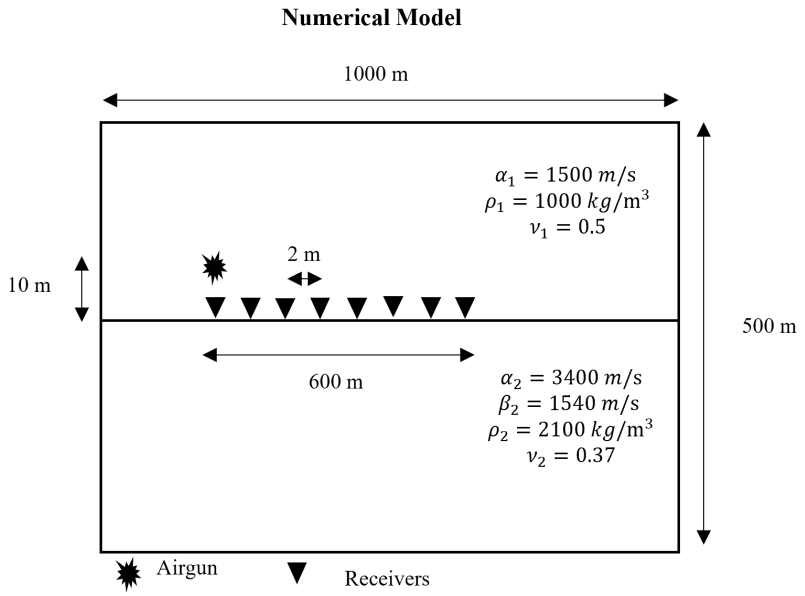


Figure 4.3: Physical model (Model 2) with a shallow source at $h = 10\ m$ and a Poisson ratio of $\nu = 0.37$ which represents an intermediate consolidated solid.

water layer;i.e., $\beta_2 < \alpha_1$ (Allouche and Drijkoningen, 2016).

The second model used for the numerical solution is shown in figure 4.3. The physical model (Model 2) shows a fluid half-space above an elastic half-space. The pressure source is placed $10\ meters$ above the sea-bottom in the water layer and its placement is similar to the shallow marine environment. In the lower elastic layer, the P wave velocity is $\alpha = 3400\ m/s$, S wave velocity is $\beta = 1540\ m/s$, and Poisson ratio is $\nu = 0.37$ which are indicative of an elastic sea-bottom characterized by an intermediate consolidated solid. From the source, 600 receivers are placed on the seafloor that are $2\ meters$ apart. The total dimensions of the physical model are $500\ meters$ in the vertical direction and $1000\ meters$ in the horizontal direction. To investigate the propagation of waves from the source, the medium will be considered unbounded. Numerical solution for the horizontal component using Model 2 is shown in figure 4.4. The wavelet used is a Ricker wavelet and the source frequency is $25\ Hz$. The grid spacing chosen for this simulation is $2\ meters$ according to equation 4.10. As a result, the sampling rate to satisfy the Courant criteria is $\Delta t = 0.3\ ms$. This ensures the stability of the FDM code and avoids grid dispersion. Two main

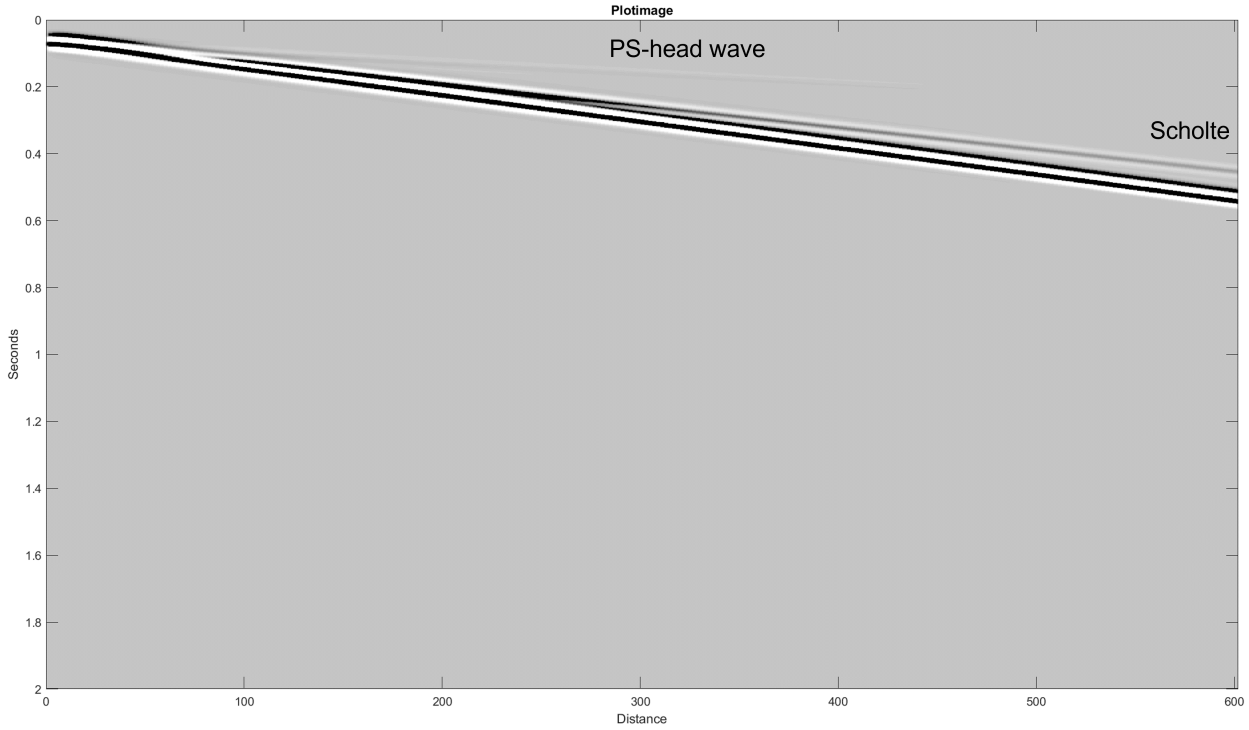


Figure 4.4: Horizontal particle velocity for Model 2. The vertical axis is the time in $seconds$ and the horizontal axis is the distance in $meters$.

events are observed from the numerical solution, the surface Scholte wave and the PS headwave. The PP and PS events appear to overlap due to the coupling between P and SV waves at the sea-bottom boundary which are masked by the surface Scholte waves. The other event is the refracted PS waves that exists due to having the shear wave velocity in the solid medium faster than the acoustic wave velocity of the water layer;i.e., $\beta_2 > \alpha_1$.

The third model used for the numerical solution is shown in figure 4.5. The physical model (Model 3) shows a fluid half-space above an elastic half-space. The pressure source is placed $10$ $meters$ above the sea-bottom in the water layer and its placement is similar to the shallow marine environment. In the lower elastic layer, the P wave velocity is $\alpha = 5000\ m/s$, S wave velocity is $\beta = 2580\ m/s$, and Poisson ratio is $\nu = 0.318$ which are indicative of an elastic sea-bottom characterized by a hard coral reef. From the source, 600 receivers are placed on the seafloor that are $2$ $meters$ apart. The total dimensions of the physical model are $500$ $meters$ in the vertical direction and $1000$ $meters$ in the horizontal direction. To investigate the propagation of waves

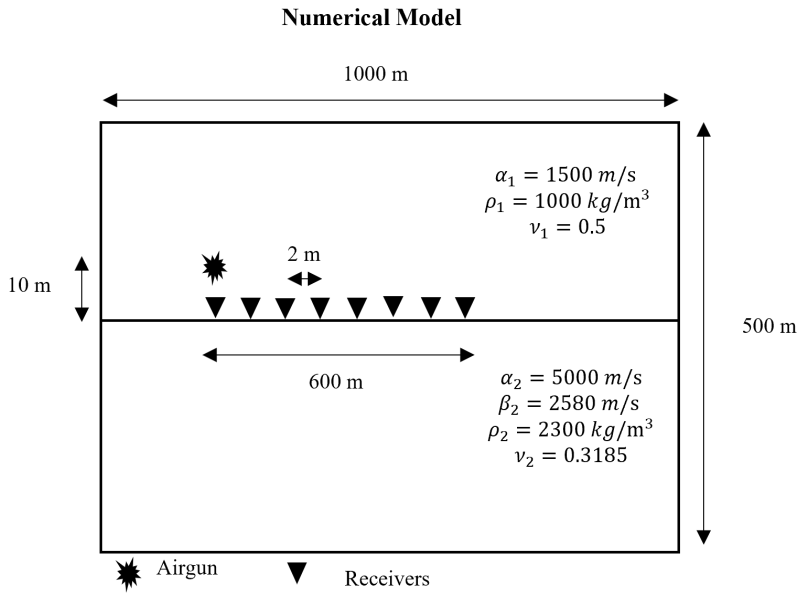


Figure 4.5: Physical model (Model 3) with a shallow source at $h = 10\ m$ and a Poisson ratio of $\nu = 0.318$ which represents a hard coral reef.

from the source, the medium will be considered unbounded. Numerical solution for the horizontal component using Model 3 is shown in figure 4.6. The wavelet used is a Ricker wavelet and the source frequency is $25\ Hz$. The grid spacing chosen for this simulation is $2\ meters$ according to equation 4.10. As a result, the sampling rate to satisfy the Courant criteria is $\Delta t = 0.24\ ms$. This ensures the stability of the FDM code and avoids grid dispersion. Two main events are observed from the numerical solution, the surface Scholte wave and the PS headwave. The PP and PS events appear to overlap due to the coupling between P and SV waves at the sea-bottom boundary which are masked by the surface Scholte waves. The other event is the refracted PS waves that exists due to having the shear wave velocity in the solid medium faster than the acoustic wave velocity of the water layer;i.e., $\beta_2 > \alpha_1$.

Considering the far source depth analysis, the fourth model used for the numerical solution is shown in figure 4.7. The physical model (Model 4) shows a fluid half-space above an elastic half-space. The pressure source is placed $100\ meters$ above the sea-bottom in the water layer and its placement is similar to the deep marine environment. In the lower elastic layer, the P wave

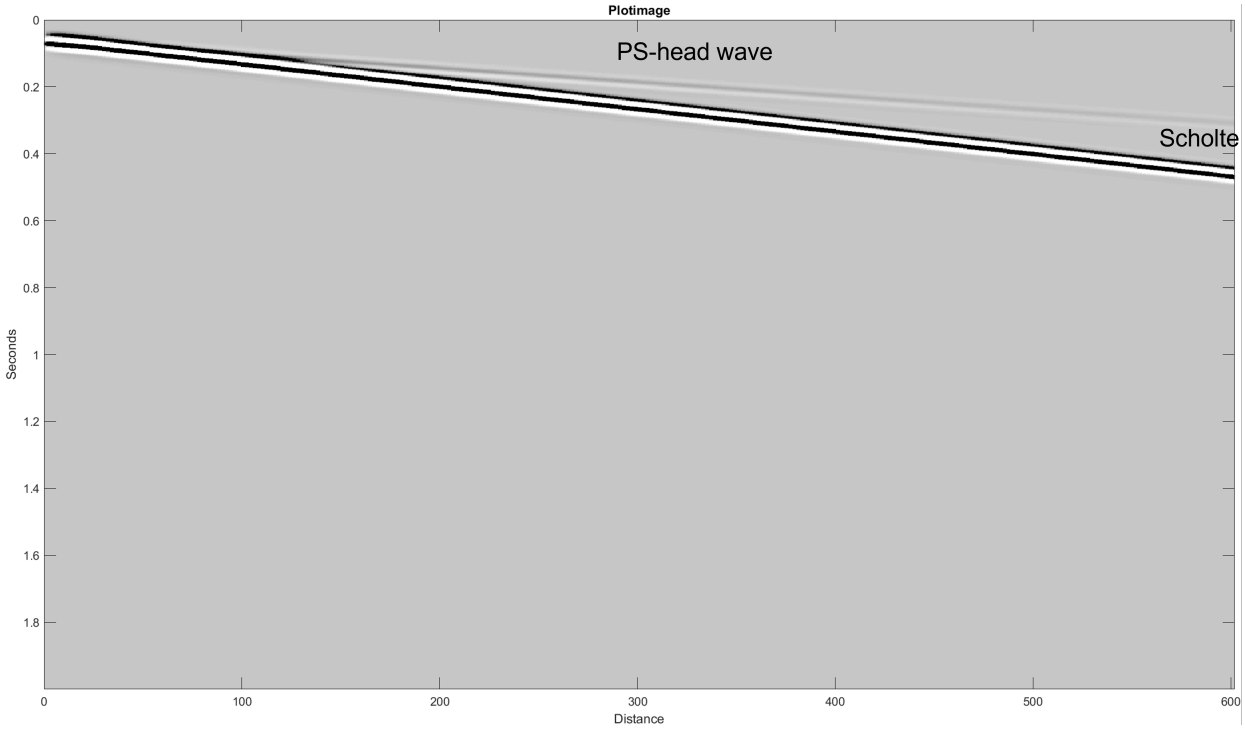


Figure 4.6: Horizontal particle velocity for Model 3. The vertical axis is the time in $seconds$ and the horizontal axis is the distance in $meters$.

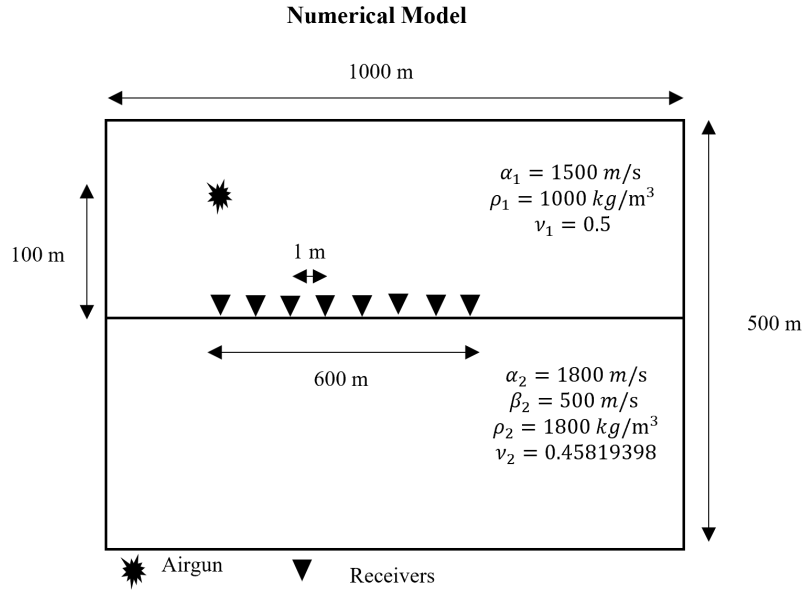


Figure 4.7: Physical model (Model 4) with a far source at $h = 100\ m$ and a Poisson ratio of $\nu = 0.458$ which represents soft unconsolidated mud.

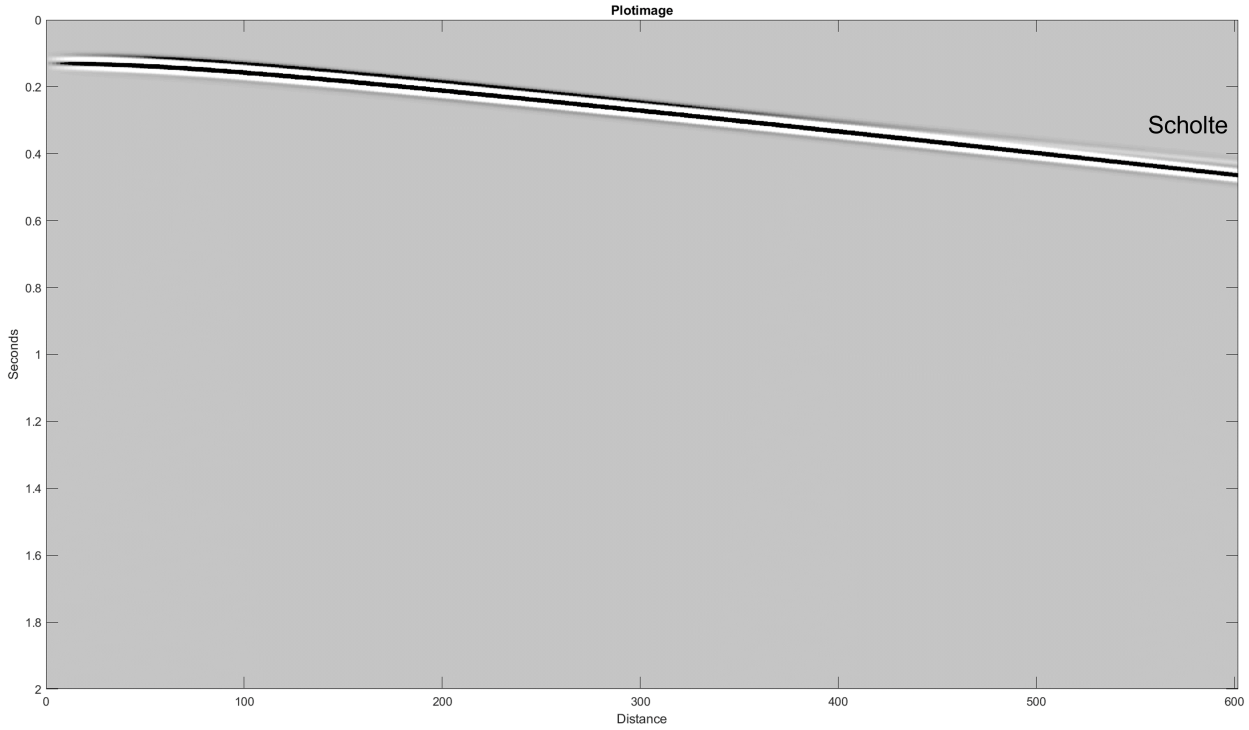


Figure 4.8: Horizontal particle velocity for Model 4. The vertical axis is the time in $seconds$ and the horizontal axis is the distance in $meters$.

velocity is $\alpha = 1800\ m/s$, S wave velocity is $\beta = 500\ m/s$, and Poisson ratio is $\nu = 0.458$ which are indicative of an elastic sea-bottom characterized by a soft unconsolidated mud. From the source, 600 receivers are placed on the seafloor that are $2\ meters$ apart. The total dimensions of the physical model are $500\ meters$ in the vertical direction and $1000\ meters$ in the horizontal direction. To investigate the propagation of waves from the source, the medium will be considered unbounded. Numerical solution for the horizontal component using Model 4 is shown in figure 4.8. The wavelet used is a Ricker wavelet and the source frequency is $25\ Hz$. Given the 4th order of the FDM, the grid spacing chosen for this simulation is $1\ meters$ according to equation 4.10. As a result, the minimum sampling rate from the Courant criteria is $\Delta t = 0.3\ ms$. This ensures the stability of the FDM code and avoids grid dispersion. One main event is observed from the numerical solution which is the surface Scholte wave. The PP and PS events appear to overlap due to the coupling between P and SV waves at the sea-bottom boundary which are masked by the surface Scholte waves. Since the source isn't placed within a wavelength of the interface, the PS*

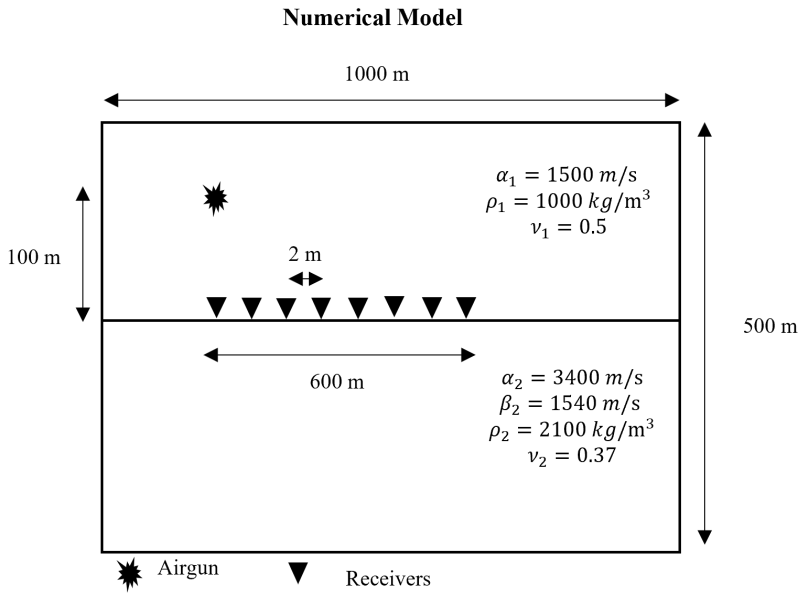


Figure 4.9: Physical model (Model 5) with a far source at $h = 100\ m$ and a Poisson ratio of $\nu = 0.37$ which represents an intermediate consolidated solid.

event isn't observed for Model 4. This is due to the evanescent nature of the PS* waves and they can only exist when the source is located close to the interface (within one wavelength), although the velocity criteria is satisfied.

The fifth model used for the numerical solution is shown in figure 4.9. The physical model (Model 5) shows a fluid half-space above an elastic half-space. The pressure source is placed $100\ meters$ above the sea-bottom in the water layer and its placement is similar to the deep marine environment. In the lower elastic layer, the P wave velocity is $\alpha = 3400\ m/s$, S wave velocity is $\beta = 1540\ m/s$, and Poisson ratio is $\nu = 0.37$ which are indicative of an elastic sea-bottom characterized by an intermediate consolidated solid. From the source, 600 receivers are placed on the seafloor that are $2\ meters$ apart. The total dimensions of the physical model are $500\ meters$ in the vertical direction and $1000\ meters$ in the horizontal direction. To investigate the propagation of waves from the source, the medium will be considered unbounded. Numerical solution for the horizontal component using Model 5 is shown in figure 4.10. The wavelet used is a Ricker wavelet and the source frequency is $25\ Hz$. The grid spacing chosen for this simulation is $2$

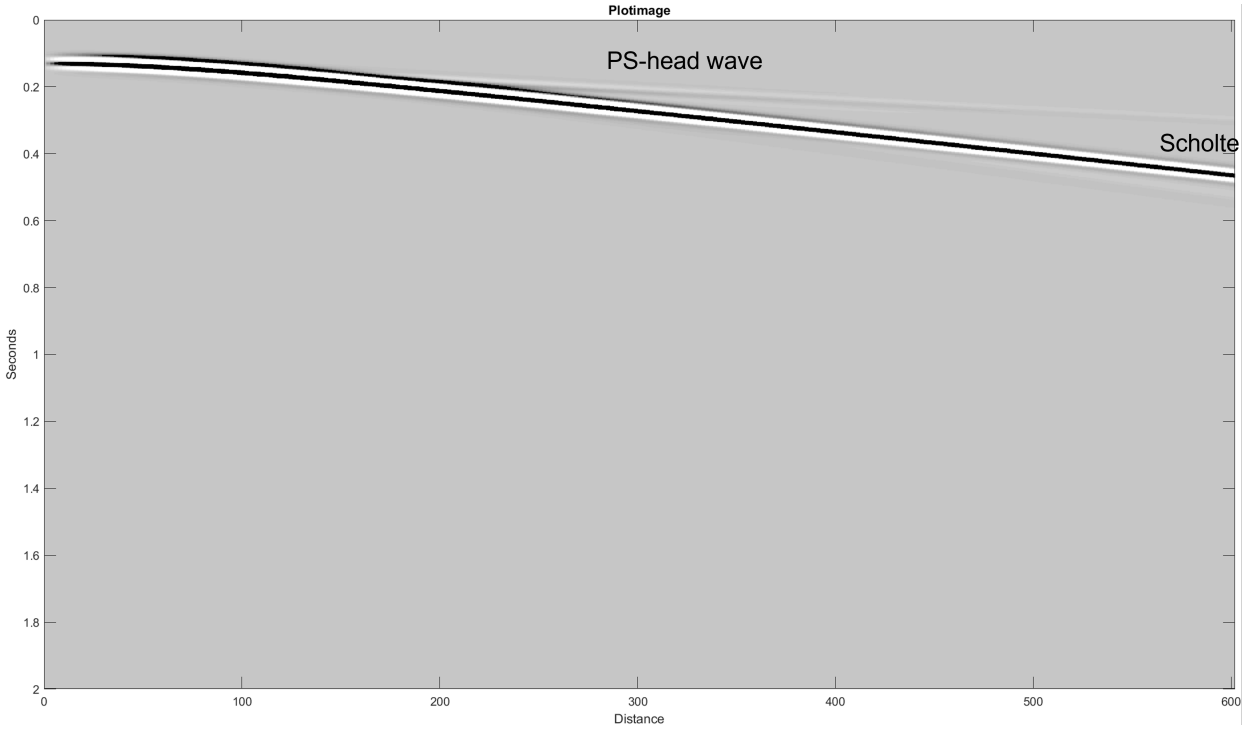


Figure 4.10: Horizontal particle velocity for Model 5. The vertical axis is the time in $seconds$ and the horizontal axis is the distance in $meters$.

$meters$ according to equation 4.10. As a result, the sampling rate to satisfy the Courant criteria is $\Delta t = 0.3\ ms$. This ensures the stability of the FDM code and avoids grid dispersion. Similar to the shallow source case, two main events are observed from the numerical solution;i.e., the Scholte wave and refracted PS wave. The PP and PS events appear to overlap due to the coupling between P and SV waves at the sea-bottom boundary. The other event is the refracted PS waves that exists due to the shear wave velocity in the solid medium is faster than the acoustic wave velocity of the water layer;i.e., $\beta_2 > \alpha_1$.

The sixth model used for the numerical solution is shown in figure 4.11. The physical model (Model 6) shows a fluid half-space above an elastic half-space. The pressure source is placed $100$ $meters$ above the sea-bottom in the water layer and its placement is similar to the deep marine environment. In the lower elastic layer, the P wave velocity is $\alpha = 5000\ m/s$, S wave velocity is $\beta = 2580\ m/s$, and Poisson ratio is $\nu = 0.318$ which are indicative of an elastic sea-bottom characterized by a hard coral reef. From the source, 600 receivers are placed on the seafloor that

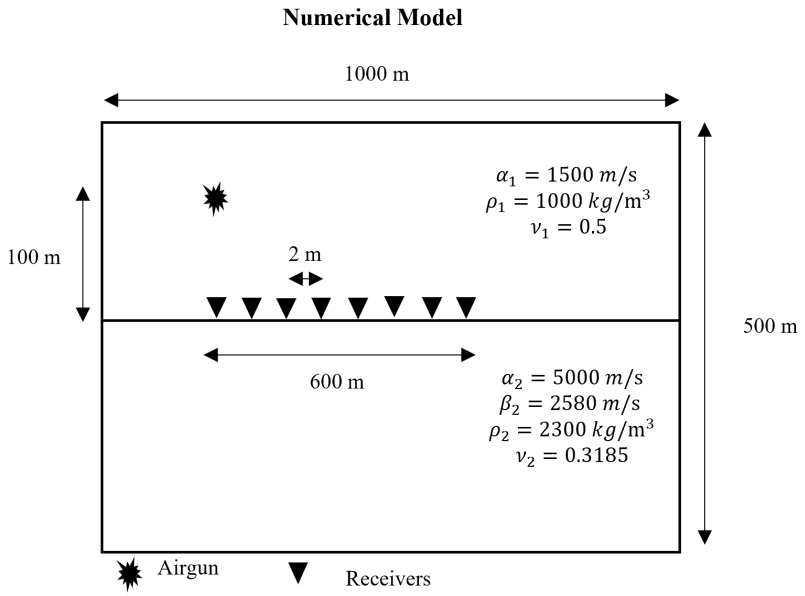


Figure 4.11: Physical model (Model 6) with a far source at $h = 100\ m$ and a Poisson ratio of $\nu = 0.318$ which represents a hard coral reef.

are $2\ meters$ apart. The total dimensions of the physical model are $500\ meters$ in the vertical direction and $1000\ meters$ in the horizontal direction. To investigate the propagation of waves from the source, the medium will be considered unbounded. Numerical solution for the horizontal component using Model 6 is shown in figure 4.12. The wavelet used is a Ricker wavelet and the source frequency is $25\ Hz$. The grid spacing chosen for this simulation is $2\ meters$ according to equation 4.10. As a result, the sampling rate to satisfy the Courant criteria is $\Delta t = 0.24\ ms$. This ensures the stability of the FDM code and avoids grid dispersion. Similar to the shallow source case, two main events are observed from the numerical solution;i.e.,the Scholte wave and refracted PS wave. The PP and PS events appear to overlap due to the coupling between P and SV waves at the sea-bottom boundary. The other event is the refracted PS waves that exists due to the shear wave velocity in the solid medium is faster than the acoustic wave velocity of the water layer;i.e., $\beta_2 > \alpha_1$.

For further analysis, figures 4.13 and 4.14 display the horizontal particle velocity for near, mid, and far offsets using the different model cases at shallow and far depth source positions.

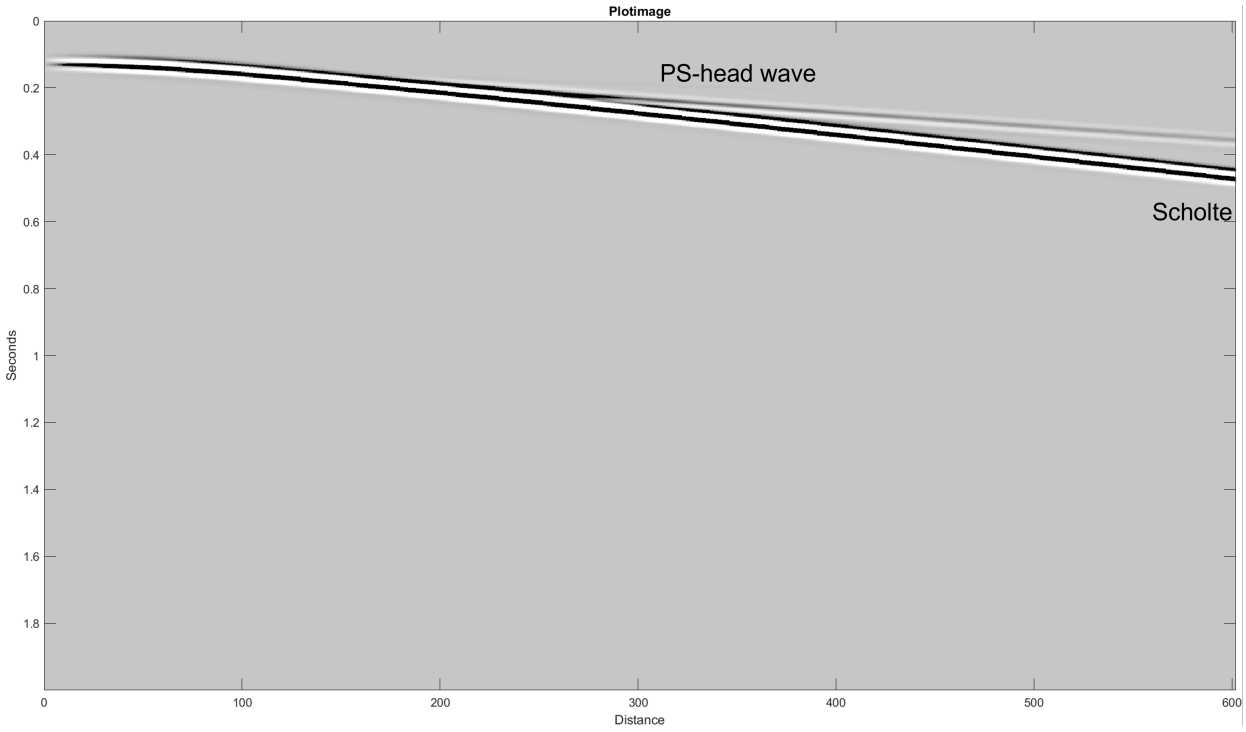


Figure 4.12: Horizontal particle velocity for Model 6. The vertical axis is the time in $seconds$ and the horizontal axis is the distance in $meters$.

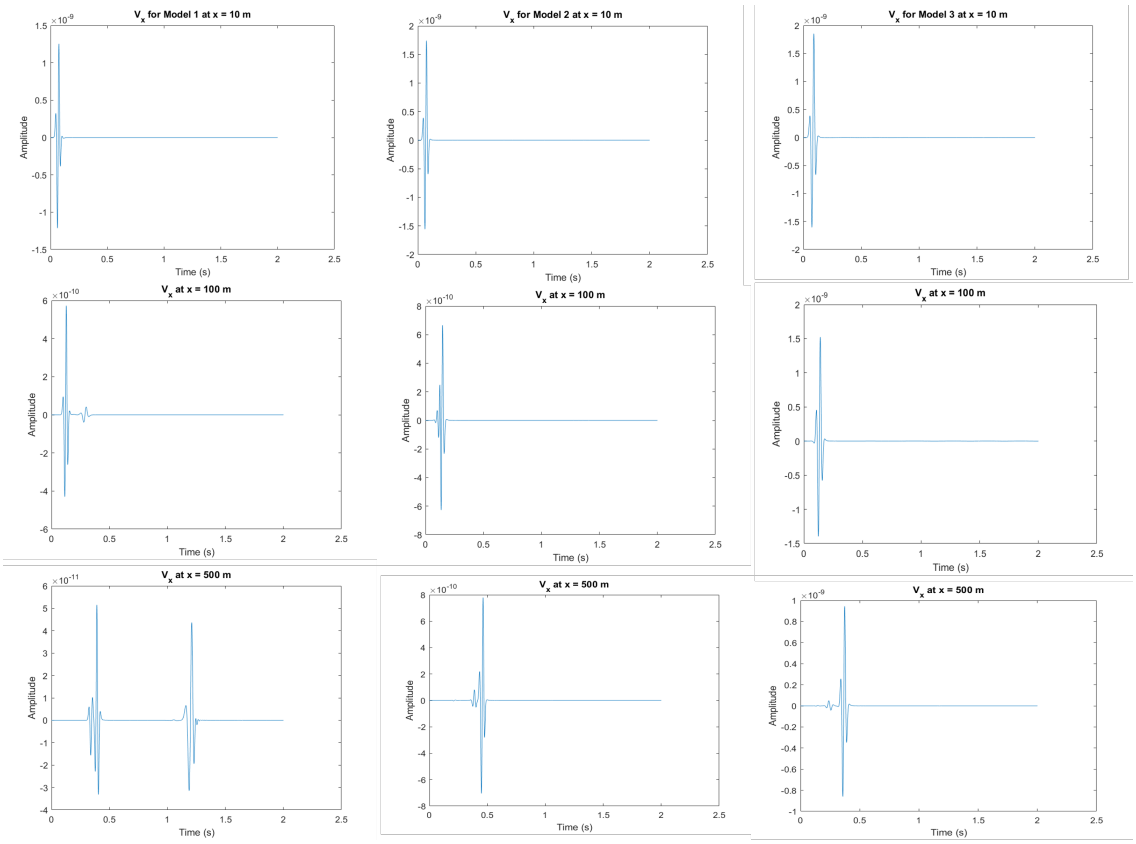


Figure 4.13: Horizontal particle velocity for Models 1, 2, and 3 at different distances. These models represent the shallow source depth case varying from soft unconsolidated mud to hard coral reef.

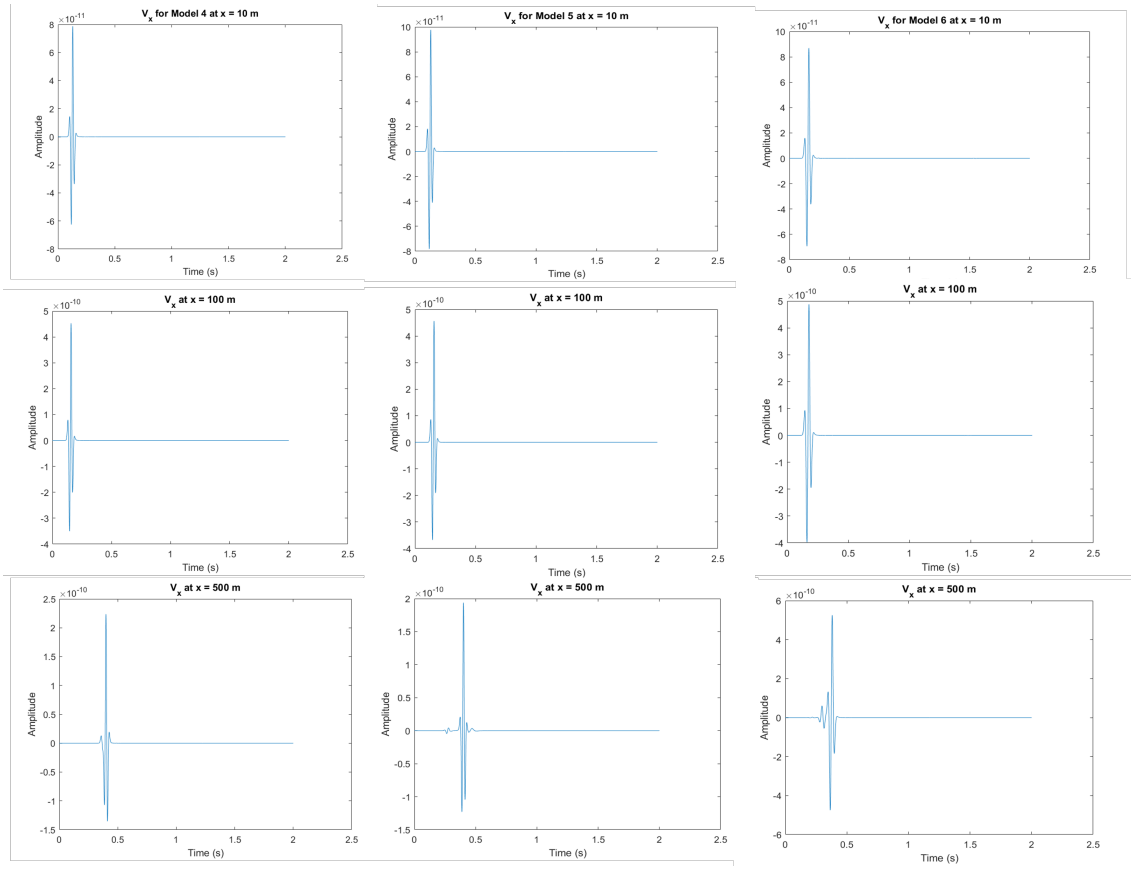


Figure 4.14: Horizontal particle velocity for Models 4, 5, and 6 at different distances. These models represent the far source depth case varying from soft unconsolidated mud to hard coral reef.

From figure 4.13, the horizontal velocity solution results are shown at $x = 10\ m$, $x = 100\ m$, and $x = 500\ m$ for Model 1, 2, and 3 which represents the shallow source depth models. At $x = 10\ m$, the PP and PS signals are indistinguishable for all the models and are masked by the Scholte surface waves. The peak amplitude at this offset is $V_x = 1.2 \times 10^{-9}\ m$ for Model 1, $V_x = 1.7 \times 10^{-9}\ m$ for Model 2, and $V_x = 1.8 \times 10^{-9}\ m$ for Model 3. At $x = 100\ m$, the PS* event starts to form for Model 1. The peak amplitude is $V_x = 5.8 \times 10^{-10}\ m$ for Model 1, and $V_x = 6.8 \times 10^{-10}\ m$ for Model 2 while the peak amplitude drops slightly to $V_x = 6.8 \times 10^{-10}\ m$ for Model 3. At $x = 500\ m$, The Scholte and PS* waves are clearly distinguishable and the PP waves starts to arrive faster for Model 1. The refracted wave starts to arrive faster for Models 2 and 3 and are distinguishable. The peak amplitude of the Scholte and PS* waves are $V_x = 5.1 \times 10^{-11}\ m$ and $V_x = 4.5 \times 10^{-11}\ m$ for Model 1; respectively. The peak amplitude is $V_x = 7.8 \times 10^{-10}\ m$ and $V_x = 0.9 \times 10^{-9}\ m$ for Models 1 and 2; respectively. Those results indicate that the maximum amplitude is in the near-field and is highest for the hard coral reef model case; although the difference between the Model cases at the near offset is not drastic. As the offset increases, this pattern increases; however, the hard consolidated Model 3 becomes an order of magnitude higher than Model 2 which is an order of magnitude higher than Model 1. This means that for the shallow source, the material properties of the elastic bottom has noticeable impact on the transmitted converted waves. In Model 1, PS* waves are formed and increase in amplitude the further from the source across the horizontal sea-bottom boundary. However, the amplitude of PS* remains lower than the Scholte waves for all model cases. Further, PS* waves exponentially decay with depth which means their amplitudes should decrease further as they travel through the subsurface.

From figure 4.14, the horizontal velocity solution results are shown at $x = 10\ m$, $x = 100\ m$, and $x = 500\ m$ for Model 4, 5, and 6 which represents the far source depth models. The peak amplitude at this offset is $V_x = 8.0 \times 10^{-11}\ m$ for Model 4, $V_x = 9.8 \times 10^{-11}\ m$ for Model 5, and $V_x = 8.8 \times 10^{-11}\ m$ for Model 6. At $x = 100\ m$, the surface Scholte waves dominate the record and the PS* waves are not observed for Model 4. The peak amplitude is $V_x = 4.5 \times 10^{-10}\ m$ for Model 4, and $V_x = 4.6 \times 10^{-10}\ m$ for Model 5 while the peak amplitude increases slightly

to $V_x = 4.8 \times 10^{-10}\ m$ for Model 6. The refracted wave starts to arrive faster for Models 5 and 6 and are distinguishable from the Scholte surface waves. The peak amplitude for Model 4 is $V_x = 2.25 \times 10^{-10}\ m$; whereas, the peak amplitude is $V_x = 1.9 \times 10^{-10}\ m$ and $V_x = 5.1 \times 10^{-10}\ m$ for Models 5 and 6; respectively. Those results indicate that the maximum amplitude is in the far field and is highest for the hard consolidated layer; although the difference between the Model cases at the near offset is not significant. In general, the amplitude increases for all Model cases from near to far offset for the far source depth case; where, the increase for all cases are approximately an order of magnitude. This pattern is opposite to the shallow source cases which confines most of its energy in the near-field instead. Generally, the shallow source cases amplitude values are two orders of magnitudes higher than the far shallow source cases especially in the near-field where most of the energy is transmitted for the shallow source case (Sun and Berteussen, 2009). In Model 4, PS* waves are not formed due to the far distance of the source to the sea-bottom.

# 5. 2D 4C SHEAR WAVE IMAGING IN SHALLOW MARINE ENVIRONMENT

The higher rate of attenuation of S-waves compared to P-waves makes it difficult to obtain a pure shear imaged seismic section. Fortunately, the proximity of the pressure source to the hard sea-bottom in the shallow water environment serves as an effective shear wave generator, which is useful for obtaining a shear wave imaged seismic section. In this chapter, a direct shear wave imaged section from 2D 4C seismic data will be extracted using established model-driven algorithm utilizing well log data.

## 5.1 Methods

The 2D 4C seismic line contains pressure, inline, crossline, and vertical components. In this work, only the pressure and inline components will be processed using Landmark's ProMax software. The processing workflow follows the work of Zhang et al., (2015), Berteussen et al. (2014), and Guo (2017) where model-driven approach utilizing log data is used to extract P and S waves from the pressure and inline components. The log data contains crucial information for this processing method since it not only has P and S wave information at the reservoir level, but also includes velocity information starting $30\ m$ below the sea-bottom. This means the log data is essential in the proposed workflow as shown in Figure 5.1

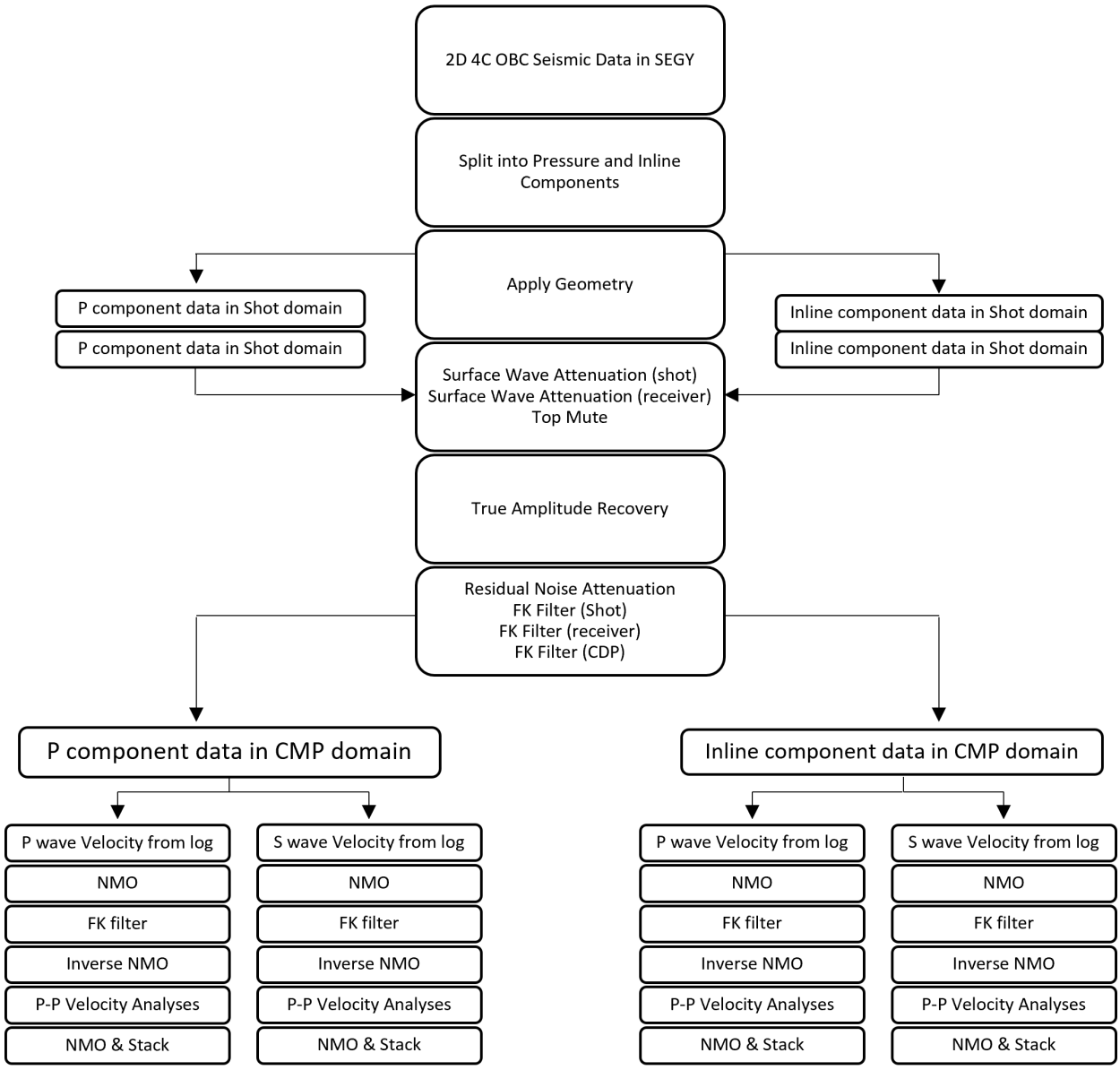


Figure 5.1: Seismic processing workflow focusing on Pressure and Inline components to separate and extract S waves.

When dealing with 4C seismic data, the first step involves separating the data into each component and applying the geometry. Given the highly dispersive surface waves that contaminate the dataset; their removal takes precedence since they mask the desirable reflection signals. To remove the surface waves, a linear move out in the Frequency-Space (FX) domain is utilized. This filter is based on a fixed velocity value and can be fixed for low frequencies which is a common feature for surface waves. This process is done in source side (shot domain) and receiver side (receiver domain). The main reason for multiple domain filtering is that some of the linear features of the surface waves do not exist completely in the shot domain; therefore, receiver domain sorting is used to remove surface waves that appear linear only in this domain. Afterwards, multiple domain Frequency-Wavenumber (FK) filtering is used to remove the residual noises masking the reflection signals. In this context, residual noise represents signals that hide the reflection signals at mid to far offsets after removing the surface waves which include but not limited to direct waves, refracted waves, and back-scattered noise. After removing all the noise, velocity measurements from the log are used as a reference to extract the desirable P and S wave modes from the components. This is done first by the NMO correction which straightens reflectors with similar velocity from the log and then using FK filter to remove all up-dipping and down-dipping events. This leads to two additional results: one using P velocity values for extraction; whereas, the other using S velocities values from log for extraction. The new P and S section are used as a reference to perform another round of Velocity analyses and the resulting velocity picking on the P and S section represents the final P and S stacking velocities that are then used to generate the final P and S stacked sections for each respective component; i.e., pressure and inline components.

## 5.2 Results

### 5.2.1 Log Data Analysis

The well log data used in this study includes Gamma ray, bulk density, effective porosity, water saturation, P wave velocity, and S wave velocity as shown in Figure 5.2. The gamma ray (GR) log is a continuous measurement of the rock's natural radioactivity with higher GR values indicate

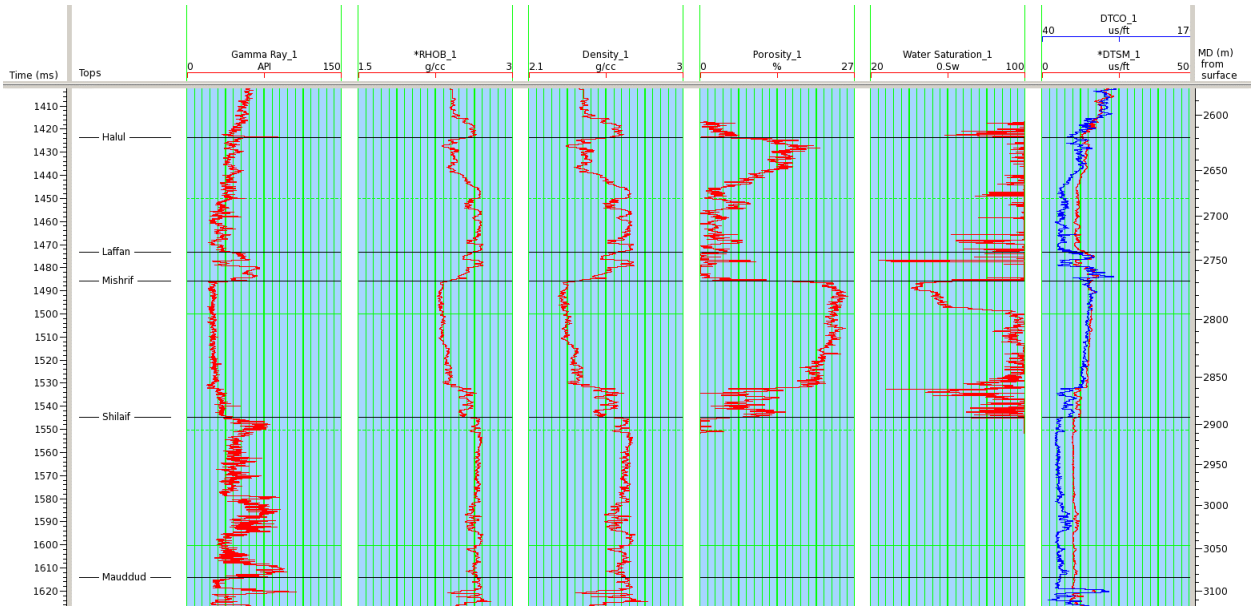


Figure 5.2: Well log data of the nearby well around the reservoir zone. The log data displayed are gamma ray, bulk density, effective porosity, P velocity, and S velocity.

formations such as shale. In the log, GR log is consistently low from depth of 2780 $m$ to 2890 $m$. At the same depth, the porosity values range from 25 to 27 percent. From 2780 $m$ to 2800 $m$, the water saturation is lowest, and peaks right after that depth. Similarly, the porosity is highest at 27 percent and then drops down to 25 percent. This indicates that the oil reservoir is roughly 20 m between 2780 $m$ to 2800 $m$. Velocity values in this range confirms that and the respective two-way travel time (TWT) for the reservoir is approximately at 1.5 $s$.

### 5.2.2 Processing Results

The main objective of the seismic processing is to separate S from P waves and extract a P and S wave structural image of the subsurface. Focusing on the pressure and inline components only, Figures 5.3 and 5.4 show the raw shot gathers for the pressure and inline components, respectively.

As shown from the previous figures, the raw shot gathers are severely contaminated by noise especially surface waves. Following the proposed workflow from figure 5.1, the first round of denoising mainly includes surface wave attenuation in shot domain then receiver domain. The surface wave attenuation is based on waves velocity and frequency values. The typical velocity

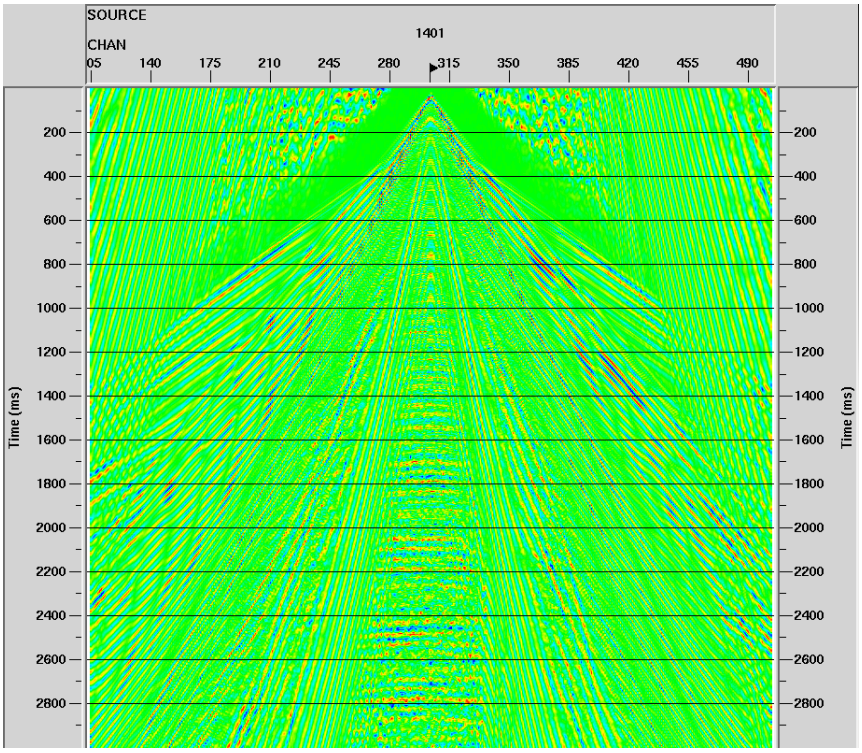


Figure 5.3: Raw shot gather of the pressure component.

value for the Surface wave was measured to between 700 $m/s$ to 1000 $m/s$; thus, multiple surface wave attenuation was applied in both shot and receiver domains. The result after surface wave attenuation for the pressure and inline components are displayed in figure 5.5 and 5.6, respectively.

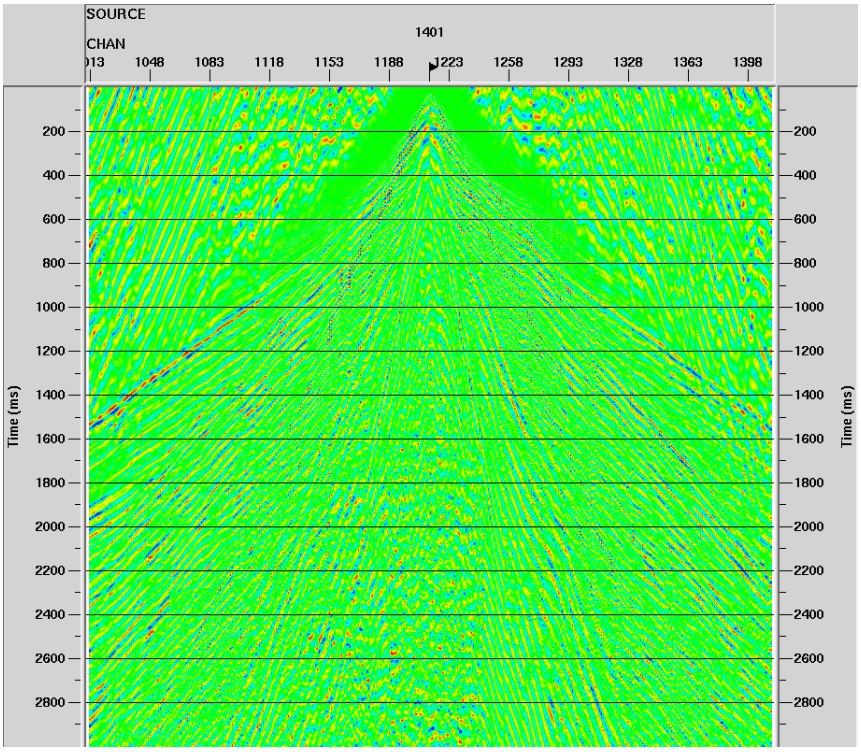


Figure 5.4: Raw shot gather of the inline component.

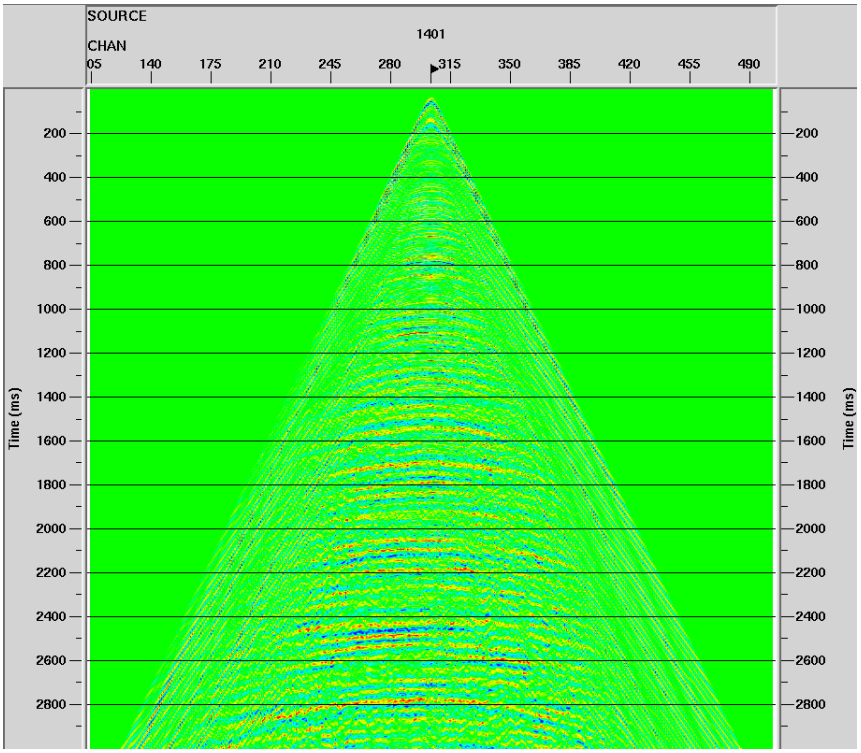


Figure 5.5: Shot gathers after surface wave attenuation for the pressure component.

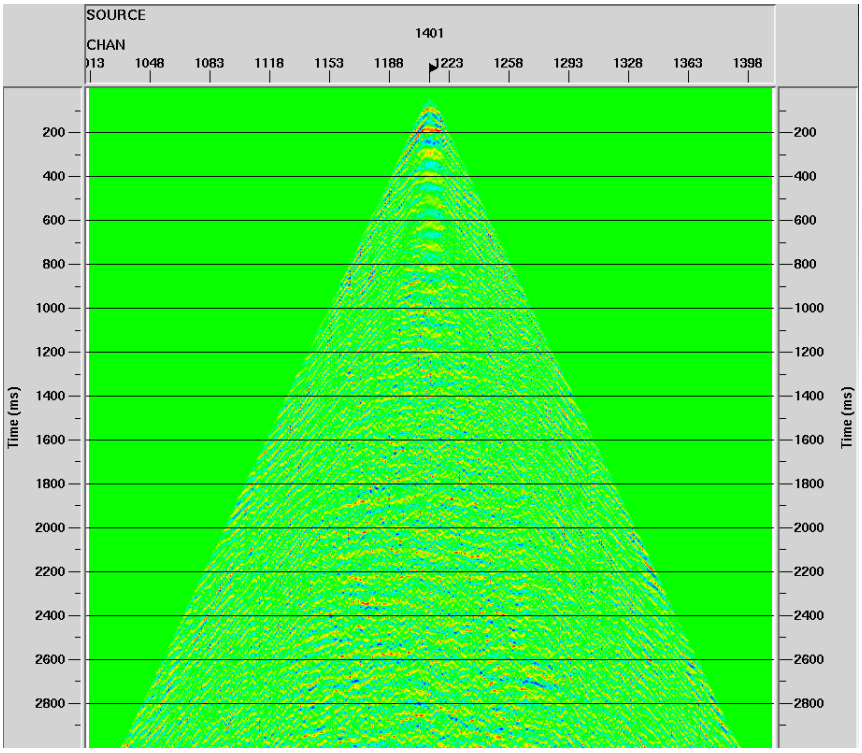


Figure 5.6: Shot gathers after surface wave attenuation for the pressure component.

As shown from the previous figures, removing the surface wave drastically enhances the signal-to-noise ratio by revealing the desirable signal; i.e., reflected hyperbolic waves. It is important to note; however, removing surface waves can remove wanted signals if they overlap due to aliasing. The next step after removing surface waves, is to remove all the remaining residual noises that aren't reflection signals. To do that, a multi-trace FK analysis in utilized as shown in figure 5.7. The FK spectrum transforms the space-time domain of the shot record into frequency-wavenumber domain. This is essentially a 2D Fourier transform that allows the analysis of the waves with frequency and wavenumber. In this domain, linear and hyperbolic events based on their frequencies should separate clearly. Unfortunately, severe aliasing can be observed from the FK spectrum which is a common issue in seismic data acquired in the shallow marine environment of the Arabian Gulf. A polygon in constructed to reject all the unwanted linear events in shot, receiver, and CMP domain. As mentioned earlier, this is done because some linear features cannot be observed

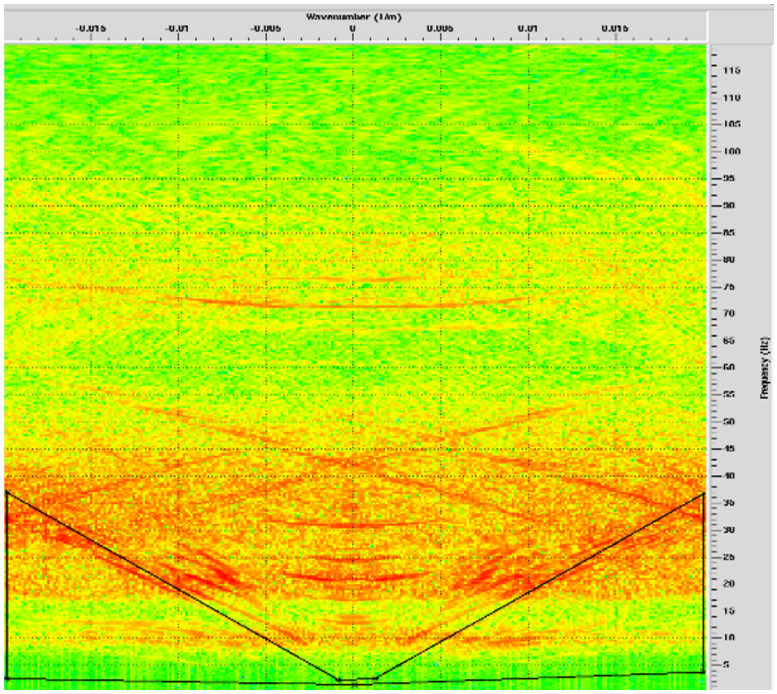

Figure 5.7: FK spectrum of the pressure component using 2D Fourier transform. The arbitrary polygon represents the zone created to reject the unwanted signal.

in a single domain. With SWA and FK filters, most of the coherent noise suppression is completed for the seismic data. At this stage, the P and S wave information can be extracted using NMO correction and FK filter. P wave velocities from the log is used to straighten the filtered seismic gathers followed by an FK filter to extract the P wave and an inverse NMO to get back the P wave extracted gather. Similar process is done for S wave but using the S wave velocities from the log instead. Results from the Fk filtering, P wave extraction, and S wave extraction are displayed for pressure and inline components in figure 5.8 and 5.9, respectively. The heavy filtering sequence successfully removes the contaminating surface waves and residual noise. Also, the extracted P wave gather depicts a hyperbola typical of higher velocities; whereas, the S wave gather depicts a hyperbola of lower velocities. To stack the gathers, velocity analysis is carried out as shown in figure 5.10 Several velocity analyses were carried out on the P-extracted CMP gather and the S-extracted CMP gather. For the P-extracted gather, the velocity values where consistent with less ambiguity due to strong semblance values existing throughout the picking and each sem-

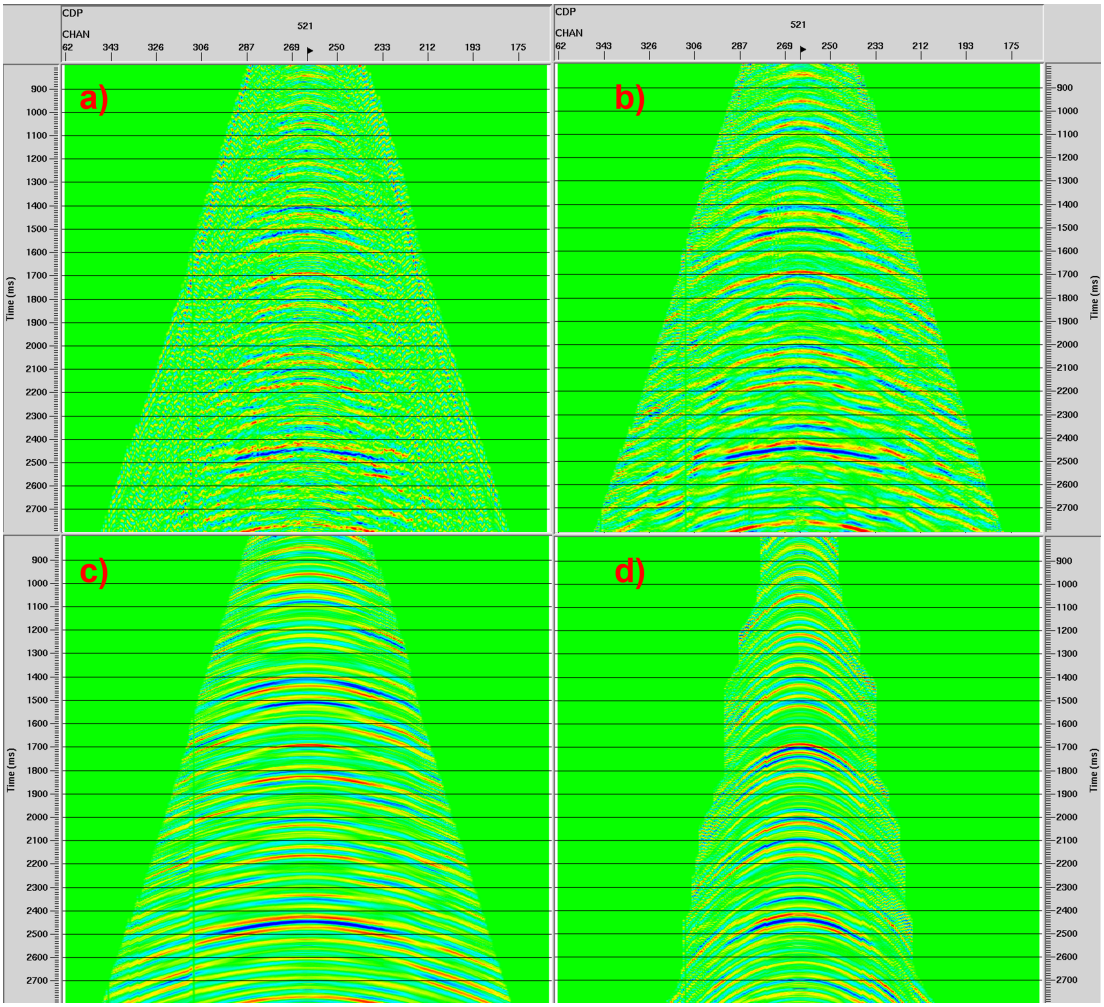


Figure 5.8: Results from applying heavy filtering on the raw pressure record. a) SWA filtered CMP record. b) FK filtered CMP record. P wave extracted CMP record using velocities from the well log. S wave extracted CMP record using velocities from the well log.

blance value corresponds to major reflector signals. However, the S-extracted picking introduces more ambiguity due to semblance values and corresponding reflectors having different response. Therefore, using the log measurements as a guide for S-wave velocity picking resulted in a guided analysis helped picking the reflectors signals. Using the velocity analysis, the final stacked images for the pressure and inline component are shown in figure 5.11 and 5.12, respectively. The stacked seismic sections represent the structural image of the subsurface in the region. In general, the reflectors are approximately flat which is typical of the region. In the pressure component, both the P and S waves stacked section display similar features with decent signal-to-noise ratio (SNR);

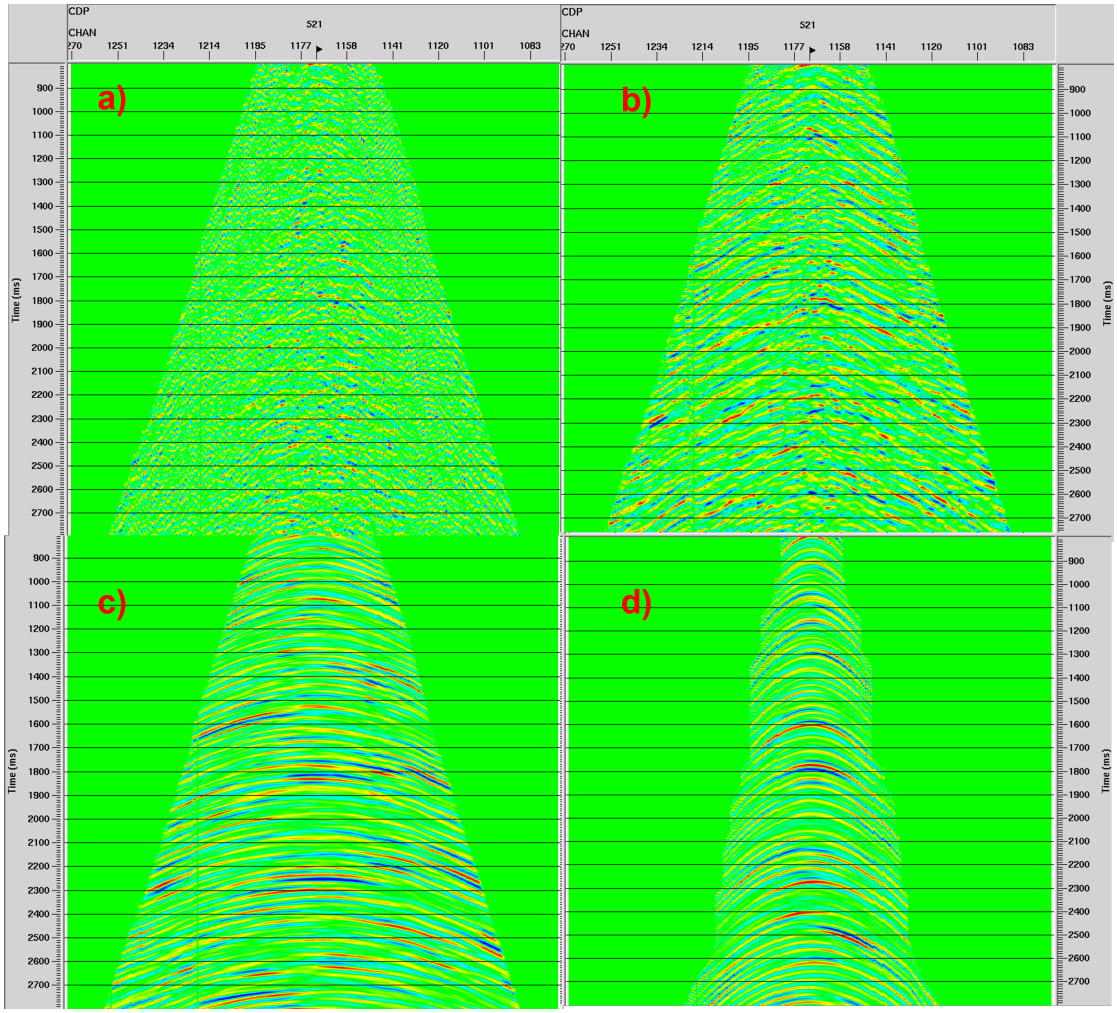


Figure 5.9: Results from applying heavy filtering on the raw inline record. a) SWA filtered CMP record. b) FK filtered CMP record. P wave extracted CMP record using velocities from the well log. S wave extracted CMP record using velocities from the well log.

although, the P wave stacked image of the pressure component has noticeable higher SNR. However, the S stacked image of the pressure component has higher frequency level than the P stacked image. For the inline component, both sections display similar flat reflector pattern; however, the SNR of both P and S wave stacked inline components are noticeably lower than the pressure component. Generally, the inline component stacked section have higher frequency content but the S stacked image has higher SNR than the P stacked image of the inline component. This is expected because the inline component directly measures S waves (direct shear) that reflect from the sub-

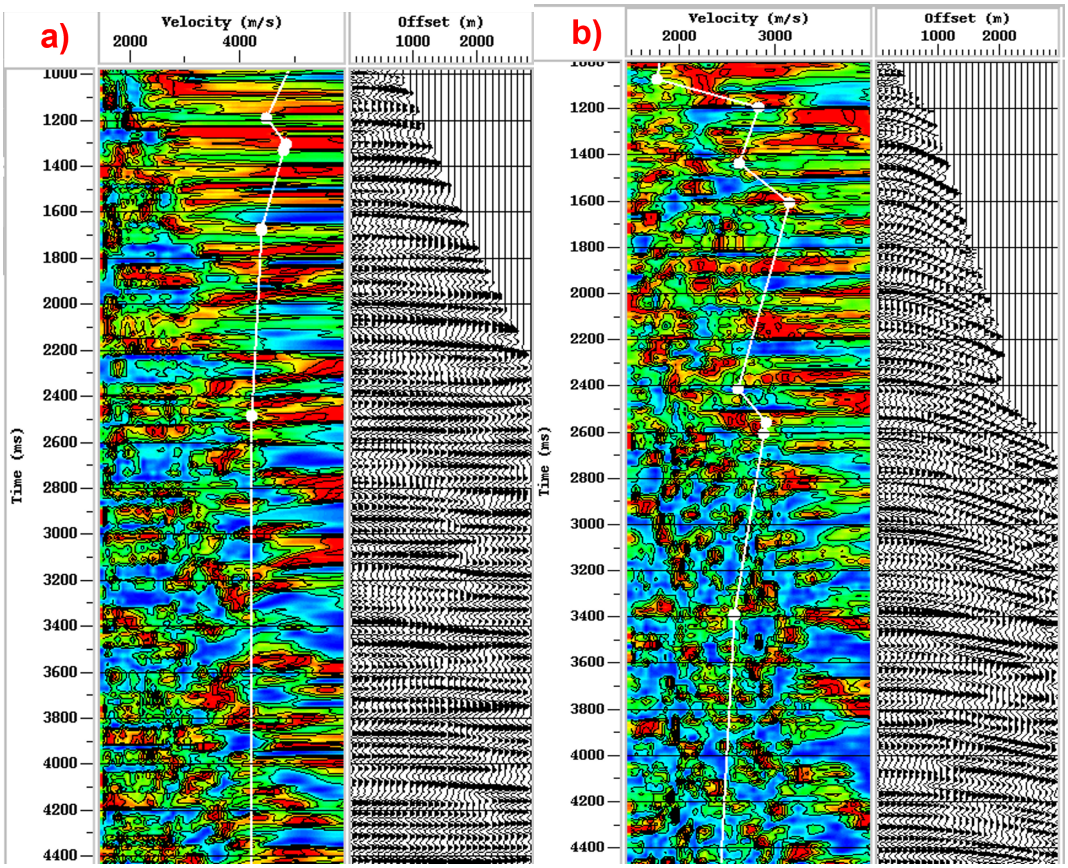


Figure 5.10: Velocity analysis for the pressure component done on the P extracted CMP gather. a) P wave velocity analysis. b) S wave velocity analysis.

surface. The existence of SH* wave from 2D seismic has been successfully confirmed using the same dataset from this study on the crossline component by Guo (2017).

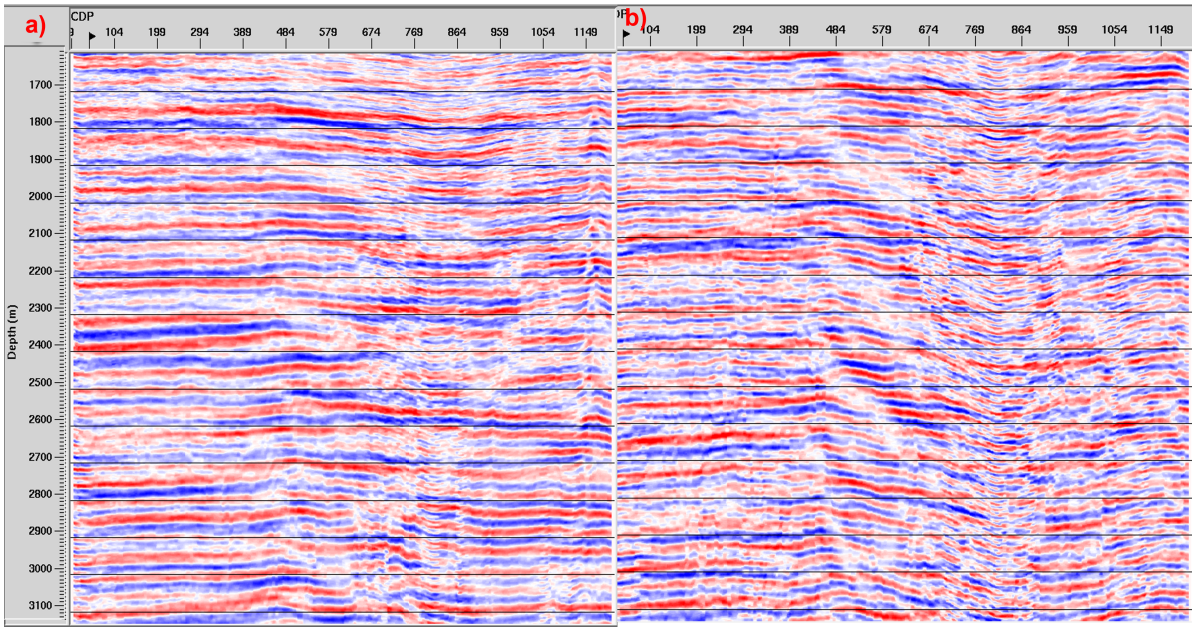


Figure 5.11: Seismic stacking image of the pressure component.a) P wave stacked seismic image. b) S wave stacked seismic image.

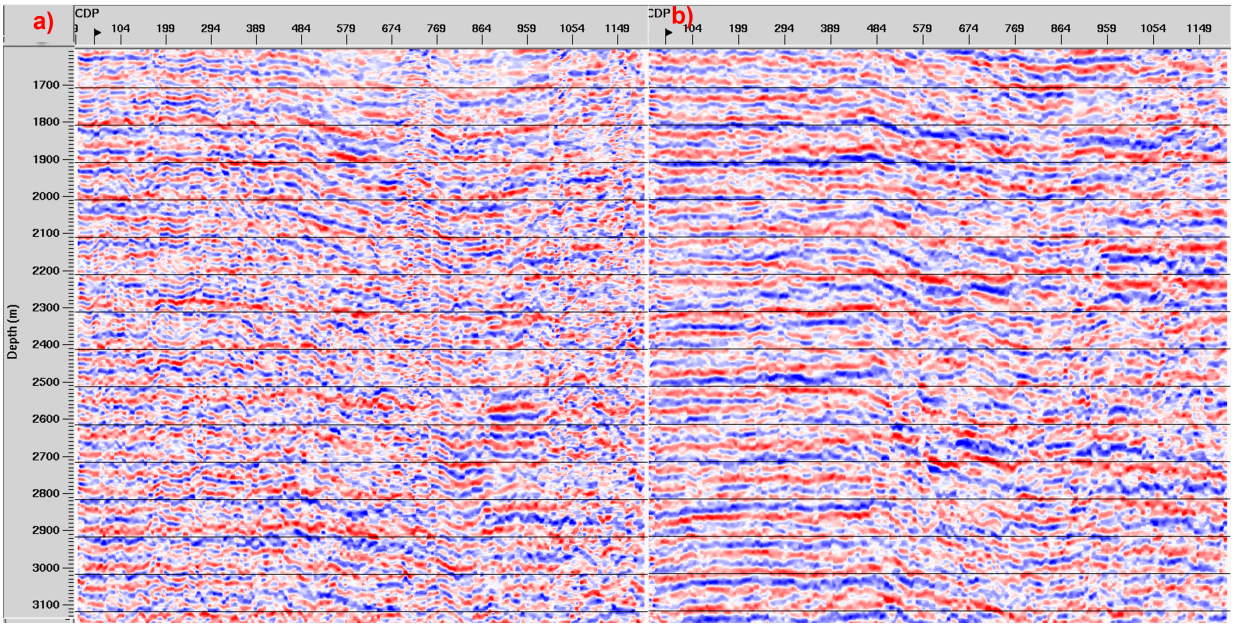


Figure 5.12: Seismic stacking image of the inline component.a) P wave stacked seismic image. b) S wave stacked seismic image.

# 6. CONCLUSIONS

The Arabian Gulf is home to the world's largest oil reserves. This region is characterized by heterogeneous carbonates, very shallow waters (10 m) and hard sea-bottom which presents unique challenges that makes hydrocarbon extraction difficult. This setting is also responsible for strong shear wave generation at the sea-bottom. The strong shear wave generation is attributed to the complicated source mechanism that exists in the region due to the proximity of the source to the seafloor and the varying hard sea-bottom. Extracting shear wave information is essential for reservoir characterization in the offshore fields of the Arabian Gulf and, along with P waves, can help delineate reservoir structures and discriminate bypassed hydrocarbons for production monitoring.

To understand and utilize the strong shear waves generated in the region, the source mechanism was analyzed. Classical wave propagation analysis is not sufficient to address the complex wave interactions between the source and the sea-bottom in shallow waters. To analyze the source, a conceptual body force model was proposed that uses mechanical deformation analysis to define an effective source on the seafloor directly under the acoustic source load. This model explains the generation of SH* and S* waves from an explosive source in the shallow waters with a hard sea-bottom. Considering the acoustic source and seafloor boundary as a single volume element of deformation, the mechanical model is used to explicitly define P, SV, and SH waves body force components from the water depth of the acoustic source and the Poisson ratio difference of the media. Using the effective source, exact analytical solutions were derived to analyze wave propagation, in the near and far-field, for three sea-bottom scenarios representing soft mud, intermediate, and hard coral reef. This was done to observe the effect of acoustic source distance and sea-bottom hardness on wave propagation. With this analysis, shear waves generated from shallow source and hard sea-bottom were found to be more than thousand times stronger than shear waves from far source and soft sea-bottom. The source mechanism was further analyzed using numerical finite-difference wave modeling for seismic wave propagation.

Acquired 2D 4C seismic data in the Arabian Gulf was processed for direct shear wave imaging

utilizing the pressure and inline components only. This processing follows an established model-driven approach that confirmed the existence of direct shear (PSS) waves using the inline component. The existence of SH* waves using the same 2D seismic has been successfully detected in another study. This was done by first addressing the seismic processing challenges that exist in the region including highly dispersive surface waves, water-bottom reverberations, and severe anti-aliasing. Separately extracting P and S wave information involved a NMO-filtering routine that utilized the P and S wave velocities from the well log which provided the necessary step to stack and image the seismic data. Similar geological structural features were observed on both P and S wave stacked section; however, the S stacked section showed higher frequency and resolution on the inline component. The processing workflow greatly enhances the signal-to-noise ratio of the seismic data and also direction extracts shear wave information for reservoir characterization.

# REFERENCES


- Aki, K., and Richards, P.G., 1980, Quantitative Seismology: Theory and Methods. W. H. Freeman & Co., New York.
- Allouche, N., and G. Drijkoningen, 2016, Theoretical analysis of non-geometric PS-waves recorded at the water bottom interface: Geophysical Prospecting, **64**, 543-553.
- Alsharhan, A.S., and Nairn, A.E.M., 1990, A Review of the Cretaceous Formations in the Arabian Peninsula and Gulf: Part III. Upper Cretaceous (Aruma Group) Stratigraphy and Paleogeography. Journal of Petroleum Geology, Vol. 13, p. 247-266.
- Båth, M., 1968, Mathematical Aspects of Seismology: Developments in Solid Earth Geophysics, Elsevier Publishing Comp., New York, 1968.
- Berkhovskikh, L. M., 1980, Waves in Layered Media, Second Edition, Translated by Robert T. Beyer.
- Berteussen, K. and Sun, Y.F. 2010. A critical look at the acquisition parameters for sea bottom seismic in the Arabic Gulf. Proc., 80th SEG Annual International Meeting, Denver, Colorado, 17-22 October, 56-60.
- Berteussen, K., Sun, Y.F., Ali, M., and Zhang, Z. 2014. Hunting S-waves using 4C seismic data in the carbonates, offshore UAE. Proc., 84th SEG Annual International Meeting, Denver, Colorado, 26-31 October, 347-352.
- Cagniard, L., 1939, Reflexion et refraction des seismiques progressives: Gauthier Villars, Paris.
- Chapman, C. H, 1972, Lamb's problem and comments on the paper, 'On Leaking Modes' by Usha Gupta, Pure and Appl Geophys., 94, 233-247.

- Courant, R., Friedrichs, K., and H. Lewy, 1967, On the partial difference equations of mathematical physics: IBM journal of Research and Defvelopment, 11(2), 215-234.

- Crompton, R., Dodge, K., Whitfield, P., Bouska, J., and Johnston, R. 2005. Depth imaging of 3D, 4C OBS surveys in the Caspian sea. Proc. 75th SEG Annual International Meeting, Houston Texas, 5-6 November, 425-428.

- Daley P.F. and F. Hron, 1983, Nongeometric arrivals due to highly concentrated sources adjacent to plane interfaces: Geophysical Journal International, **73**, 1655-1671.

- Daley P.F. and F. Hron, 1988, A non-geometrical SH-arrival. Bulletin of the Seismological Society of America, **36**, 430-445.

- DeVault, B., Davis, T.L., Tsvankin, I., Verm R., Hilterman, F., 2002, Multicomponent AVO analysis, Vacuum field, New Mexico: Geophysics, Vol. 67, p. 701-710.

- DiSiena, J.P., 2017, Historical S-Wave Applications and Aspirations. Proc., 87th SEG Annual International Meeting, Houston, Texas, 24-27 September, 6087-6093.

- Dufour, J., Squires, J., Goodway, W.N., Edmunds, A., and Shook, I., 2002, Integrated geological and geophysical interpretation case study, and Lame rock parameter extractions using AVO analysis on the Blackfoot 3C-3D seismic data, southern Alberta, Canada: Geophysics, Vol. 67, p. 27-37.

- Eringen, A. C., and E. S. Suhubi, 1975, Elastodynamics, vol. ii, linear theory.

- Ewing, W.M., W.S. Jardetzky, P. Frank, and B. Arthur, 1957, Elastic waves in layered media: Physics today, 10(12), 27.

- Farfour, M., and Yoon, W. J., 2016, A review on multicomponent seismology: A potential seismic application for reservoir characterization. Journal of advanced research, 7(3), 515-524.

- Garvin, WW., 1956, Exact transient solution of the buried line source porblem. Proc R Soc Lon Ser A Math Phys Sci, 234, 528-541.

- Granier B., Al-Suwaidi, A.S., Busnardo, R., Aziz, S.K., Schroeder, R., 2003. New Insight on the Stratigraphy of the "Upper Thamama" in Offshore Abu Dhabi (U.A.E.). Camets de Geologie / Notebooks on Geology, Maintenon, Article 2003/05.

- Graves, R.W., 1996, Simulating seismic wave propagation in 3D elastic media using staggered-grid finite differences: Bulletin of the Seismological Society of America, **86**, 1091-1106.

- Guo, H., 2017, Signal Enhancement and Converted Wave Processing of 4C OBC Seismic Data from the Shallow-Water Arabian Gulf: M.S. thesis, Texas A&M University.

- Gutowski, P.R., F. Hron, D.E. Wagner, and S. Treitel, 1984, S*: Bulletin of the Seismological Society of America, **74**, 61-78.

- Hron, F., and Mikhailenko, B. G., 1981. Numerical Modeling of Nongeometrical effects by the Alekseev-Mikhailenko Method. Bulletin of the Seismological Society of America. Vol 71, No 4, pp 1011-1029.

- Ikelle, L., and Amundsen, L. 2005. Introduction to Petroleum Seismology. Tulsa: Society of Exploration Geophysicists.

- Johns, T.D., Vito, C., Clark, R., and Sarmiento, R. 2006. Multicomponent OBC (4C) prestack time imaging: offshore Trinidad, Pamberi, LRL Block. Proc., SEG Annual International Meeting, New Orleans, Louisiana, 1-6 October, 1193-1197.

- Lamb H., 1904, On the propagation of tremors over the surface of an elastic solid: Philosophical Transactions of the Royal Society of London. Series A, Containing Papers of a Mathematical or Physical Character, **203**, 1-42.

- Levander, A.R., 1988, Fourth-order finite-difference P-SV seismograms: Geophysics, **53**, 1425-1436.

- Madriaga, R., 1976, Dynamics of an expanding circular fault: Bulletin of the Seismilogical Society of America, **66**, 163-182.
- Meredith J.A., C.H. Cheng, and M.N. Toksoz, 1991, Modelling of Downhole Seismic Sources I: Literature Review, Review of Fundamentals, Impulsive point Source in a Borehole: Massachusetts Institute of Technology. Earth Resources Laboratory.
- Pekeris, CL., 1956, Solution of an integral equation occurring in impulsive wave propagation problems: Proc Natl Acad Sci, 42, 439-443.
- Pilant, W. L., 1979, Elastic Waves in the Earth: Elsevier Scientific Publishing Company.
- Rajput, S. 2010. Converted wave velocity model using 4C ocean bottom seismometer data. Proc., ASEG 21st Geophysical conference.
- Sanchez-Sesma, J. Francisco , U. Iturraran-Viveros, and E. Kausel, 2012, Garvin's Generalized Problem Revisited: Soil Dynamics and Earthquake Engineering, **47**, 4-15.
- Shan, Z., and D. Ling, 2016, An analytical solution for the transient response of a semi-infinite elastic medium with a buried arbitrary cylindrical line source: International Journal of Solids and Structures, **100 − 101**, 399-410.
- Sharland, P.R., Archer, R., Casey, D.M., Davies, R.B., Hall, S.H., Heward, A.P., Horbury, A.D., and Simmons, M.D., 2001, Arabian Plate Sequence Stratigraphy. GeoArabia, Special Publication 2, Bahrain. pp. 371.
- Singh, P., Davis, T.L., and DeVault, B., 2015, Poststack, prestack, and joint inversion of P- and S-wave data for Morrow A sandstone characterization. Interpretation, Vol. 3, SZ59-SZ92.
- Stein, S. and M. Wysession, 2009, An introduction to Seismology, Earthquakes, and Earth Structure: John Wiley & Sons.

- Stewart, R.R., Gaiser, J.E., Brown, R.J., and Lawton, D.C., 2003, Converted-wave seismic exploration: Applications. Geophysics, Vol. 68, p. 40-57.

- Stokes, G.G., 1849, On the variation of gravity on the surface of the Earth: Trans. Camb. Phil. Soc., 8, 672-695.

- Sun, Y.F. and Berteussen, K., 2009a, New opportunities of 4C ocean bottom seismic in shallow-water environment of the Arabian Gulf: A case study. Proc.,79th SEG Annual International Meeting, Houston, Texas, 25-30 October, 46-50.

- Sun, Y.F., and Berteussen, K., 2009b, Challenge and opportunity of 4C ocean bottom seismics in shallow water environment. Proc.,71st EAGE Conference, Amsterdam, Netherlands, 8-11 June, 1-5.

- Virieux, J., 1986, P-SV wave propagation in heterogeneous media: Velocity-stress finite-difference method. Geophysics, Vol. 51(4), p. 889-901.

- Winterstein, D.F., 1987, Invited introductory paper: Shear waves in exploration: A perspective. SEG Technical Program Expanded Abstracts 1987: pp. 638–641 Yilmaz, O. 2001. Seismic Data Processing. Tulsa: Society of Exploration Geophysicists.

- Zhao Zhang, Yuefeng Sun, Karl Berteussen, and Mohammed Ali (2015) 4C OBC shear wave processing in shallow water environment of the Arabian Gulf. SEG Technical Program Expanded Abstracts 2015: pp. 2113-2117.